DESIGN OF A NOVEL LOW-LOSS FREQUENCY SCANNING ANTENNA

A THESIS SUBMITTED TO
THE GRADUATE SCHOOL OF NATURAL AND APPLIED SCIENCES
OF
MIDDLE EAST TECHNICAL UNIVERSITY

BY

SENA ALKIŞ

IN PARTIAL FULFILLMENT OF THE REQUIREMENTS
FOR
THE DEGREE OF MASTER OF SCIENCE
IN
ELECTRICAL AND ELECTRONICS ENGINEERING

DECEMBER 2019

Approval of the thesis:

DESIGN OF A NOVEL LOW-LOSS FREQUENCY SCANNING ANTENNA

submitted by **SENA ALKIŞ** in partial fulfillment of the requirements for the degree of **Master of Science in Electrical and Electronics Engineering Department, Middle East Technical University** by,

Prof. Dr. Halil Kalıpçılar
Dean, Graduate School of **Natural and Applied Sciences** _____

Prof. Dr. İlkay Ulusoy
Head of Department, **Electrical and Electronics Eng.** _____

Assoc. Prof. Dr. Özgür Ergül
Supervisor, **Electrical and Electronics Eng., METU** _____

Dr. Erdinç Erçil
Co-Supervisor, **ASELSAN** _____

Examining Committee Members:

Prof. Dr. Özlem Aydın Çivi
Electrical and Electronics Eng, METU _____

Assoc. Prof. Dr. Özgür Ergül
Electrical and Electronics Eng., METU _____

Assoc. Prof. Dr. Lale Alatan
Electrical and Electronics Eng, METU _____

Prof. Dr. Asım Egemen Yılmaz
Electrical and Electronics Eng, Ankara University _____

Prof. Dr. Vakur Ertürk
Electrical and Electronics Eng, Bilkent University _____

Date: 18.12.2019

I hereby declare that all information in this document has been obtained and presented in accordance with academic rules and ethical conduct. I also declare that, as required by these rules and conduct, I have fully cited and referenced all material and results that are not original to this work.

Name, Surname: Sena Alkış

Signature:

ABSTRACT

DESIGN OF A NOVEL LOW-LOSS FREQUENCY SCANNING ANTENNA

Alkış, Sena
Master of Science, Electrical and Electronics Engineering
Supervisor: Assoc. Prof. Dr. Özgür Ergül
Co-Supervisor: Dr. Erdinç Erçil

December 2019, 156 pages

In antenna engineering, frequency scanning arrays are well-known with their ability to provide low-cost electronic scanning capability. However, in many studies on these arrays, the loss of the structure is overlooked. In this study, a novel low-loss frequency scanning antenna structure is proposed. The design is a composition of a feeding waveguide utilized for frequency scanning in one plane and an array of eight elements in the other plane, which is repeated along the frequency scanning axis. The loss of the antenna is relatively low thanks to using a metallic waveguide as a beamformer and a stripline antenna as the array element. Each stripline eight-element array is fed via a novel coupling structure, which is a stripline 90-degree hybrid coupler whose input arms are inserted into the waveguide. The coupling amplitude of the structure is controlled by the insertion depth of the 90-degree hybrid couplers, which are exploited for controlling the amplitude distribution along the frequency scanning axis. The study focuses on all aspects of the design procedure and the followed methodology, as well as difficulties came across throughout the design and the methods to cope with them.

Keywords: Travelling Wave Antenna, Frequency Scanning Array, Scan Blindness, Wide-Angle Scanning, Tapered Slot Antenna

ÖZ

DÜŞÜK KAYIPLI YENİ BİR FREKANS TARAMALI ANTEN TASARIMI

Alkış, Sena
Yüksek Lisans, Elektrik ve Elektronik Mühendisliği
Tez Danışmanı: Doç. Dr. Özgür Ergül
Ortak Tez Danışmanı: Dr. Erdinç Erçil

Aralık 2019, 156 sayfa

Anten mühendisliğinde, frekans taramalı diziler, düşük maliyetli elektronik tarama yeteneği sağlamalarıyla bilinmektedir. Fakat bu dizilerle ilgili birçok çalışmada anten kaybına yeterince önem verilmediği görülmektedir. Bu çalışmada, düşük kayıplı yeni bir frekans taramalı anten tasarımı önerilmektedir. Tasarım, bir düzlemde frekans taraması için dalga kılavuzu besleme yapısı, diğer düzlemde ise frekans taraması ekseni boyunca tekrarlanan sekiz elemanlı bir anten dizisinden oluşmaktadır. Metalik dalga kılavuzu yapısının hüzme oluşturma devresi ve şerit hat antenlerin dizi elemanları olarak kullanılması sayesinde, anten kaybı görece az olmaktadır. Sekiz elemanlı her bir şerit dizi, yeni bir bağlaşım yapısı ile beslenmektedir. Bu yapı, kolları dalga kılavuzunun içine daldırılan bir 90 derece şerit hat hibrit yapısıdır ve bağlaşım miktarı yapının dalga kılavuzuna daldırılma derinliği ile belirlenmektedir. Böylelikle frekans tarama eksenindeki genlik dağılımı kontrol edilebilmektedir. Çalışmada, tüm yönleriyle tasarım prosedürü ve takip edilen metodoloji, ve bunlara ek olarak tasarım esnasında karşılaşılan sorunlar ve bu sorunların çözülmesi için sunulan metotlar irdelenmiştir.

Anahtar Kelimeler: İlerleyen Dalga Anten, Frekans Taramalı Dizi, Tarama Körlüğü, Geniş Açılı Tarama, Açıklığı Daralan Yarık Antenler

To Türkan Töre

ACKNOWLEDGEMENTS

First, I want would express my sincere and deepest gratitude to my supervisor Assoc. Prof. Dr. Özgür Ergül for his invaluable guidance and motivation throughout all my Master's and also undergraduate studies. I would like to thank Prof. Dr. Özlem Aydın Çivi, Assoc. Prof. Dr. Lale Alatan, Prof. Dr. Vakur Ertürk and Prof. Dr. Asım Egemen Yılmaz for being on my thesis committee and their suggestions.

I would like to express my deepest appreciation to Erdinç Erçil for his guidance, patience and invaluable experience. I would like to thank Egemen Yıldırım, Ömer Bayraktar, Akın Dalkılıç, Dilek Yalçınkaya, Mert Taşçı and all my other collegues for their suggestions and support on this work. I would like to thank Mustafa Demircan for the mechanical designs and all my collegues who take part in the manufacturing processes. I am grateful to ASELSAN, for providing financial and technical opportunities to complete this study.

I would like to thank Barışcan Karaosmanoğlu, Can Önol, Şeyda Kaya, Sinan Emre Senem and all other group members of CEMMETU. I would like to thank TUBITAK for the scholarship program.

I would particularly like to thank Hande İbili, Aşkın Altınoklu for their help during my Master's studies and their invaluable friendship. I would like to thank Deniz Çavdar, Berna Barutcu, Özlem Gümüşkanat, Alperen Çalıkoğlu, Eray Ercan, Muammer Kozan and Gökhan Gültepe for their constant support. I would like to thank Yusuf Deniz for his endless support, patience and compassionateness.

I would like to express my deepest gratitude to my mother, father and grandmothers, for their endless love, care and patience. Any of my successes would not have been possible without their never-ending support and blessings. I also want to thank my all other family members who always show their support and wish me the best.

TABLE OF CONTENTS

LIST OF TABLES

TABLES

LIST OF FIGURES

FIGURES

CHAPTER 1

INTRODUCTION

Many modern military and civil systems require antenna beams that are quickly pointed to the desired directions in space. Mechanical scanning antennas are almost always short of satisfying the speed requirements of such systems. Besides, it is quite possible that the desired beam pointing angles be totally random in time. This requirement makes the mechanical systems even less capable of providing the requirements of the modern architectures.

Phased array antennas are the most popular and versatile devices that are able to fulfill the functions required by the modern systems. However, as the number of antenna elements increases, the cost and complexity of the phased arrays become a disadvantage and make them less attractive. Especially when the scanning is to be done in one axis (azimuth or elevation) and the frequency of operation is not dictated by other operational requirements, frequency scanning arrays are more convenient options that offer electronic scanning capability at lower costs than phased arrays.

In this study, a novel low-loss frequency scanning antenna structure is proposed. In the following, the motivation of the study and the design specifications are introduced. The proposed design is briefly mentioned and the outline of the thesis is presented.

1.1. Motivation and Design Requirements

In a radar system, antenna is one of the critical components that is both responsible for transmitting and receiving functions. Specifically, radar operational capabilities and cost are defined by the antenna to a great extent [1]. In a transmission mode the radar antenna converts the radio frequency signal that is generated by the radar to radiated energy in the form of a beam towards targets. In a receiving mode,

the received echo scattered from a target is converted to a radio-frequency signal by the antenna.

In the proposed design, being low-loss is one of the main considerations within the scope of the design limits. The design aims an array with frequency scanning in one axis, while there are no scanning requirements in the other axis. In the frequency scanning axis (azimuth), several requirements are considered. These are beam scanning over an angular range of 80°, high directivity, and low side-lobe levels. In the other axis (elevation), a pencil beam is required such that it has approximately 9° half-power beamwidth. The design specifications are summarized in Table 1.1.

Table 1.1. Design specifications.

Specification	**Value**
Frequency bandwidth (for the specified scan range and side-lobe level at azimuth axis)	12 %
Scan range	>80°
Half-power beamwidth at broadside (azimuth axis)	<2.3°
Half-power beamwidth at broadside (elevation axis)	~9°
Side-lobe level (azimuth axis)	<−18 dB

Beam scanning is the ability to steer the beam of the antenna to desired directions. Rapid change of the steering angle is necessary in many radar applications. Beam scanning can be realized by mechanically or electronically. The reasons that makes the mechanical scanning not favorable are mentioned in Section 2.3.

Directivity of an antenna is determined by the general shape of the radiation pattern and it is especially related to the half-power beamwidth. The directivity is usually increased by narrowing the beam. A high directivity ensures that most of the

energy is directed towards to target. To resolve the targets that are close to each other and to make accurate angular measurements, high directivity values are necessary.

Side-lobes are the maxima in the antenna pattern other than the main beam. Large side lobes are not desirable for several reasons. First, they can result in false detections since signals can be received unintentionally from side lobe directions. Second, they increase clutter signals in radar applications. In addition to those, side lobes cause vulnerability against jamming. Thus, low side-lobe levels are desired in general, which can be obtained by properly tapering the antenna excitation.

1.2. Proposed Design

The proposed design, shown in Figure 1.1 and Figure 1.2 consists of a feeding waveguide section as a beamformer to provide frequency scanning in one plane and an array of eight stripline antenna elements in the other plane repeated along the frequency scanning axis. The loss of the antenna is relatively low thanks to the use of an empty metallic waveguide as a beamformer and stripline antennas as the array elements.

In the design, Vivaldi tapered slot antennas are aligned along a rectangular grid to form the array. Important properties of such tapered slot antennas are given in Section 2.4 in detail. The reasons to use a Vivaldi design are its endfire radiation characteristics, convenience for a broadband operation, planar and simple geometry, suitability for a stripline configuration, and low weight. The excitation of the stripline Vivaldi array in elevation axis is realized by a stripline power divider. The power divider is designed by a proper arrangement of 2-way stripline Wilkinson power dividers.

The stripline Vivaldi array is fed via a novel coupling structure. The structure is a stripline 90-degree hybrid coupler whose input arms are inserted into the waveguide from the broadwall. The coupling amplitude of the structure is controlled by the insertion depths of the arms of the coupler to realize the desired amplitude distribution along the frequency scanning axis.

A major component of a frequency scanning antenna is the beamforming circuit. A waveguide beamformer is preferred over other options, namely microstrip or stripline-type tranmission structure, to end up with a low-loss antenna. A waveguide beamformer can be considered as a travelling-wave array with stripline coupling ports instead of radiating elements. In order to scan a large angular sector, phase shifts between array elements need to be relatively large. Feeding array elements by an air filled linear waveguide is not convenient since the array becomes very long and grating lobes arise due to large element spacings. Another method to create large phase shifts is to fill the used waveguide with high-permittivity materials, which is also not favorable since it results in high propagation losses and large mass. To ensure compactness and not to introduce propagation losses, a meandered waveguide array is utilized.

One of the main problems in the design of travelling-wave arrays is the scan blindness due to coherent build-up of reflections at the input port when the frequency is tuned to generate a broadside beam. The proposed 90-degree hybrid coupler yields a low reflection coefficient and alleviates the gain loss associated with the scan-blindness phenomenon since the arms of the coupler inside the waveguide are separated by a quarter wavelength. Moreover, quarter-wavelength separation of the arms results in a directional characteristics of the overall coupling structure. This directional characteristics is useful for suppressing the coupling of reflected signals from subsequent antenna elements.

1.3. Thesis Outline

The thesis consist of four chapters. Chapter 2 is divided into three subsections to introduce the theoretical background information on antenna arrays, waveguide-fed slot arrays, and tapered slot antennas.

In Chapter 3, the design procedure of the proposed study is outlined and simulation results are given. Detailed design procedures of the waveguide beamformer with the stripline 90-degree hybrid coupling structure, as well as the designs of Vivaldi

antenna elements and the eight-element array are presented with simulation results. Moreover, the overall design, i.e., the Vivaldi array integrated with the waveguide beamformer, is reported with simulation results.

Finally, the overall accomplishments of the study and future works are discussed in Chapter 4.

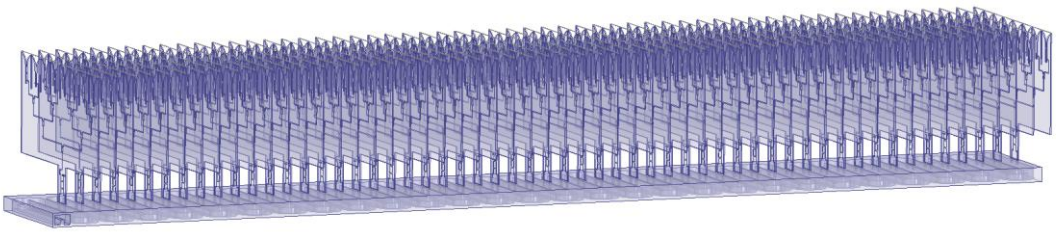

Figure 1.1. The final design.

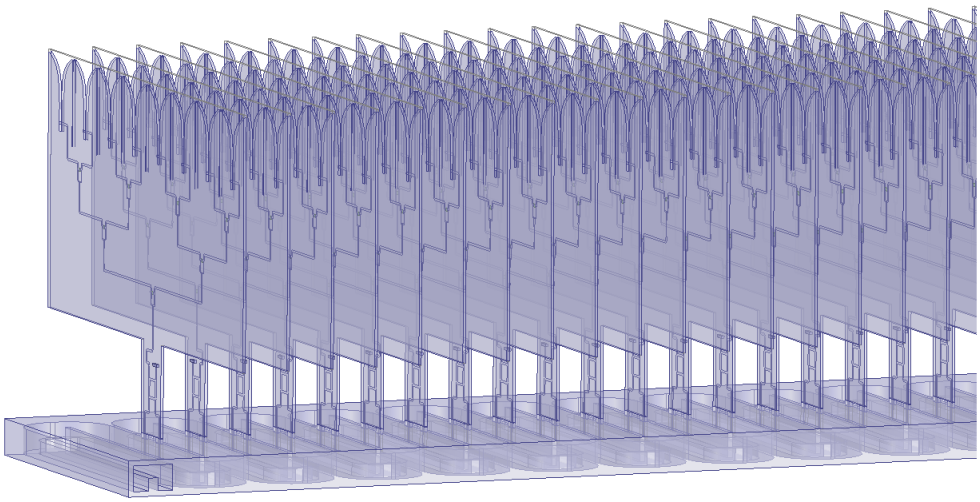

Figure 1.2. The final design (zoomed view).

CHAPTER 2

THEORETICAL BACKGROUND

2.1. Antenna Array Theory

An antenna array is a configuration of multiple antenna elements that work together as a single antenna. Field of an antenna array is a vector addition of the fields radiated by each individual antenna element in the array environment. In this chapter, basic antenna array theory will be reviewed and scanning arrays will be mentioned. Additional information and derivations can be found in textbooks, such as [2].

In general, increasing the electrical size of an antenna increases its directivity. In the context of antenna arrays, by increasing the number of elements or increasing the aperture size of an antenna array, higher directivity values may be obtained. In radar applications, if targets that are close to each other are to be resolved or if there is a need for accurate angular measurements, narrow beamwidths become crucial [3]. Moreover, antenna arrays can provide electronic scanning, which makes them very common in radar applications.

The pattern of an antenna array is controlled by the placement of array elements, as well as their relative patterns (in array environment) and excitations (both amplitude and phase).

2.1.1. Array Pattern Multiplication

As stated, pattern of an antenna array can be calculated by vector addition of the fields radiated by the individual elements of that array. For an array of identical elements, for which mutual coupling between elements can be neglected, the total pattern of the array can be approximated as the multiplication of the pattern of a single

element at a reference point with the array factor. This principle is called "the principle of pattern multiplication", which can be written as

$$F_{total}(\theta, \phi) = f_{single\ element}\ (\theta, \phi)\ \times\ AF(\theta, \phi). \qquad (2.1)$$

The array factor can be thought as a transfer function of a linear system and it is based on the assumption that the radiation pattern of an array is generated by isotropic radiators instead of actual array elements. Thus array factor is a function of the number of array elements, their placements and excitations, but not of their directional characteristics.

Although geometrical configurations of antenna arrays can be diverse, linear and planar arrays are very common in radar applications [3]. If array elements are aligned in a straight line, the array is called linear. If elements are arranged in a rectangular grid, they form a planar array, which can also be considered as a linear array of linear arrays. Linear array and planar array configurations are shown in Figure 2.1 and Figure 2.2, respectively.

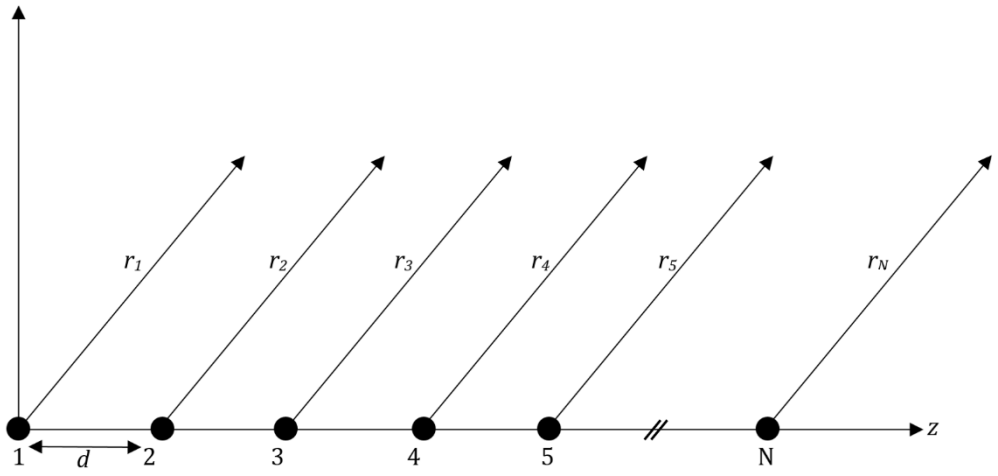

Figure 2.1. Linear array.

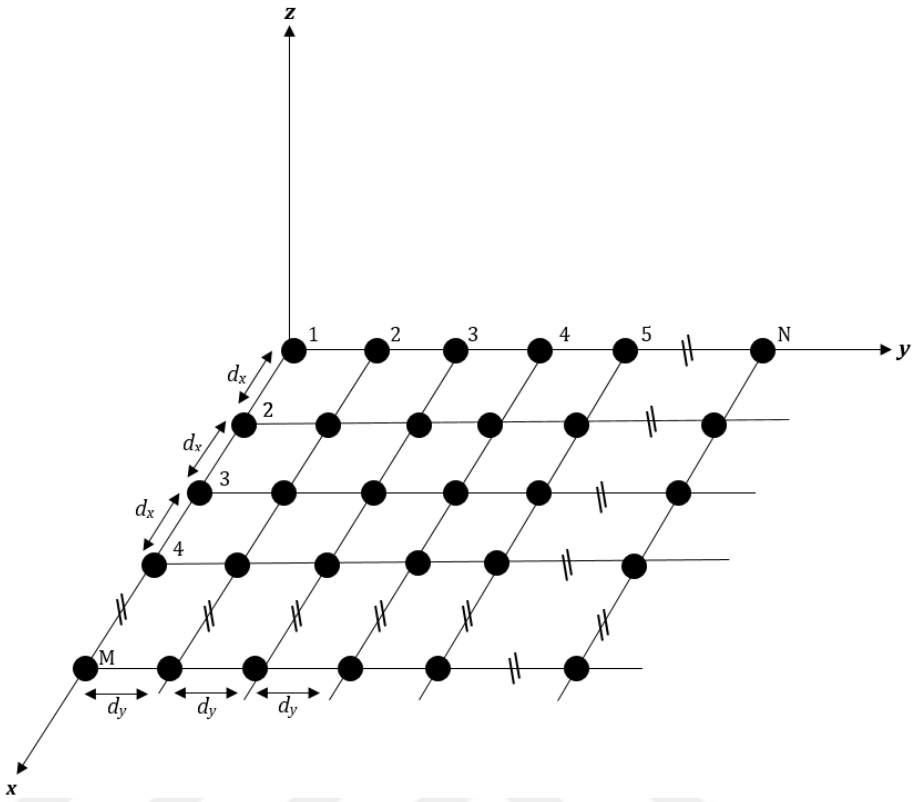

Figure 2.2. Planar array.

In far-field region, the observation points are far away from the array in comparison to its size. Thus, referring to Figure 2.1, distances to observation points (r_n) can be assumed to be constant for amplitude variations ($r_n = r_1 = r_2 = \cdots$). On the other hand, the angular coordinates of the observation points can be assumed to be same for each element and r_n can be approximated as $r_n = r_0 + ndcos\theta$ for phase variations of a uniformly spaced linear array positioned along the z axis, where θ is the usual spherical coordinate angle. Then, the array factor of an N-element linear array with uniform spacing can be written as

$$AF = \sum_{n=1}^{N} I_n e^{jk(n-1)d\cos\theta}, \qquad (2.2)$$

where $I_n = a_n e^{j\beta_n}$ is the complex excitation for the n^{th} element and k is the wavenumber that equals to $2\pi/\lambda$.

In many practical scenarios, array factor can be sufficient to predict the total radiation pattern. The properties that are mostly considered in the design of an array antenna are main beam direction, half-power beamwidth, side-lobe levels, and directivity. In the next section, these properties will be discussed on the simplest type of arrays, i.e., N-element linear array with uniform amplitude and spacing. These concepts may be applied to more complex linear arrays in a similar manner.

2.1.2. Properties of Uniform Arrays

A uniform array is the one with identical elements that are uniformly spaced and excited with identical magnitudes ($a_n = a$) but a progressive phase (β), by which the current in an element leads the current of the previous element, i.e., $\beta_n = (n-1)\beta$. From (2.2), the array factor for a uniform array can be written as

$$AF = \sum_{n=1}^{N} e^{j(n-1)\psi}, \tag{2.3}$$

where

$$\psi = kd\cos\theta + \beta. \tag{2.4}$$

By using (2.3), the normalized array factor for a linear uniform array can be approximated as

$$(AF)_n = \frac{1}{N}\left[\frac{\sin\left(\frac{N}{2}\psi\right)}{\sin\left(\frac{1}{2}\psi\right)}\right]. \tag{2.5}$$

2.1.2.1. Main Beam Direction

Considering the normalized array factor in (2.5), maxima of the antenna array pattern occur when

$$\psi = \pm 2m\pi, \qquad m = 0,1,2, \ldots \tag{2.6}$$

Substituting (2.6) into (2.4), the angular position of these maxima can be found as

$$\theta_m = \cos^{-1}\left[\frac{\lambda}{2\pi d}(-\beta \pm 2m\pi)\right]. \tag{2.7}$$

Generally, the main lobe is considered as the $m = 0$ maximum, which is located at

$$\theta_m = \cos^{-1}\left[\frac{\lambda\beta}{2\pi d}\right]. \tag{2.8}$$

Other maxima that occur in the visible angular range $0 \leq \theta \leq \pi$ for different values of m are called grating lobes, which are generally undesired. To avoid grating lobes, the element spacing (d) is arranged such that θ_m is defined only for $m = 0$ in (2.7). For example, element spacing $d \leq \lambda/2$ ensures that there is not any grating lobe. However, one may design an array with larger element spacing while avoiding grating lobes by obeying a relation

$$d \leq \frac{\lambda}{1 + |\cos\theta_0|}, \tag{2.9}$$

which can be obtained from (2.7).

2.1.2.2. Half-Power Beamwidth

Half-power beamwidth, shown in Figure 2.3, which is also known as 3-dB beamwidth, is defined as the angle between the two directions, in which the radiation

intensity is the half of the maximum value, in a plane containing the direction of the maximum of the beam [4]. Generally, half-power beamwidth is considered for the main beam and it is sometimes abbreviated as "beamwidth". Half-power points, $\theta_{h_1}$and θ_{h_2}, which are the directions that radiation intensity is half of the maximum value, can be calculated by setting the magnitude squared normalized array factor in (2.5) to ½. Then, the half-power beamwidth is equal to

$$HPBW = |\theta_0 - \theta_{h_1}| + |\theta_0 - \theta_{h_2}|. \qquad (2.10)$$

2.1.2.3. Side-Lobe Levels

Considering the normalized array factor in (2.5), secondary maxima may be observed in an array pattern. These maxima occur approximately when

$$N\psi = \pm(2s+1)\pi, \qquad s = 1,2,\ldots \qquad (2.11)$$

Substituting (2.6) into (2.11), the angular positions of these maxima, which are called side-lobe positions, can be found as

$$\theta_s = \cos^{-1}\left[\frac{\lambda}{2\pi d}\left(-\beta \pm \frac{(2s+1)\pi}{N}\right)\right], \qquad s = 1,2,.., \qquad (2.12)$$

where s corresponds to the sequence of the side lobe. This means that $\theta_{s=1}$ is the location of the first side lobe, $\theta_{s=2}$ is the location of the second side lobe, etc. Side-lobe level is generally defined as the dB value of the largest secondary maxima. For a uniform array, the first side lobe is the largest secondary maximum and the side-lobe level is approximately -13 dB.

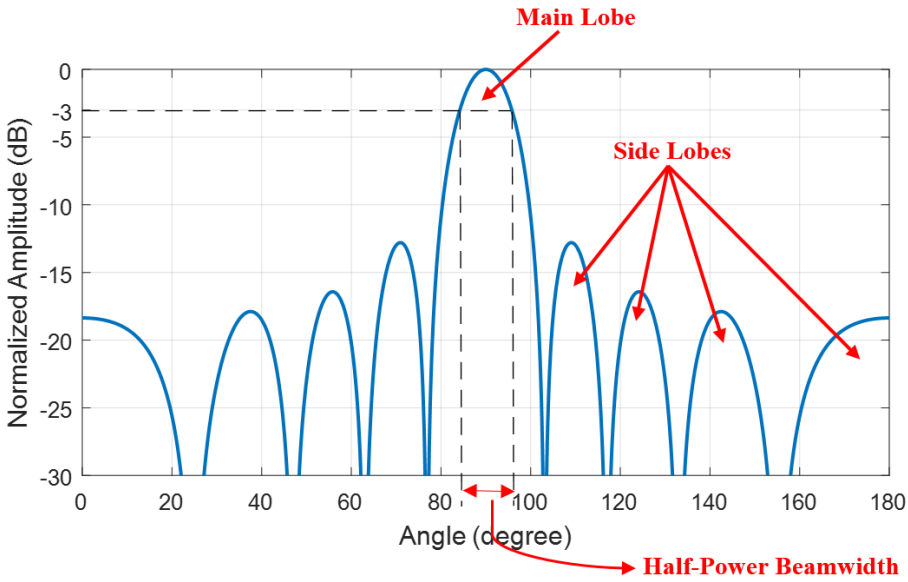

Figure 2.3. Radiation pattern lobes and half-power beamwidth.

2.1.2.4. Directivity

Directivity is defined as the ratio of the radiation intensity in the direction of maximum radiation to the radiation intensity averaged over all directions, as given in [4]. In a mathematical form, it is written as

$$D = \frac{4\pi U}{P_{rad}}, \tag{2.13}$$

where U is radiation insensity and P_{rad} is total radiated power. As stated previously, in most radar applications, directive antennas are necessary, and the directivity of an antenna array can be increased by increasing the number of elements or increasing its aperture size. There is a close relationship between the half-power beamwidth and the directivity of an antenna, i.e., narrower beamwidth usually represents high directivity and vice versa.

2.1.3. Planar Arrays

To form a planar array, individual antenna elements can be positioned in a rectangular grid. Planar arrays may be considered as linear arrays of linear arrays, and their radiation patterns can be written as the products of the radiation patterns in two planes if their arrangement and excitations are separable in those two planes. Thus, with a planar array configuration, the main beam can be shaped in two planes and may be positioned at desired points in space. Many applications like tracking radar, search radar, remote sensing, and communications benefit from planar arrays.

Considering as a linear array of linear arrays, the array factor of a planar array can be derived. Referring to the planar array configuration in Figure 2.2 and according to (2.2), M elements placed along the x axis has an array factor of

$$AF_x = \sum_{m=1}^{M} a_{m1} e^{j(m-1)(kd_x sin\theta cos\phi + \beta_x)}, \qquad (2.14)$$

where a_{m1} represents the excitation coefficients of the elements that are placed along the x axis, d_x represents the spacing, and β_x represents the progressive phase shift between elements in the x direction. If N such arrays are placed along y direction with spacing d_y and progressive phase β_y, the planar array configuration in Figure 2.2 is obtained and the corresponding array factor can be derived as

$$AF = \sum_{n=1}^{N} a_{1n} \left[\sum_{m=1}^{M} a_{m1} e^{j(m-1)(kd_x sin\theta cos\phi + \beta_x)} \right] e^{j(n-1)(kd_y sin\theta sin\phi + \beta_y)}, \qquad (2.15)$$

which is also equal to

$$AF = AF_x AF_y. \qquad (2.16)$$

For a uniform planar array, where excitations of elements are identical in magnitude, according to (2.3), (2.5), (2.15), and (2.16), the normalized array factor can be written as

$$(AF)_n = \frac{1}{M}\left[\frac{\sin\left(\frac{M}{2}\psi_x\right)}{\sin\left(\frac{1}{2}\psi_x\right)}\right]\frac{1}{N}\left[\frac{\sin\left(\frac{N}{2}\psi_y\right)}{\sin\left(\frac{1}{2}\psi_y\right)}\right], \qquad (2.17)$$

where

$$\psi_x = kd_x\cos\theta + \beta_x \qquad (2.18)$$

$$\psi_y = kd_y\cos\theta + \beta_y. \qquad (2.19)$$

2.1.4. Mutual Coupling in Arrays

By the nature of antennas, if an antenna is transmitting energy, another one may receive some of this energy, and may even reradiate. The phenomenon of the interaction and energy interchange between antennas is called mutual coupling. Mutual couplings naturally occur in antenna arrays and usually they are not negligible. Due to mutual couplings, design difficulties in antenna arrays arise since array elements cannot be treated as they are independent of each other. Thus, the contribution of an array element to the array pattern does not only depend on its individual excitation but also on its parasitic excitation due to other array elements. Mutual couplings depend on the type of array elements and their positioning [5].

There are several approaches to estimating or modeling mutual couplings. One of them, which is an approximation for large arrays, is infinite array approach. This approach assumes that the array is infinite and identical array elements are positioned regularly. Then, by simulating antenna elements with periodic boundary conditions, element patterns and scattering parameters can be obtained and combined. The actual

behavior of the elements in large arrays is practically very similar to that of the infinite array element [6].

2.2. Waveguide-Fed Slot Arrays

Watson invented the waveguide-fed slot array antennas with related work by Stevenson, Cullen, and others in Britain during World War II [7]. Since then, they are widely used in many radar, communications, and navigation applications. Geometric and fabrication simplicity, convenience to build large arrays for high directivity, ability to achieve low side-lobe levels, efficiency, capability to handle high power, and durability of these arrays make them ideal solutions for these applications.

2.2.1. Waveguide Slots

Waveguide-fed slot array antennas are phased array antennas with radiating slots that are cut on the walls of waveguides. Slots interrupt the flow of current and induce electric field across apertures leading to radiation. Current flow cannot be interrupted with narrow slots parallel to current flow. Only when there are surface current components perpendicular to the opening at the slot location, the current flow can be interrupted and radiation becomes possible [8].

The normalized field components for a waveguide excited by a dominant TE_{10} mode travelling in the $+z$ direction, whose dimensions and current distribution are shown in Figure 2.4, are given as [9]

$$H_z = j\cos\left(\frac{\pi x}{a}\right)e^{-j\beta_g z} \qquad (2.\ 20)$$

$$H_x = -\frac{\beta_g}{\pi/a}\sin\left(\frac{\pi x}{a}\right)e^{-j\beta_g z} \qquad (2.\ 21)$$

$$E_y = -\frac{\omega\mu_0}{\pi/a}\sin\left(\frac{\pi x}{a}\right)e^{-j\beta_g z}, \qquad (2.\ 22)$$

where

$$\beta_g = \sqrt{(k_0)^2 - \left(\frac{\pi}{a}\right)^2} = \frac{2\pi}{\lambda_g}. \qquad (2.\ 23)$$

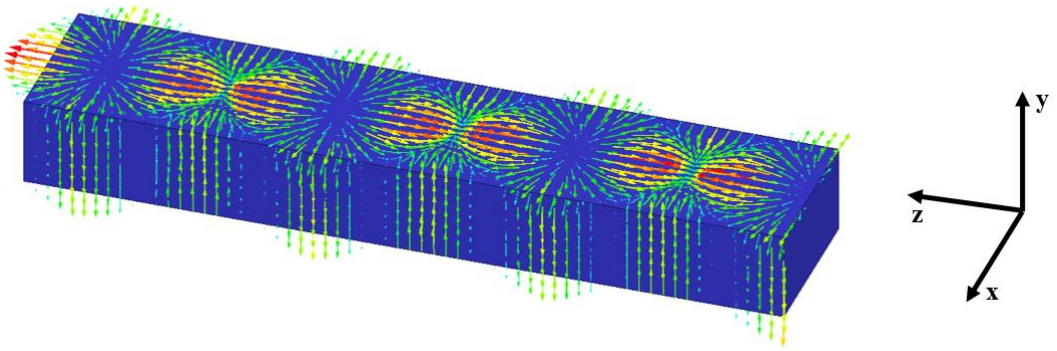

Figure 2.4. TE_{10} mode current distribution.

Various types of slots can be used in order to create a waveguide-fed slot array antenna. Some of these are shown in Figure 2.5.

Longitudinal offset broadwall slots parallel to the waveguide centerline (labeled a in Figure 2.5) are the most widely used slot types. As seen in Figure 2.4, the transversal current component is zero along the centerline of the waveguide such that slots along the centerline do not radiate. However, an offset slot can induce electric field and radiate. Increasing the offset increases the induced field. This kind of slots can be modelled as shunt elements. Although an inclined broadwall slot is located along the centerline of the broadwall (labeled b in Figure 2.5), it can interrupt the current flow due to its inclined nature. As the inclination angle increases, induced electric field also increases. This kind of slots can be modelled as series impedances.

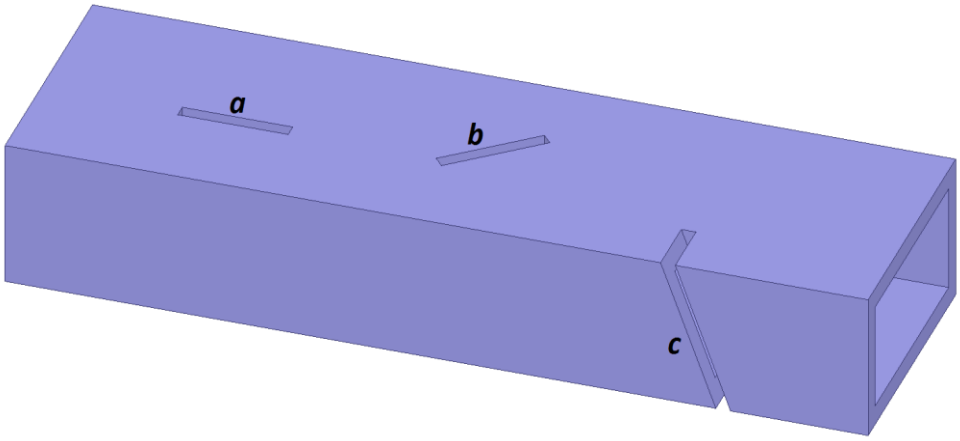

Figure 2.5. Slot types.

An inclined edge wall slot (labeled c in Figure 2.5) can interrupt the transversal current on the narrow wall. If the slot is not inclined, it is not possible to induce electric field since the current is not interrupted. The intensity of induced electric field increases with inclination. This kind of slots can be modelled as shunt elements. Generally, these slots are wrapped around waveguide corners to make the slots longer to obtain purely real admittances.

2.2.2. Waveguide-to-Probe Transitions

Waveguide-to-coaxial-line transitions are very common in microwave systems and a typical transition is shown in Figure 2.6. This transition is known as E-plane (probe) coupling and generally used to feed the waveguide. In mm-wave applications, waveguide-to-microstrip transitions are preferred in order to avoid high losses in coaxial-to-microstrip transitions. In [10], waveguide-to-microstrip probe that is developed from coaxial probe is designed. Microstrip is placed inside the waveguide through a slot to get power from the waveguide as shown in Figure 2.7. In [11], a probe consisting of a metal strip between two dielectric layers is inserted into a longitudinal rectangular slot at the centerline of the broad wall of a waveguide to

couple energy from the waveguide to radiating elements, which are linearly tapered slot antennas, as shown in Figure 2.8.

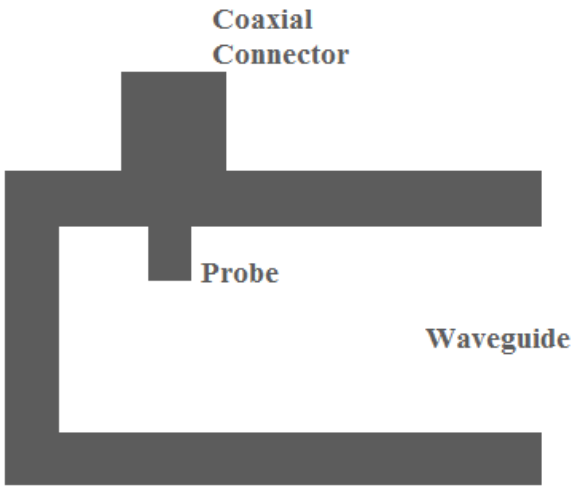

Figure 2.6. Coaxial-line-to-waveguide transition.

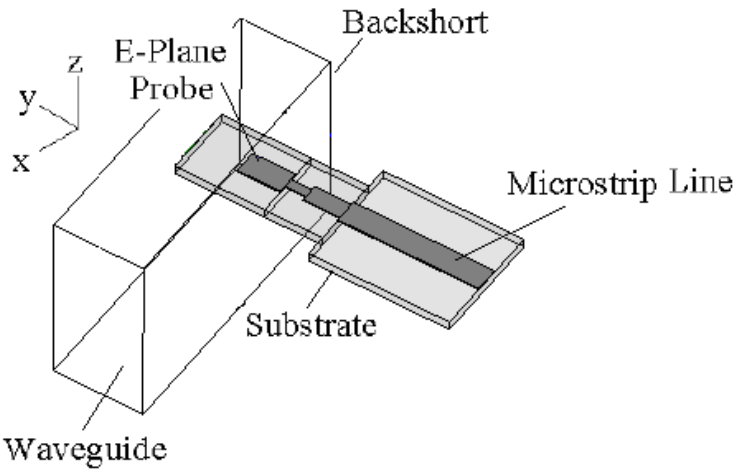

Figure 2.7. Waveguide-to-microstrip transitions. Reprinted from "A broadband W-band E-plane waveguide-to-microstrip probe transition" by Ma, X., & Xu, R., 2008, *9th Asia-Pacific Microwave Conference*, © 2008 IEEE.

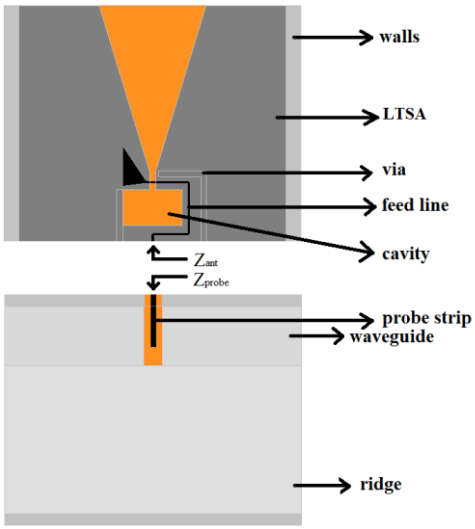

Figure 2.8. Radiating element connected to a waveguide via a probe. Reprinted from "Monopulse wideband waveguide based travelling wave array antenna" by Gültepe, G., 2017, M.S. thesis, Middle East Technical University.

2.2.3. Types of Waveguide-Fed Slot Arrays

There are two main classes for waveguide-fed slots arrays, i.e., standing-wave (resonant) and travelling-wave.

2.2.3.1. Standing-Wave (Resonant) Waveguide-Fed Slot Arrays

Elements of standing-wave arrays are excited by standing waves within the waveguide. The elements (slots) are placed with $\lambda_g/2$ separation and at alternating positions that create 180° phase difference between consecutive elements, in order to create in-phase excitation across the elements. The array can be fed either from the end or center of the waveguide. For both end-fed and center-fed approaches, the array is terminated with a short circuit termination, which is at $\lambda_g/4$ distance from the first end slot. At the center frequency, voltage maxima occur at in-phase excited slots and the array radiates broadside. As the center frequency changes, the resonance deteriorates rapidly, while pattern distortion and impedance mismatch occur [8].

2.2.3.2. Travelling-Wave Waveguide-Fed Slot Arrays

In general, voltage or current distribution of travelling-wave antennas can be described by one or more travelling waves [2]. Travelling-wave waveguide-fed slot arrays are fed from one side, while the energy is radiated from the slots along the waveguide and dissipated at a matched load at the other end. Standing-wave conditions are avoided and a resonant behavior is not observed. These arrays are used in applications that require operation over a frequency band or frequency scanning.

For a uniform-spaced travelling-wave waveguide-fed slot array with element spacing d, the phase difference between the slots can be written as

$$\beta = \beta_g d. \qquad (2.24)$$

As stated, after some energy is coupled to a slot, remaining energy is transferred to other slots and the load. Since the last slot cannot radiate 100% of the power transferred but radiate the power coupled to the slot, there exists some amount of power that has to be absorbed by the matched load. Since the incident power on slots decreases towards the load, better coupling is necessary for the slots near the load. For an N slot array, assuming the waveguide is lossless and the reflection coefficient due to each slot is minimal, the amount of coupling is defined with slot conductances as

$$g_n = \frac{P_n}{P_L + \sum_{k=n}^{N} P_k}, \qquad (2.25)$$

where g_n is the conductance of the n^{th} slot, P_n is the normalized radiated power from the n^{th} slot, and P_L is the power dissipated at the load [8].

2.3. Beam Scanning

In many applications, maximum radiation is desired to be directed normal to the array. However, the main beam of an antenna array may also be steered to desired angles in the visible angular range ($0 \leq \theta \leq \pi$), by controlling the progressive phase, as seen in (2.8). The angular position of the maximum of the main beam (θ_m) is called steering angle.

In many radar applications, continuous scanning that requires a continuous change of the steering angle is necessary. Beam-steerable antennas, have ability to change the angular position of radiation to the direction of interest, which is essential for many radar applications [12].

Continuous scanning may be achieved by mechanical or electronic scanning. Mechanical scanning means changing the direction of the beam by rotating the entire antenna system [1]. This type of steering is highly effective since any other characteristics of the pattern remain unchanged and constant gain is provided while controlling the beam direction [13]. However, mechanical steering is inherently slow and its usage is limited to static or slowly changing environments. Moreover, mechanical components used to rotate antenna systems are bulky and they require significant amounts of power. It is also hard to sustain a mechanical system without failures due to moving parts [12].

Although mechanically scanned antennas are widely used, requirements for rigidity, shock resistance, and rapid scanning rate that is impossible to obtain with mechanical tools lead to the interest in electronically scanned antennas [14]. Electronic scanning changes the direction of the beam almost instantaneously (in the order of microseconds) by electronically varying the phase of antenna elements while keeping the aperture fixed in space without any mechanical mechanism [15]. One method to scan the beam electronically is using phased arrays. In phased arrays, relative phases and amplitudes of excitations of individual elements determine the

array pattern, while steering is mainly controlled by varying the phases [3]. In order to control the phase of each element, phase shifters may be used. However, these shifters introduce complexity and cost. Another type of antenna arrays, namely frequency scanning arrays, that are used for electronic scanning will be discussed in detail.

2.3.1. Electronic Scanning: Frequency Scanning Arrays

Frequency scanning arrays are types of electronically scanned arrays, where the direction of radiation is controlled by changing the frequency of operation. Generally, these arrays are implemented using series feed networks as shown in Figure 2.9. Their operation depends on controlling the phases of individual elements by the phase delay along a transmission line (between the elements) that varies with the frequency of operation. In other words, a frequency-dependent progressive phase shift is generated. Since frequency scanning arrays do not require additional elements, like phase shifters, and they are completely passive, they are simple and low-cost [8].

The frequency-dependent progressive phase shift between the elements (β) of a frequency scanning array is defined as

$$\beta = \frac{2\pi f l}{v}, \tag{2.26}$$

where f is the operating frequency of the antenna, l is the length of the transmission line between the adjacent elements, and v is the velocity of propagation in the transmission line. Equation (2.26) can also be written as

$$\beta = k_g l = \frac{2\pi}{\lambda_g} l, \tag{2.27}$$

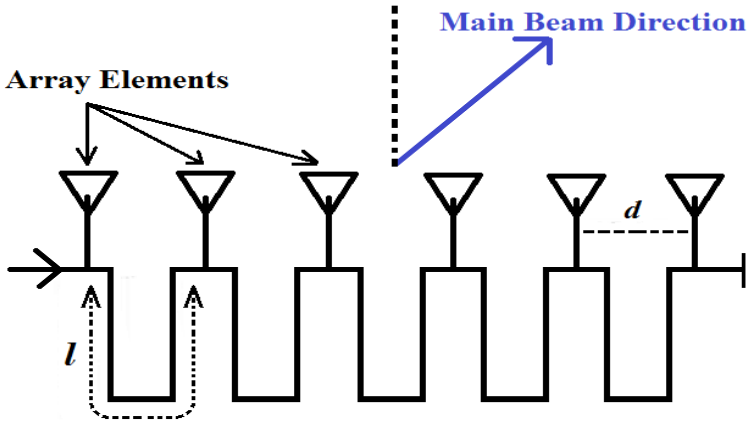

Figure 2.9. Frequency scanning array.

where k_g is the wavenumber for the transmission line and λ_g is the guided wavelength. Substituting (2.27) into (2.7), angular locations of the maxima can be found as

$$\theta_m = \cos^{-1}\left[\frac{\lambda}{d}\left(-\frac{l}{\lambda_g} \pm m\right)\right]. \tag{2.28}$$

Let λ_c be defined as the guided wavelength, where $k_c l = \frac{2\pi}{\lambda_c} l = 2\pi m$, for the frequency that creates broadside radiation, i.e., $\theta_m = 90°$. Substituting into (2.28), we obtain

$$\theta_m = \cos^{-1}\left[\frac{\lambda}{d}\left(\frac{l}{\lambda_g} - \frac{l}{\lambda_c}\right)\right] = \cos^{-1}\left[\frac{\lambda l}{d}\left(\frac{1}{\lambda_g} - \frac{1}{\lambda_c}\right)\right], \tag{2.29}$$

which is known as frequency-scan equation.

In the design of frequency scanning arrays, complexity and loss need to be considered while satisfying design requirements on scan range and frequency bandwidth [16].

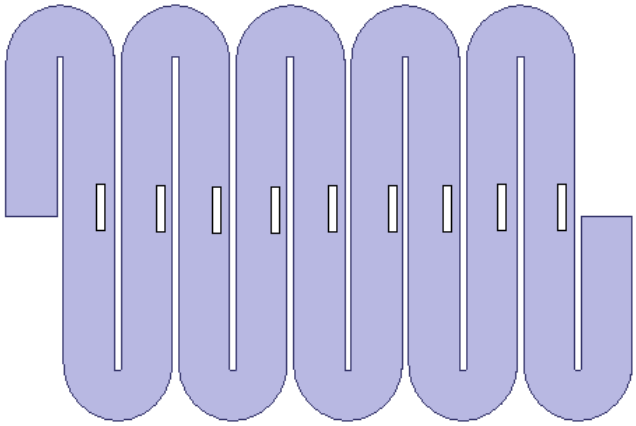

Figure 2.10. Meandered waveguide array.

2.3.1.1. Frequency Scanning With Waveguide-Fed Slot Arrays

Waveguide-fed slot arrays are very common in frequency scanning applications, e.g., see [17]-[20]. By employing waveguide-fed slot arrays in frequency scanning applications, high efficiency and low side-lobe performances can be obtained; however, these antennas are narrow band and their scan range is limited [21]. In [17], only 15° angular sector is scanned over the frequency range from 8.5 GHz to 9.5 GHz. Similarly, in [18], 17° angular sector is scanned for a frequency variation from 26.5 GHz to 30 GHz.

In order to increase the scan range of a waveguide-fed slot antenna, a meandered waveguide array illustrated in Figure 2.10 can be utilized [19], [20]. Since the excitation phases of slots are determined by the length of meandered sections l, the element spacing d can be selected independently of scan considerations. By meandering, the beam is scanned over an angular sector of 30° in the 6.6−6.9 GHz range in [19] and an angular sector of 26.4° in the 33.4−35.2 GHz range in [20].

To achieve larger scanning range and higher gain, hybrid coupling technology, which is the excitation of microstrip patches by the coupling slots of a slotted

waveguide, is applied in frequency scanning arrays [16], [21]. By this way, while high efficiency performance of the waveguide-fed slot arrays is benefited, scanning over a wide frequency band, which can provide wide scan range, can be possible. In [16], 93° angular sector is scanned for a frequency variation from 8.86 GHz to 9.88 GHz, while the peak gain is 23.2 dBi. However in this work, although 25 dB Taylor distribution is employed along frequency scan axis, relatively high side-lobe levels (−17 dB to −12.5 dB) are obtained. In [21], 61° scan range and low side lobe levels (below −25 dB) are obtained over the frequency range of 16−17 GHz with a peak gain of 29.12 dBi.

2.3.1.2. Scan Blindness Phenomenon

For travelling-wave arrays, when the elements are excited in phase, the equivalent impedances of the elements and the matched load become very large. This corresponds to reflections from each element added in phase, leading to no power transfer into the network. Because of this resonant condition, scan blindness is observed in the broadside direction, especially in arrays with large numbers of elements [17], [20].

In many studies, scan blindness phenomenon is unexamined. In [16] and [21], scan blindness phenomenon is not observed probably due to small numbers of elements in the arrays. However, if broadside radiation is required for a travelling wave array with a large number of elements, reflections from the elements need to be minimized. In [17] and [18], the scan range is determined such that the beam is not steered to the broadside to avoid scan blindness. In [21], the return loss from the input ports increases up to −3.5 dB due to scan blindness phenomenon, which results in −2.6 dB gain loss at the broadside.

For waveguide-fed slot arrays, reflection from each individual slot may be suppressed by introducing another discontinuity, called “reflection cancelling element” [20]. This element may be an additional slot [22] or a capacitive/inductive

iris [20], [23], [24]. Some examples can be seen in Figure 2.11. Because of their non-radiating structures, irises have less effect on the radiation pattern and they are more preferable than slot pairs. The discontinuity is designed such that the reflected wave due to the radiating elements is magnitude-wise equal to but 180° out of phase with the reflected wave from the discontinuity. This leads to minimization of the overall reflection coefficient of the antenna element and alleviation of the scan-blindness phenomenon [22].

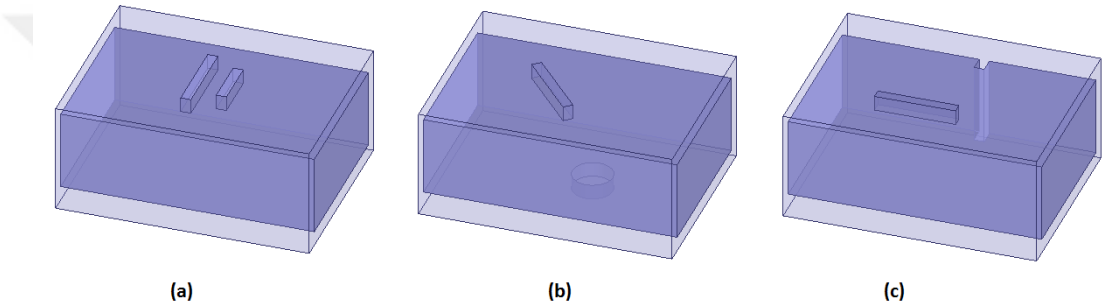

Figure 2.11. Reflection cancelling elements. (a) Slot pair, (b) circular pit, (c) inductive wall.

2.4. Tapered Slot Antennas

The idea of tapered slots was first introduced in 1960 when Eberle et al. developed a waveguide-fed flared slot antenna [25]. However, the planar-printed tapered slot antennas (TSAs), which will be considered in this section, are first are presented by Gibson [26] and Prasad and Mahapatra [27] in 1979. Since then, TSAs are commonly used for applications that require end-fire and symmetrical radiation characteristics, low side-lobe levels, moderate directivity, and broadband operations. Moreover, geometric simplicity and lightweightness make TSAs favorable [8].

2.4.1. Types and Configurations

Cutting a tapered slot from a metallized surface with or without an electrically substrate behind creates a TSA [28]. The tapered slot is the widening of a slotline, which is narrow at the feed, to form a flare. According to the shape of the tapering, the type of TSA is specified. The most common types, i.e., linearly tapered slot antennas (LTSAs), constant width slot antennas (CWSAs), and exponentially tapered slot antennas (ETSAs, also known as Vivaldi), are illustrated in Figure 2.12. In general, the functions that define the taper profile name the type of TSA.

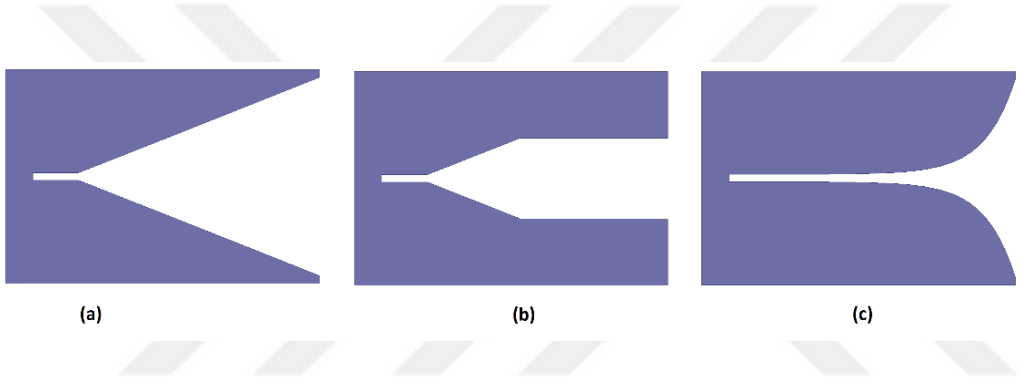

Figure 2.12. Types of tapered slot antennas: (a) Linearly tapered slot antenna, (b) constant width slot antenna, (c) exponentially tapered slot antenna.

TSA that Prasad and Mahapatra proposed [27] is a LTSA. The design is based on slotline radiation occurring due to the excessive widening of the slot. Gibson developed an ETSA, shown in Figure 2.13, as a feed for a parabolic dish reflector and named it Vivaldi. Theoretically, for an electrically large antenna, unlimited frequency bandwidth is expected since the radiating section and its vicinity remain invariant at all frequencies [26].

For a TSA, if the taper profiles are backed by a bare substrate, the configuration is called unilateral. On the other hand, if two taper profiles are separated by a substrate, the configuration is called bilateral. Moreover, these taper profiles can

be used as an antipodal layout, as well as in unilateral or bilateral configurations. In Figure 2.14, the work of Gazit [29], i.e., antipodal Vivaldi antenna configuration, is illustrated.

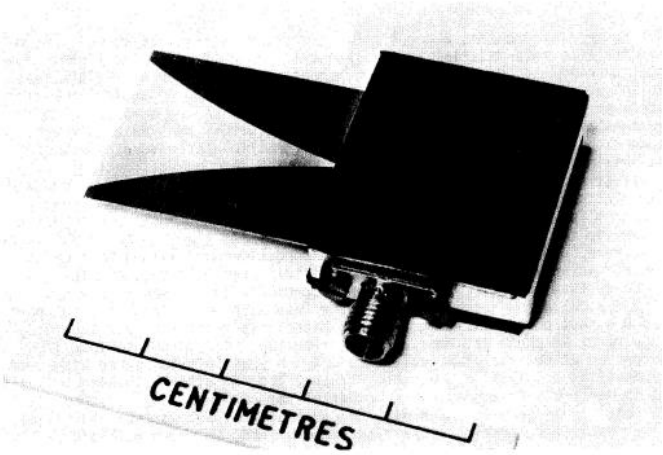

Figure 2.13. Vivaldi aerial. Reprinted from "The Vivaldi Aerial" by Gibson P. J., 1979, *9th European Microwave Conference Proceedings*, pp. 101–105. © 1979 IEEE.

2.4.2. Principle of Operation

TSAs belong to the class of travelling-wave antennas. As mentioned in Section 2.2.3.2, voltage/current distribution of travelling-wave antennas are modelled by travelling waves. Leaky-wave antennas and surface-wave antennas are two subgroups of travelling-wave antennas. TSAs are surface-wave antennas since end-fire radiation occurs from discontinuities in the structure by interrupting a bound wave on the antenna surface [4]. Surface-wave antennas let the travelling wave propagate with a phase velocity that is less than the speed of light [30]. Since a surface wave propagates parallel to an interface, radiation occurs only at discontinuities. Thus, the total radiation is mainly the superposition of the feed and terminal (antenna end) patterns [31]. By controlling diffractions on the antenna structure, TSAs can achieve wide

bandwidth operation [8]. For a TSA, different parts of the antenna radiates at different frequencies, while the electrical size of the radiating part is invariant at all frequencies [26], [29].

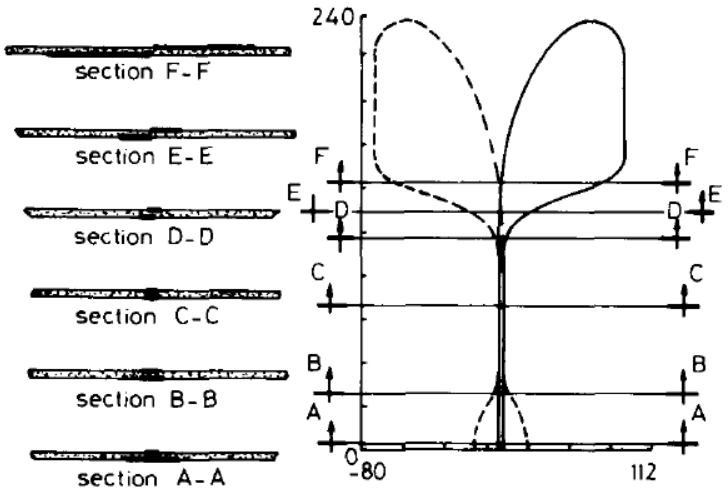

Figure 2.14. Antipodal Vivaldi antenna. Reprinted from "Improved design of the Vivaldi antenna" by Gazit E., 1988, *IEE Proceedings H-Microwaves, Antennas and Propagation*, vol. 135, no. 2, pp. 89-92. © 1988 IEEE.

The operation principle of surface-wave antennas are described in two sections, i.e., propagating section and radiating section. In the case of TSAs, the electromagnetic wave propagates along the metallization that is separated gradually according to the taper profile. The energy of the propagating waves is tightly bound to the conductors when the slot is narrow and near the feed. However, as the separation increases (slot widens) up to the order of $\lambda_0/2$, the bond becomes weaker, energy leaves the guiding structure, and radiation from the substrate end is observed [26]. In other words, some or all of the incident power that propagates along the slotline is converted into radiating power.

2.4.3. Radiation Characteristics & Related Antenna Parameters

As mentioned previously, TSAs have end-fire radiation, as a general property of surface-wave antennas. Illustration for the radiation pattern of a Vivaldi antenna is shown in Figure 2.15. For TSAs, since the electric field is induced between two tapered sections, i.e., across the slot, the radiated electric field is parallel to the antenna surface and it is linearly polarized, as shown in Figure 2.16 [28]. E-plane of an antenna is the plane containing the direction of maximum radiation and the electric field vector. Similarly, H-plane of an antenna contains the direction of maximum radiation and the magnetic field vector [2]. Despite their planar geometries, by choosing appropriate antenna parameters, TSAs can provide almost symmetric beams in E- and H- planes, as Gibson [26] obtained with the Vivaldi Aerial design [30]. However, as a disadvantage of TSAs, cross-polarization levels are typically high in the diagonal planes [32].

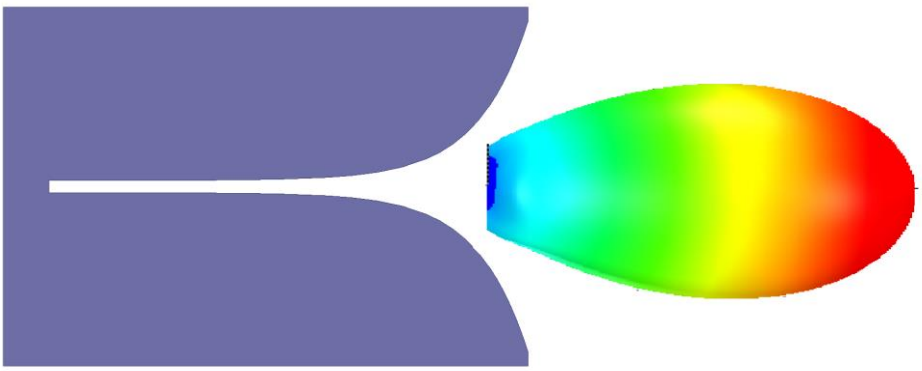

Figure 2.15. Radiation pattern of a Vivaldi TSA.

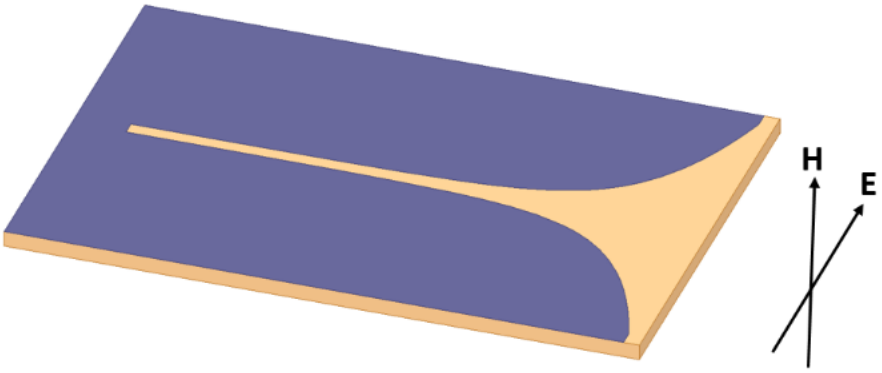

Figure 2.16. Field vectors of a Vivaldi TSA.

Taper of a TSA is very critical for the beamwidth and side-lobe levels. Three main types of TSAs are compared by Yngvesson et al [33]. While CWSAs produce the narrowest beamwidth and the highest side-lobe levels among three TSA types, Vivaldi antennas have the widest beamwidth and the lowest side-lobe levels. Increase in the electrical length of an antenna decreases the beamwidth and increases the gain. For a surface-wave antenna with length L such that $3\lambda_0 < L < 8\lambda_0$, the directivity can be approximated as $D = 10L/\lambda_0$ [8]. Proper selections of antenna length and tapering are crucial to obtain constant beamwidth in E- and H-planes [32].

Dielectric substrates are also very influential on antenna performances. Increasing the dielectric permittivity improves the low-frequency performance with respect to dielectric-free cases. However, further increases in dielectric permittivity beyond certain limits deteriorate high-frequency performances [34]. Generally, thickening the dielectric substrate results in higher gain and higher side-lobe levels. While using dielectrics of high permittivity, increasing the substrate thickness over a limit may cause undesired substrate modes that lower antenna performance [32], [33].

2.4.4. Feeding Techniques

Since a TSA is simply the extension of a slotline, feeding mechanism of a TSA consists of a transition between a slotline and another type of transmission line, which carries signals from transmitter (or to receiver) circuitry. Transitions should be low-loss over the frequency band of operation, which is usually wide. Moreover, compact and easy-to-fabricate transitions are more preferable. There are two categories for these transitions, i.e., electromagnetically coupled transitions and directly coupled transitions.

2.4.4.1. Directly Coupled Transitions

A directly coupled transition feeds TSA with a direct current path, like a wire of solder connection. The most popular directly coupled transition is coupling through a coaxial line. An illustration for a coaxial-line-to-slotline transition, from the work of Knorr [35], is shown in Figure 2.17. The main disadvantages of this type of transitions are increased profiles of the geometries and high losses at high frequencies.

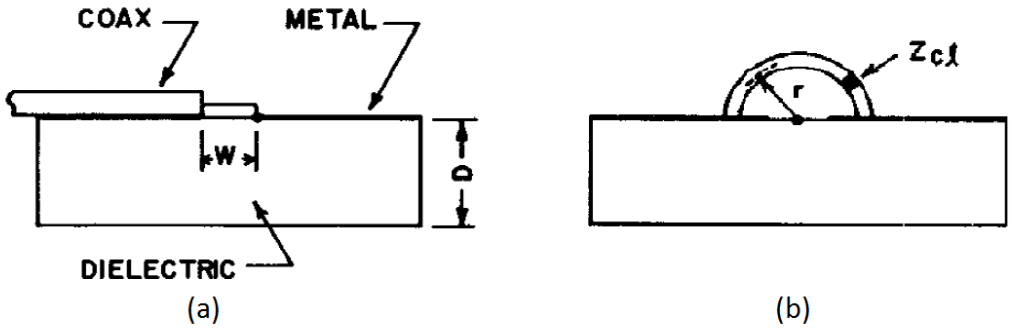

Figure 2.17. Coaxial-line-to-slotline transition: (a) side view (b) back view. Reprinted from "Slotline transitions (short papers)" by Knorr, J. B., 1974, *IEEE Transactions on Microwave Theory and Techniques*, vol. 22, pp. 548–554. © 1974 IEEE.

2.4.4.2. Electromagnetically coupled Transitions

With an electromagnetically coupled transition, the antenna is excited through the coupling of electromagnetic fields rather than a direct contact. Examples to well-known electromagnetically coupled transitions are microstrip-line-to-slotline, stripline-to-slotline, antipodal slotline, and balanced antipodal slotline transitions. Details about these transitions are shortly given below.

Microstrip-Line-to-Slotline Transition

The simplest version of a microstrip-line-to-slotline transition is the crossing of microstrip on one side of the dielectric substrate and a slotline on the ground at right angle. The termination represents short circuit for the microstrip line and open circuit for the slotline. This can be realized with various shapes [36]. For example, in the study of Schuppert [37], four different geometries shown in Figure 2.18 are investigated.

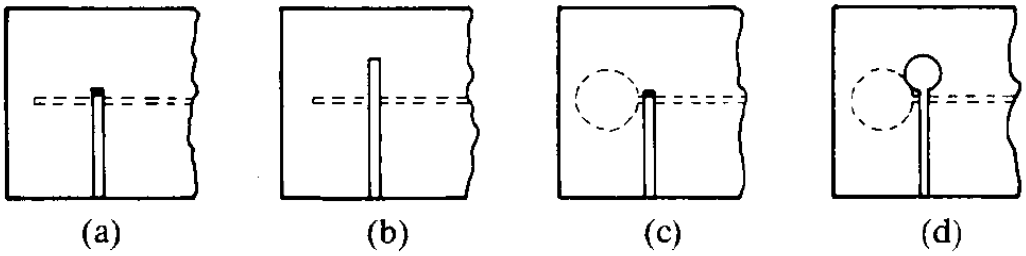

Figure 2.18. Microstrip-line-to-slotline transitions. Reprinted from "Microstrip/slotline transitions: Modeling and experimental investigation" by Shuppert, B., 1988, *IEEE Transactions on Microwave Theory and Techniques*, vol. 36, pp. 1272–1282 © 1988 IEEE.

Stripline-to-Slotline Transition

The concept of stripline-to-slotline transition is similar to the concept of microstrip-line-to-slotline transition. Like a microstrip-line-to-slotline transition, stripline and slotline crosses at right angle with proper terminations, as shown in Figure 2.19. A stripline-fed bilateral Vivaldi TSA is studied by Shin and Schaubert **[38]**.

Antipodal Slotline Transition

As mentioned previously, a TSA can be modeled as an antipodal layout. An antipodal TSA is directly fed by a microstrip feed, as shown in Figure 2.14. Since impedance matching for microstrip-line-to-slotline transition may be hard to satisfy over a wide operation bandwidth, antipodal TSAs are preferable for wideband operation [29].

Balanced Antipodal Slotline Transition

Balanced antipodal TSAs, which are fed directly by striplines, are presented by Langley et al. [39] in order to overcome poor polarization performance of antipodal TSAs. The diagram for a balanced antipodal TSA is shown in Figure 2.20.

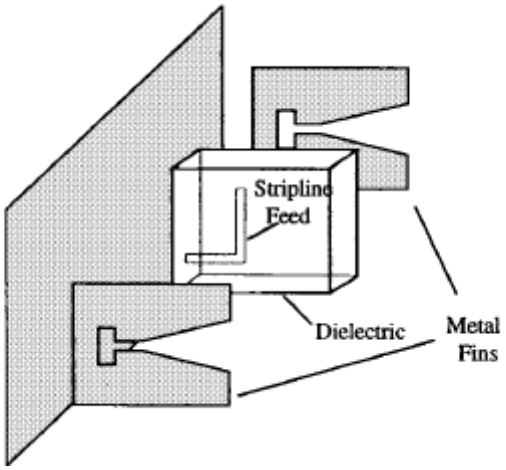

Figure 2.19. Stripline-to-slotline transition. Reprinted from "A parameter study of stripline-fed Vivaldi notch-antenna arrays" by Shin, J., & Schaubert, D. H., 1999, *IEEE Transactions on Antennas and Propagation*, vol. 47, pp. 879–886. © 1999 IEEE.

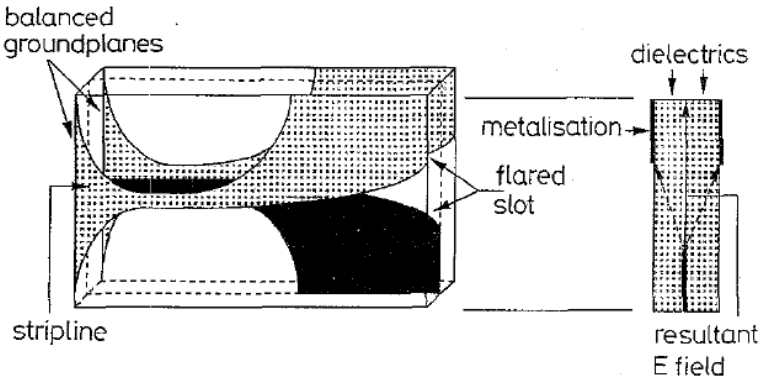

Figure 2.20. Balanced antipodal Vivaldi antenna. Reprinted from "Balanced antipodal Vivaldi antenna for wide bandwidth phased arrays" by Langley, J. D. S., Hall, P. S., & Newham, P., 1996, *IEE Proceedings-Microwaves, Antennas and Propagation*, vol. 143, pp. 97–102. © 1996 IEEE.

2.4.5. TSA Arrays

E-plane and H-plane array configurations of TSAs can be seen in Figure 2.21. In an E-plane configuration, antennas do not need to be separated, and metallization and substrate can be extended between elements. Moreover, E-plane configurations generally do not affect the return-loss performance adversely. On the other hand, in H-plane arrays, the case is the opposite. Radiation patterns of array elements are also affected by mutual couplings. Thus, during antenna design, mutual coupling effects should be taken into the consideration. For example, although a single antenna element works best with antenna size larger than a wavelength and aperture width more than a half-wavelength, the opposite is true for a Vivaldi TSA array [38].

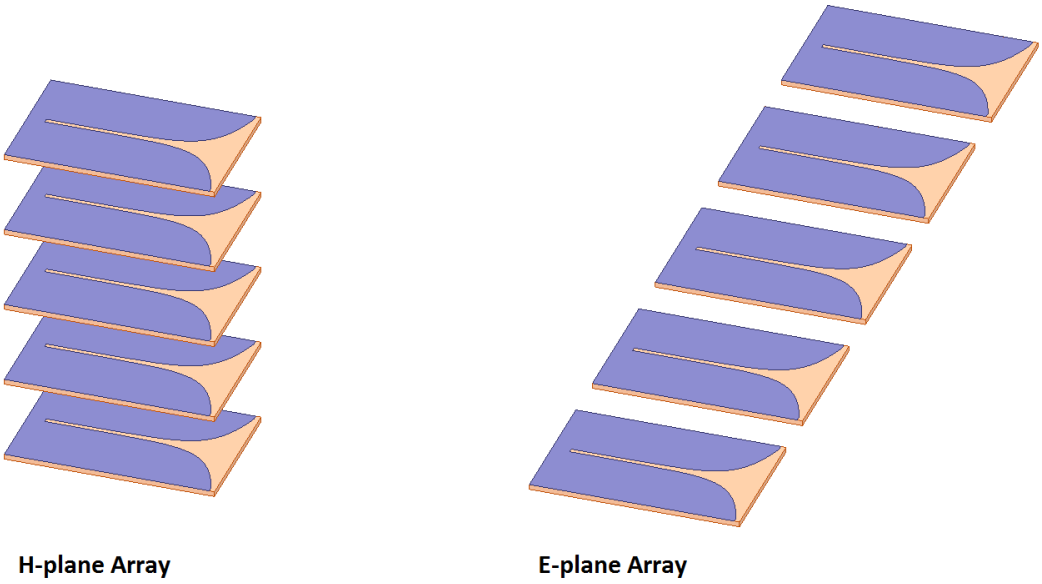

Figure 2.21. E-plane and H-plane configurations for Vivaldi arrays.

2.5. Conclusion

The proposed design in the thesis is an integration of a waveguide beamformer, which has the similar principles as waveguide-fed slot arrays, and a Vivaldi array. In this chapter, some background information for the design process of the proposed structure is given. Fundamental information on antenna array theory, waveguide-fed slot arrays, and tapered slot antennas are introduced. The importance of electronic scanning is briefly mentioned and frequency scanning with waveguide-fed slot arrays is explained considering challenges on broadside radiation. In the next chapter, the detailed design procedure for the proposed antenna is presented with simulation results in three main sections. The first section is about the generation of the pattern in azimuth axis, where frequency scanning is utilized, by employing a waveguide beamformer with stripline coupling structures. In the second section, we present a 56x8 Vivaldi array, which is fed by the stripline coupling ports of the beamformer network. In the last section, the overall design consisting of the beamformer network and the Vivaldi array is presented.

CHAPTER 3

DESIGN AND SIMULATION

As mentioned in Section 1.2, an antenna array is designed in this thesis. The array is composed of a beamforming waveguide structure utilized for frequency scanning in the azimuth axis and an array of Vivaldi elements in the elevation plane repeated along the azimuth axis. The design procedure and methodology, difficulties came across throughout the design and methods to cope with them, as well as the designed structure and its simulation results are presented in this chapter.

3.1. Generation of Azimuth Pattern

In order to realize the frequency scanning pattern in the azimuth axis, a waveguide network with stripline probes is utilized as a beamformer to feed the stripline antenna arrays in the other plane. The full-wave simulations are performed by using Ansoft HFSS®. In the simulations, the waveguide shell is modeled as aluminum and the metallizations are modelled as copper.

3.1.1. Pattern Synthesis in the Azimuth Axis

As given in Table 1.1, the antenna needs to have less than 2.3° beamwidth at broadside and side-lobe level smaller than −17 dB in the 12% frequency bandwidth, i.e., $f_{low}-f_{high}$ where $f_{low} = 0.940f_c$ and $f_{high} = 1.060f_c$ with center frequency f_c, and scanning range of 80°. The wavelength at the center frequency is symbolized as λ_c.

As explained in Section 2.1.2.1, if the element spacing does not satisfy (2.9), grating lobes are observed. In the design, it desired to avoid grating lobes in the 80° beam scanning range that can be defined as $\theta_1 \leq \theta \leq \theta_2$ such that $\theta_2 - \theta_1 > 80°$. Since scanning would not be symmetric around the broadside, assuming that $\theta_1 = 50°$ and

θ_2 = 130° and calculating element spacing accordingly leads to grating lobes at some frequencies at the ends of the frequency band. Consequently, θ_1 = 30° and θ_2 = 150° is a safe choice and an element spacing d = 0.495λ_c guarantees not to obtain a grating lobe in the visible angular range for all scanning angles such that 30° ≤ θ ≤ 150°.

As mentioned in Section 2.3.1, frequency scanning arrays can control radiation with a progressive phase shift between their elements. In the designed antenna, the beam should be scanned over an angular sector of 80° between f_{low} and f_{high}. The required progressive phase shift difference at f_{low} and f_{high}, i.e., $|\beta_{f_{low}} - \beta_{f_{high}}|$ where $\beta_{f_{low}}$ is the progressive phase shift at f_{low} and $\beta_{f_{high}}$ is the progressive phase shift at f_{high}, can be calculated by using (2.8). Some values of $|\beta_{f_{low}} - \beta_{f_{high}}|$ and the corresponding scanning ranges are listed in Table 3.1. Considering Table 3.1, it can be stated that arranging progressive phase shift between consecutive array elements at f_{low} and f_{high} with a difference greater than 230° results in a scanning range larger than 80°.

Table 3.1. Scanning ranges.

$\|\boldsymbol{\beta}_{@f_{low}} - \boldsymbol{\beta}_{@f_{high}}\|$ (°)	$\|\boldsymbol{\theta}_{m@1.060f_c} - \boldsymbol{\theta}_{m@0.940f_c}\|$ (°)
220	76.61
230	80.80
240	85.14
250	89.63
260	94.32

Half-power beamwidth of an antenna array is determined by the antenna aperture, which depends on the number of elements and element spacing, as explained in Section 2.1.2.4. Since element spacing is limited by grating lobe considerations, the beamwidth of the antenna can be decreased by increasing the number of elements.

In the antenna engineering discipline, the beamwidth is primarily determined by the electrical size of the antenna. On the other hand, it is well known that the beamwidth of an electronically scanned antenna depends on the beam direction and, as the main beam deviates from the broadside, the half-power beamwidth increases. In this study, the frequency and scan direction are interrelated through the length of the delay line and the distance between consecutive antenna elements. Therefore, at a given frequency, the number of elements cannot be determined solely by the beamwidth requirement, since the frequency for broadside radiation is not known. However, in order to get out of this viscous circle, it can be assured that the beamwidth at broadside scan does not exceed the upper limit, if the lowest frequency is assumed to scan the beam broadside at which the antenna has the smallest electrical dimension hence the widest beamwidth.

As uniform excitation results in a sinc pattern with high side-lobe levels (around -13 dB), side lobes can be suppressed by applying proper amplitude distribution (tapering) to the excitation. For the azimuth axis, Taylor line-source excitation [40] can be aimed. The synthesized pattern with the excitations equal to Taylor coefficients is an optimum compromise between side-lobe levels and beamwidth. There are three parameters that specifies the Taylor coefficients: Number of elements (n), maximum side-lobe level (SLL), and $\bar{n}$. The parameter $\bar{n}$ represents the number of sidelobes adjacent to the main lobe that are at nearly constant level defined by the maximum side-lobe level [2].

By array factor calculation including Taylor excitation coefficients for SLL = -25 and $\bar{n}$ = 3, the number of elements is selected as 56 with half-power beamwidth of 2.3° at broadside for f_{low}.

3.1.2. Single-Ridge Serpentine Waveguide Design

Rectangular waveguides are used in many applications. In a hollow rectangular waveguide, TE and TM modes can propagate. However, for each TE_{mn}/TM_{mn} mode, there is a certain frequency, called cutoff frequency, such that propagation is not possible below. Depending on the mode, cutoff frequency ($f_{c_{mn}}$) is calculated as

$$f_{c_{mn}} = \frac{k_c}{2\pi\sqrt{\mu\epsilon}} = \frac{1}{2\pi\sqrt{\mu\epsilon}}\sqrt{\left(\frac{m\pi}{a}\right)^2 - \left(\frac{n\pi}{b}\right)^2}. \quad (3.1)$$

In other words, modes having a cutoff frequency f_c such that $f_c < f$ can propagate, whereas modes having a cutoff frequency f_c such that $f_c > f$ cannot propagate at a given operation frequency f. Modes that do not propagate are called evanescent modes. The fields corresponding to these modes decay exponentially by distance.

The mode having the lowest cutoff frequency is called the dominant mode. The dominant mode for waveguides such that $a > b$ is TE_{10} (m = 1, n = 0), as in Figure 2.4. Generally, it is desired to have only one propagating mode in a waveguide. We note that expressions for electric and magnetic fields are equal to zero if m or n is equal to zero for TM modes. So, TM_{0n} and TM_{m0} modes do not exist.

As mentioned, spacing between the array elements in azimuth axis is decided to be $0.495\lambda_c$ in order to avoid grating lobes. Considering $0.055\lambda_c$ wall thickness, dimension a cannot be larger than $0.44\lambda_c$. Dominant mode TE_{10} has the cutoff frequency of $1.136f_c$ for a = $0.44\lambda_c$ and it is even higher for smaller a values. In order to have the fundamental mode propagating in the waveguide, the cutoff frequency must be decreased. This can be achieved either by filling the waveguide with an insulator material with relatively high permittivity or using ridges in an air-filled waveguide. Most of the time, using an insulator material is undesirable due to increased propagation losses and mass. Ridge waveguides can have single or double

ridges as shown in Figure 3.1. Double-ridge structures are more bulky and hard to manufacture compared to single-ridge waveguides. Thus, a single-ridge waveguide is preferred as the main signal distribution manifold in this design.

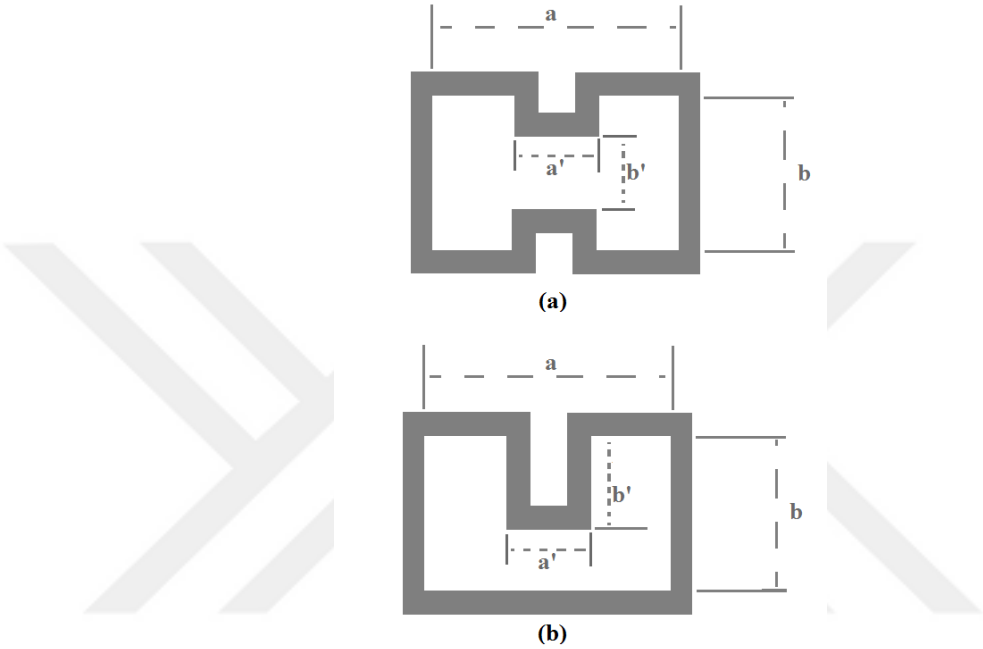

Figure 3.1. (a) Double and (b) single-ridge waveguides.

To determine the dimensions of the ridge, a' and b', several values for a' and b' are swept for the design shown in Figure 3.2, leading to the selection of these dimensions as a' = $0.110\lambda_c$ and b' = $0.138\lambda_c$. The real and imaginary parts of the propagation constant, i.e., attenuation and phase constants, are shown in Figure 3.3 in a frequency band from $0.727f_c$ to f_{high}. It is seen that, for frequencies smaller than $0.784f_c$, the propagation constant is purely real so that the mode is evanescent, while it is purely imaginary so that the mode is propagating for higher frequencies. Thus, this single-ridge waveguide design with a cut-off frequency of $0.784f_c$ is suitable for frequency band of operation.

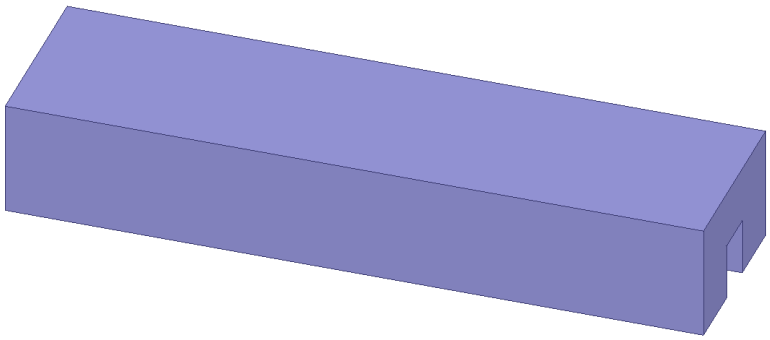

Figure 3.2. Single-ridge waveguide.

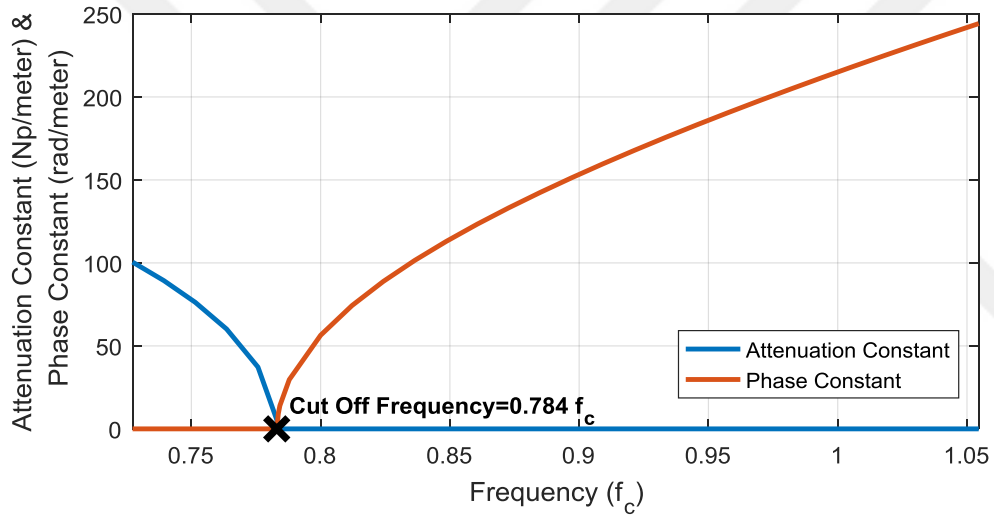

Figure 3.3. Attenuation constant and phase constant for the structure in Figure 3.2 with a' = $0.110\lambda_c$ and b' = $0.138\lambda_c$.

In order to obtain phase shifts as large as those in Table 3.1, it is not convenient to feed the array elements by an air-filled linear waveguide. The required phase shifts can only be obtained if the waveguide is filled with a high permittivity material or it is deliberately meandered between the array elements. Waveguide filling is not preferred due to various reasons mentioned above, and therefore, meandering is

utilized in this study. Meandered waveguides are realized by straight sections followed by turns. The stripline probes are to be fed via slots on the broadwall of the waveguide, which requires H-plane meandering, i.e., H-plane waveguide turns.

An H-plane turn in a single-ridge waveguide has four edges that need to be filleted as shown in Figure 3.4. To optimize the turn, the radii to fillet these edges must be carefully determined. An elementary meandered waveguide section is modeled by cascading two turns with a flat waveguide section between them. The length of the flat part of the waveguide is not determined in this section, while it is assumed to have negligible effect on the return loss of the model.

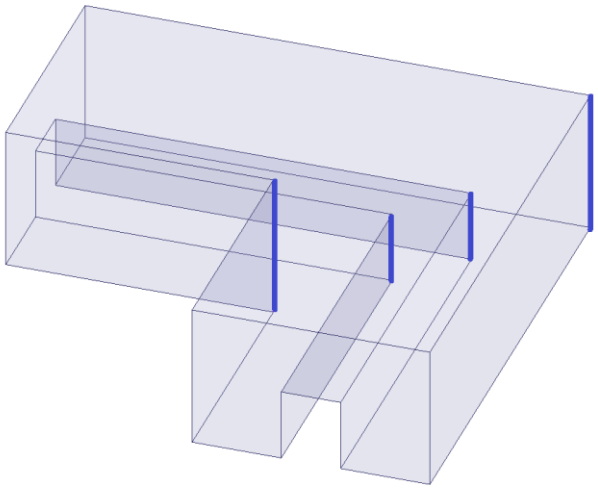

Figure 3.4. A 90° H-plane turn of a single-ridge waveguide.

The return loss of the elementary waveguide needs to be as low as possible since a large number of these sections are to be cascaded. The fillet radii are optimized to obtain a return loss smaller than -30 dB in the frequency band. The optimized model is shown in Figure 3.5 and the return loss of this model is depicted in Figure 3.6.

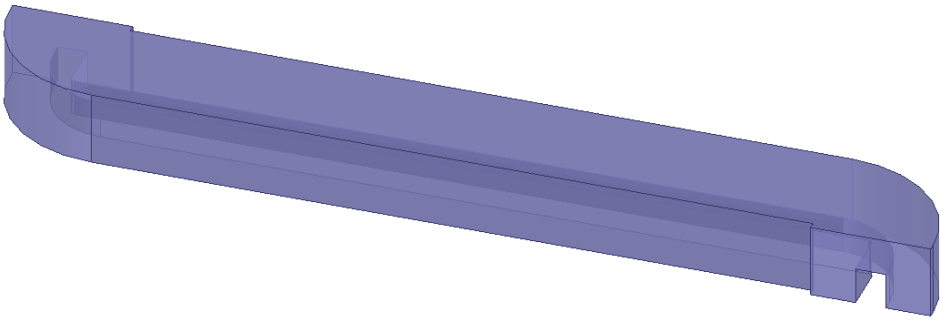

Figure 3.5. Optimized unit of a meandered waveguide.

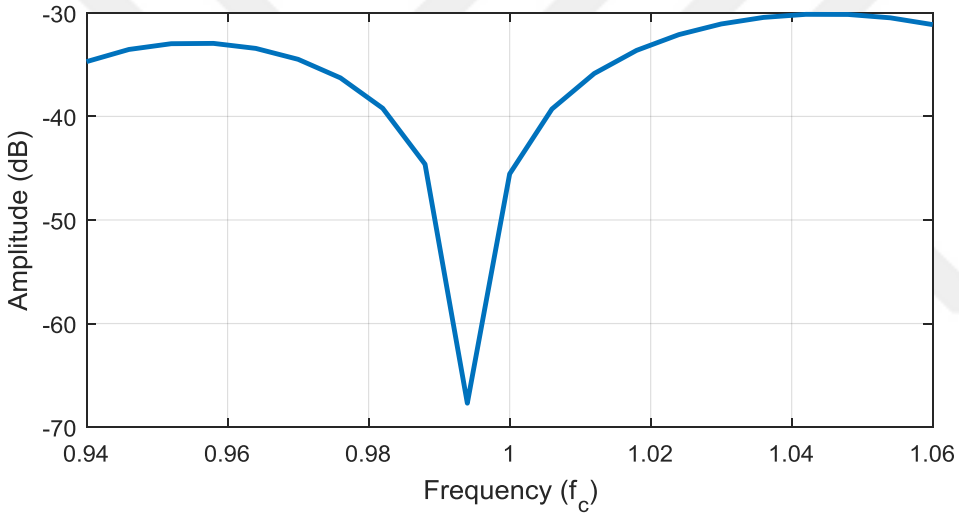

Figure 3.6. Return loss of the optimized unit of a meandered waveguide in Figure 3.5.

The length of the flat part of the model shown in Figure 3.5 is determined such that the required scanning range is obtained. In Section 3.1.1, it is stated that, in order to obtain a scanning range larger than 80°, the progressive phase difference between f_{low} and f_{high} has to be greater than 230°.

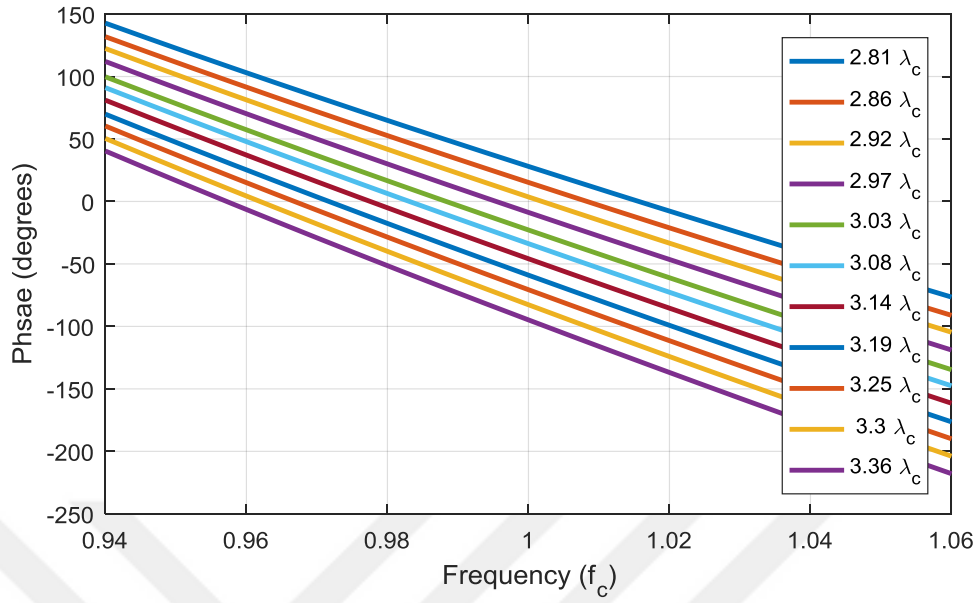

Figure 3.7. Phase of S_{21} with respect to the total length of the waveguide.

The length of the flat part is studied with respect to frequency in order to obtain progressive phase shift differences between f_{low} and f_{high}. In Figure 3.7, phase of the network parameter S_{21} ($\angle S_{21}$) is plotted, which shows the progressive phase shift with respect to frequency for different lengths of the unit waveguide. It can be observed that, the total length of $3.08\lambda_c$ creates 239° progressive phase shift difference between f_{low} and f_{high}, which creates a beam scanning range of 84°. The corresponding values of $\angle S_{21}$ with respect to frequency are listed in Table 3.2. It can be stated that broadside radiation occurs at around $0.982f_c$ (f_{bs}), since the progressive phase shift between consecutive elements is almost 0°. By applying array factor calculation with the progressive phases in Table 3.2, the patterns in Figure 3.8 are obtained. Table 3.3 summarizes the patterns in Figure 3.8 by means of the scan angle and half-power beamwidth.

Table 3.2. Progressive phase with respect to frequency.

Frequency (in terms of f_c)	$\angle S_{21}$ (°)
0.94	91.07
0.946	77.90
0.952	64.91
0.958	52.09
0.964	39.42
0.970	26.90
0.976	14.52
0.982	2.26
0.988	-9.87
0.994	-21.88
1.000	-33.78
1.006	-45.57
1.012	-57.26
1.018	-68.85
1.024	-80.35
1.030	-91.75
1.036	-103.07
1.042	-114.30
1.048	-125.46
1.054	-136.54
1.060	-147.55

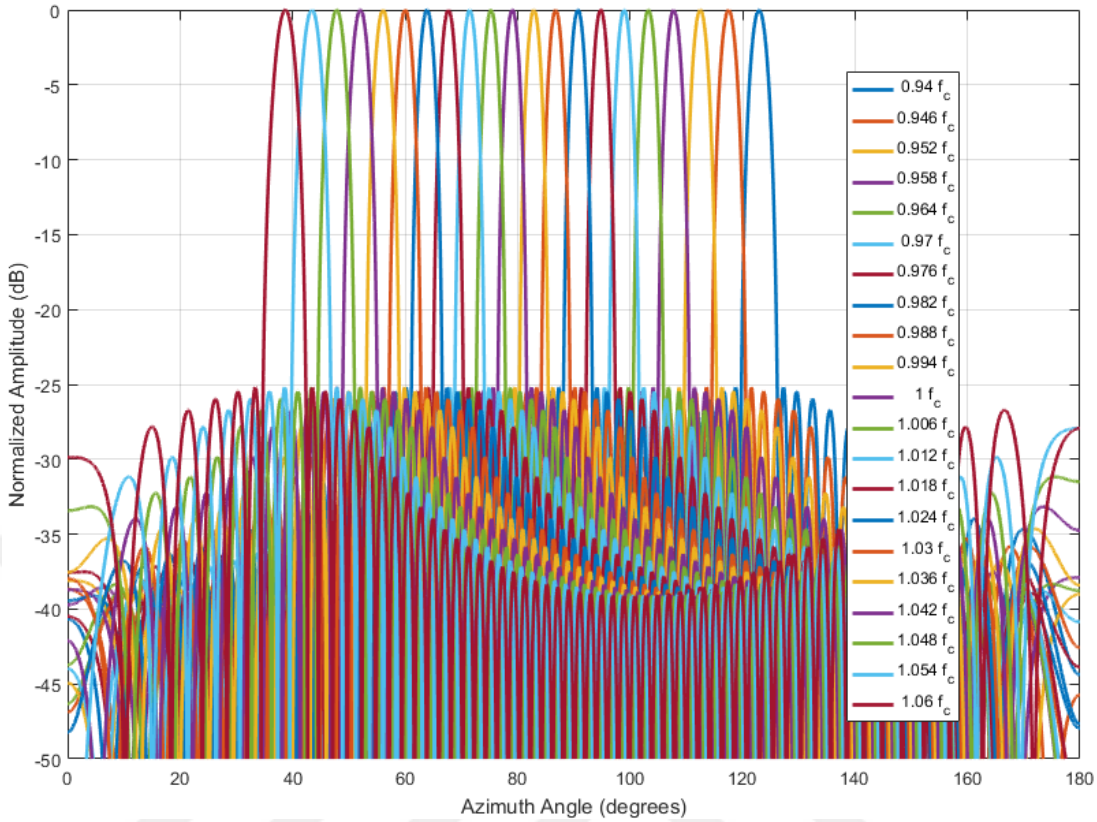

Figure 3.8. Calculated array factor for the progressive phases in *Table 3.2*.

Table 3.3. Half-power beamwidth and scan angle of the calculated array factor.

Frequency (in terms of f_c)	**Half-Power Beamwidth (°)**	**Scan Angle (°)**
0.94	2.73	122.93
0.946	2.56	117.52
0.952	2.44	112.49
0.958	2.35	107.76
0.964	2.29	103.26
0.970	2.24	98.95
0.976	2.21	94.79
0.982	2.18	90.74
0.988	2.18	86.79
0.994	2.18	82.91
1.000	2.19	79.08
1.006	2.21	75.28
1.012	2.24	71.50
1.018	2.28	67.72
1.024	2.33	63.90
1.030	2.41	60.04
1.036	2.50	56.10
1.042	2.61	52.06
1.048	2.76	47.85
1.054	2.96	43.44
1.060	3.23	38.72

3.1.3. Unit Cell Design

3.1.3.1. Single-Probe Feeding

A stripline probe is convenient to couple energy from a waveguide and transmit it to another structure. To design a 3-port unit cell with a simple stripline probe, a stripline transmission line is designed as the first step, as illustrated in Figure 3.9. Stripline width for a given characteristic impedance Z_0, relative permittivity ϵ_r, and substrate height b can be calculated analytically as [41]

$$\frac{W}{b} = \begin{cases} x & \text{for } \sqrt{\epsilon_r} Z_0 < 120\ \Omega \\ 0.85 - \sqrt{0.6 - x} & \text{for } \sqrt{\epsilon_r} Z_0 < 120\ \Omega, \end{cases} \quad (3.2)$$

where

$$x = \frac{30\pi}{\sqrt{\epsilon_r} Z_0} - 0.441. \quad (3.3)$$

Rogers 5880 with relative permittivity ϵ_r = 2.2 and height b = 0.028λ_c is selected as the dielectric material. To realize a characteristic impedance of Z_0 = 50Ω, the width of the stripline is calculated as 0.023λ_c by (3.2). In order obtain a more accurate value, the stripline geometry is simulated, where the values for the stripline width are swept at around 0.023λ_c. After simulations, the stripline width is decided as 0.0242λ_c with a characteristic impedance of Z_0 = 49.8Ω.

After designing the stripline, the stripline probe is connected to the middle of the flat section of the elementary meandered waveguide designed in Section 3.1.2. This connection is the unit cell of a 56x1 array that is responsible for assigning proper excitations to antennas for azimuth pattern. The phase of the excitation is determined by the length of the elementary meandered waveguide section as explained in Section 3.1.2, while the magnitude of the excitation is determined by coupling through the

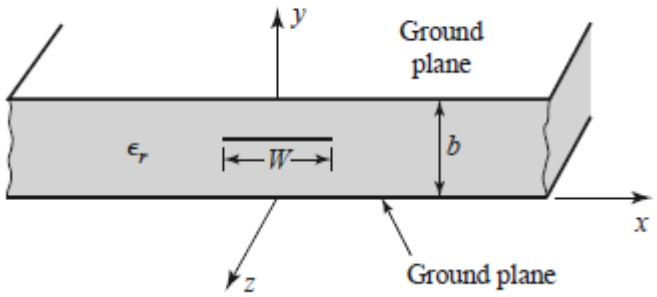

Figure 3.9. Stripline geometry. Reprinted from "Microwave engineering" by Pozar, D. M., 2011, John Wiley & Sons. © 2011 John Wiley and Sons.

stripline. The proposed model is shown in Figure 3.10. All of the walls of the probe outside the waveguide are modelled as metal. Inside the waveguide, the walls of the stripline are removed, i.e., a metal strip sandwiched into two dielectric layers is inserted into the waveguide, similar to practiced in [11].

Since the distance of the probe to the waveguide center, i.e., the probe offset, has to be the same for all elements in the array to have uniform spacing ($0.495\lambda_c$), the probe offset cannot be included in the characterization. It is observed that, as the probe gets close to the center of the waveguide, phase of S_{21} ($\angle S_{21}$), which is the source of the progressive phase between two elements, varies for different values of the probe inset length, as can be seen in Figure 3.11. This is an undesired outcome since the probe inset lengths must vary along the array, which can easily deteriorate the scanning characteristics of the array. Thus, the probe offset is selected such that the probe is close to the waveguide wall. The decided value for the probe offset is $0.1926\lambda_c$.

For different values of the probe inset length (l_{inset}), the coupling to the stripline port is different. Thus, the inset length can be defined as a characterization variable, which creates appropriate magnitude of excitation in azimuth. Coupling from the

waveguide port to the stripline port is found for different values of the inset length, and the obtained coupling values ($|S_{31}|_{dB}$) are shown in Figure 3.12. It can be observed that, as the probe enters into the waveguide, it can couple more energy. Besides, the coupling does not change too much with frequency, which is desired to maintain a frequency-stable amplitude distribution of the excitation coefficients of the antenna.

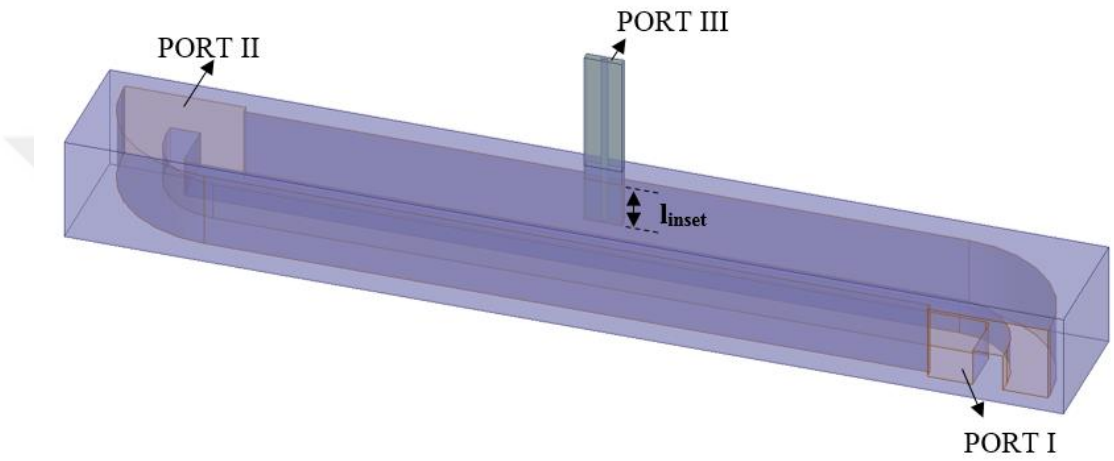

Figure 3.10. Unit cell for a single-probe feeding.

Although this design provides a good spectrum for coupling values, it has some disadvantages. First of all, since it is a reciprocal, lossless, and a 3-port network, it cannot be matched at all its ports. The behavior of $|S_{33}|_{dB}$, which represents the return loss from the stripline port, for different values of the inset length with respect to frequency is depicted in Figure 3.13. From Figure 3.13, it can be stated that this network is not matched at the stripline port. This is undesirable as it can result in degradation of the array excitation due to mismatch of the antenna and the coupling between successive antenna elements since these signals are almost completely reflected back.

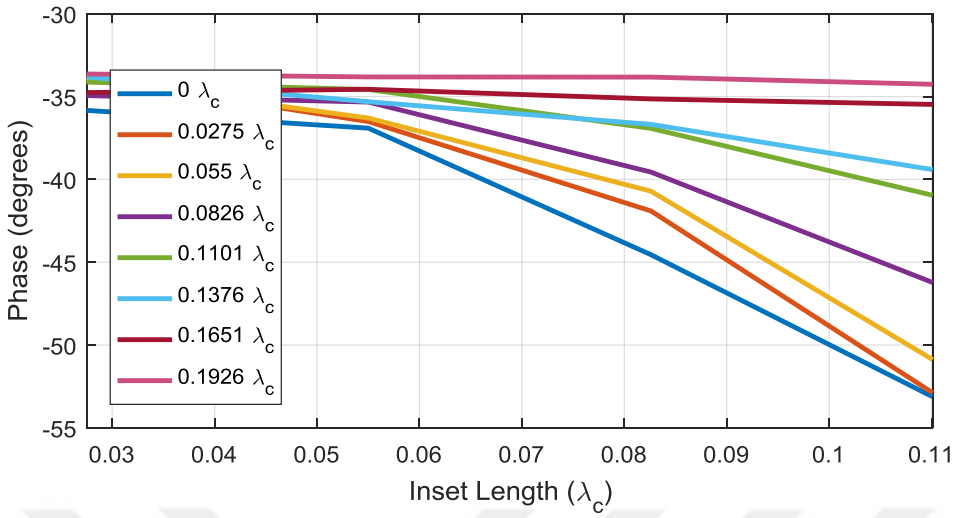

Figure 3.11. Phase of S21 with respect to the inset length for different probe offsets.

One probe significantly increases the return loss seen from the waveguide port ($|S_{11}|_{dB}$), especially for the geometries with more coupling, as shown in Figure 3.14. As mentioned in Section 2.3.1.2, low return loss for a unit cell is especially crucial for the frequency of broadside radiation (f_{bs}). At frequencies other than f_{bs}, larger values of return loss can be tolerated, as the return losses from different sections do not add coherently at the input port. However, at f_{bs}, the return losses from a large number of these units are added in-phase and result in scan blindness. To diminish the return loss of the unit cell at f_{bs}, the reflections from the probe need to be suppressed by another structure. The efforts towards this aim are presented in the next section. Although using a single-probe feeding as a unit cell is not practiced in this study, it may be useful for applications with low antenna mismatches that do not require broadside radiation or those employing less elements.

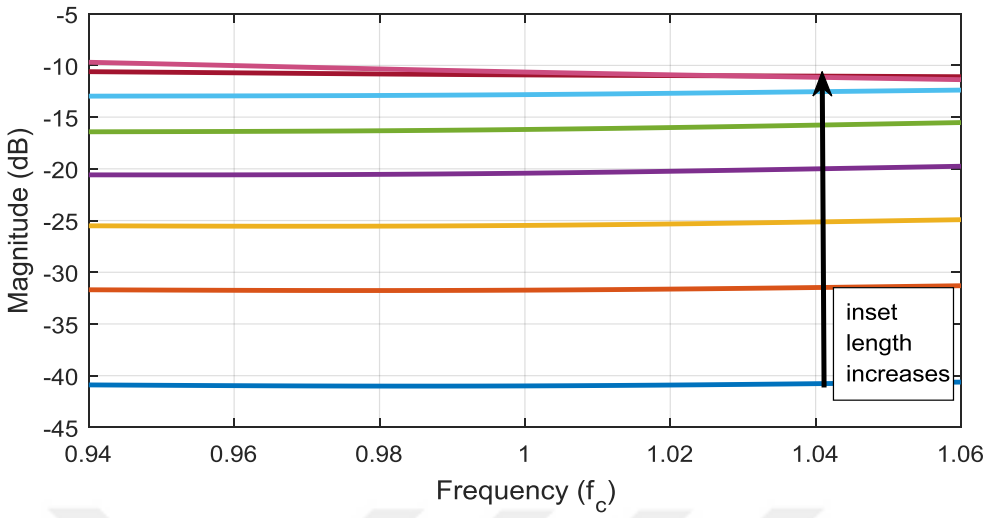

Figure 3.12. Coupling for different values of the inset length.

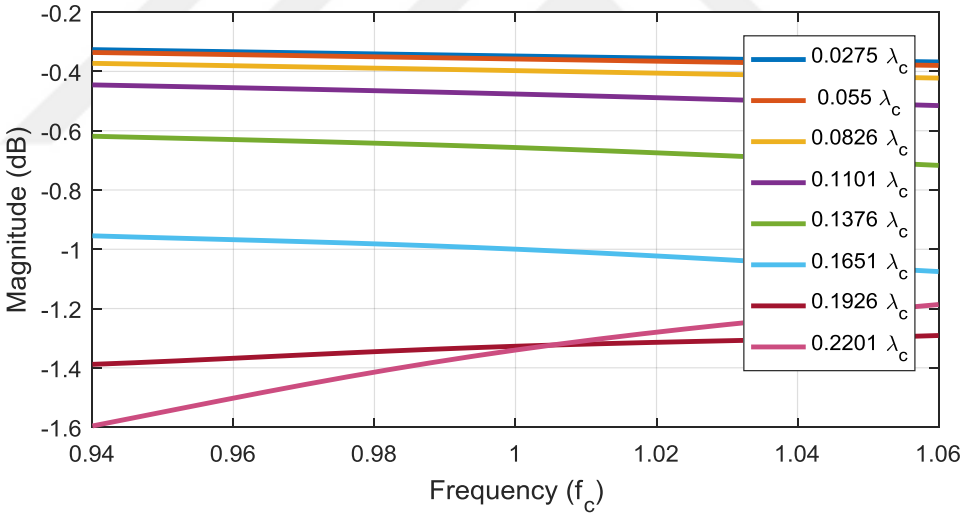

Figure 3.13. Return loss from the stripline port.

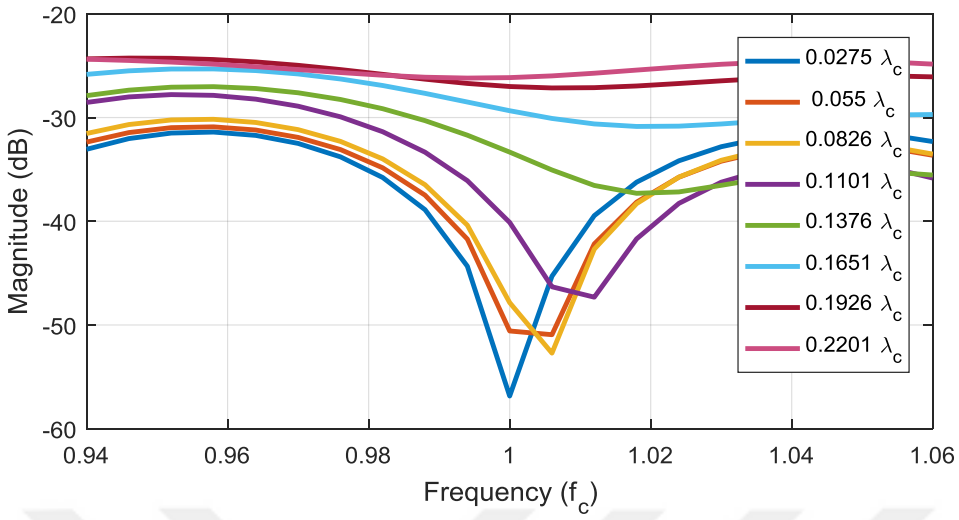

Figure 3.14. Return loss from the waveguide port.

3.1.3.2. Hybrid Coupler Feeding

First, a double-probe feeding structure is proposed by simply adding another stripline probe to the single-probe feeding structure, as shown in Figure 3.15. Assuming that the magnitudes of the reflections are almost the same, if the additional probe is positioned $\lambda_g/4$ apart from the initial probe (by two-way path length of $\lambda_g/2$), the reflections from the two arms are summed up out of phase and result in a small reflection. While port 3 (the port at the middle of the flat section) is used as the feed line for the antennas, port 4 may be terminated by a match load. This structure resolves the problem of the return loss at f_{bs}. However, as much as power delivered to the antennas is dissipated at the matched load connected at port 4. This dissipated power is considered as a loss and it is undesired.

To get rid of the disadvantages of the single-probe feeding while avoiding the loss introduced in the double-probe structure, a unit cell model with a quadrature (90-degree) hybrid coupler is introduced. The employed is a branch-line hybrid for which the scattering matrix is given as

$$[S] = \frac{-1}{\sqrt{2}} \begin{bmatrix} 0 & 0 & 1 & j \\ 0 & 0 & j & 1 \\ 1 & j & 0 & 0 \\ j & 1 & 0 & 0 \end{bmatrix}. \qquad (3.4)$$

Referring to Figure 3.16, the power entering into port 1 is evenly separated into ports 3 and 4 with a phase difference of 90° [41].

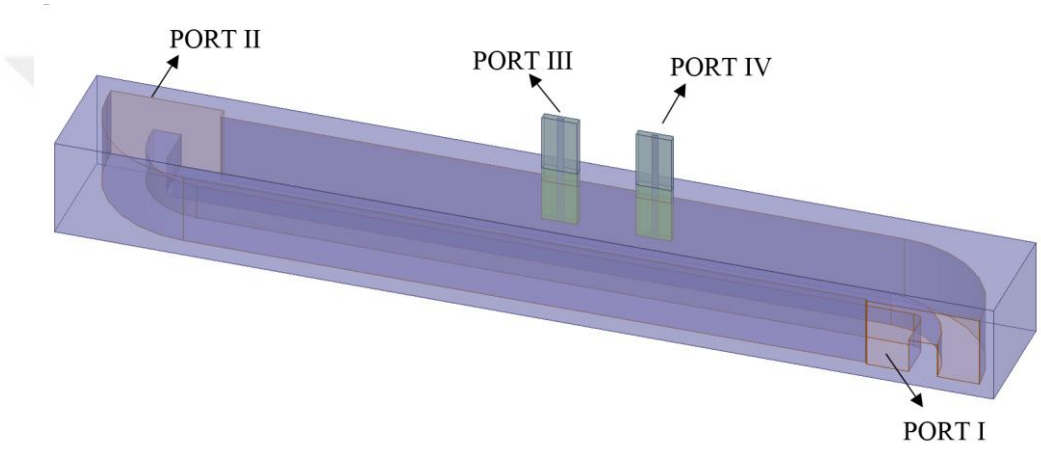

Figure 3.15. Double-probe structure.

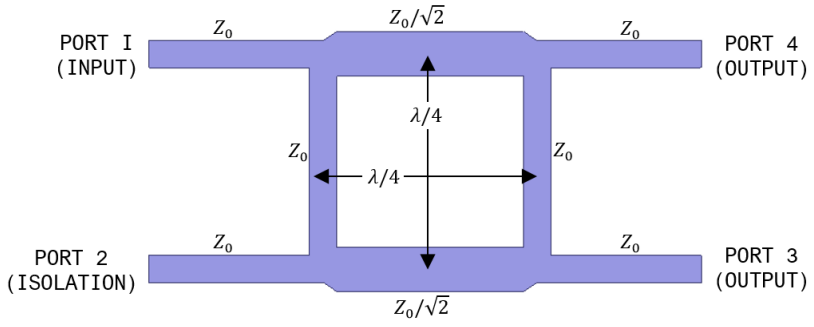

Figure 3.16. Branch-line hybrid coupler.

The branch-line hybrid coupler is connected to the waveguide similar to the single stripline probe, as shown in Figure 3.17 with related parameters. As explained for the double-probe structure, the reflections from the coupler arms that are separated by $\lambda_g/4$ are added out of phase and lead to a small reflection at the input port (port 1). Moreover, when the coupler arms are placed with $\lambda_g/4$ distance to each other, since there will be a 90° phase difference between the excitations through the first (the one that is close to port 1) and the second (the one that is close to port 2) arms, all the power captured by the hybrid coupler is transferred to port 3. Then port 4 is isolated if all ports are matched, which can be shown as

$$[b] = \begin{bmatrix} b_1 \\ b_2 \\ b_3 \\ b_4 \end{bmatrix} = [S].[a] = \frac{-1}{\sqrt{2}} \begin{bmatrix} 0 & 0 & 1 & j \\ 0 & 0 & j & 1 \\ 1 & j & 0 & 0 \\ j & 1 & 0 & 0 \end{bmatrix} . \begin{bmatrix} a_1 \\ a_2 \\ a_3 \\ a_4 \end{bmatrix}$$

$$= \frac{-1}{\sqrt{2}} \begin{bmatrix} 0 & 0 & 1 & j \\ 0 & 0 & j & 1 \\ 1 & j & 0 & 0 \\ j & 1 & 0 & 0 \end{bmatrix} . \begin{bmatrix} A \\ -jA \\ 0 \\ 0 \end{bmatrix}$$

$$= \begin{bmatrix} 0 \\ 0 \\ -\sqrt{2}A \\ 0 \end{bmatrix}, \qquad (3.5)$$

where A is the magnitude of the excitation at the coupler arms. Thus, port 4 is terminated in a matched load, while the unit cell is excited from port 1 and the energy is transferred to the antennas through port 3. Since port-4 is terminated, the unit cell may be treated as a 3-port network for the rest of the design.

With the proposed structure, it is expected to have a better-matched coupling port in comparison to the unit cell with single-probe feeding. This means that reflections from the antennas or mutual coupling signals are not reflected back to the

antenna ports but they instead leave the unit cell from the input port (port 1) substantially. Some of this reflected power is collected at the input of the array with reflections from the other antennas, while this is not a problem for frequencies other than f_{bs} since the collection is not coherent. Other portion of the power is dissipated at the matched load of port 4 of the previous element, thanks to the directional property of the proposed unit cell. In other words, reflections from the antennas vanish in the waveguide network and do not re-enter the antenna ports so that the array pattern is not disturbed. This phenomenon is illustrated in Figure 3.18, where the blue arrows show signals transmitted to and red arrows show signals reflected from the antennas.

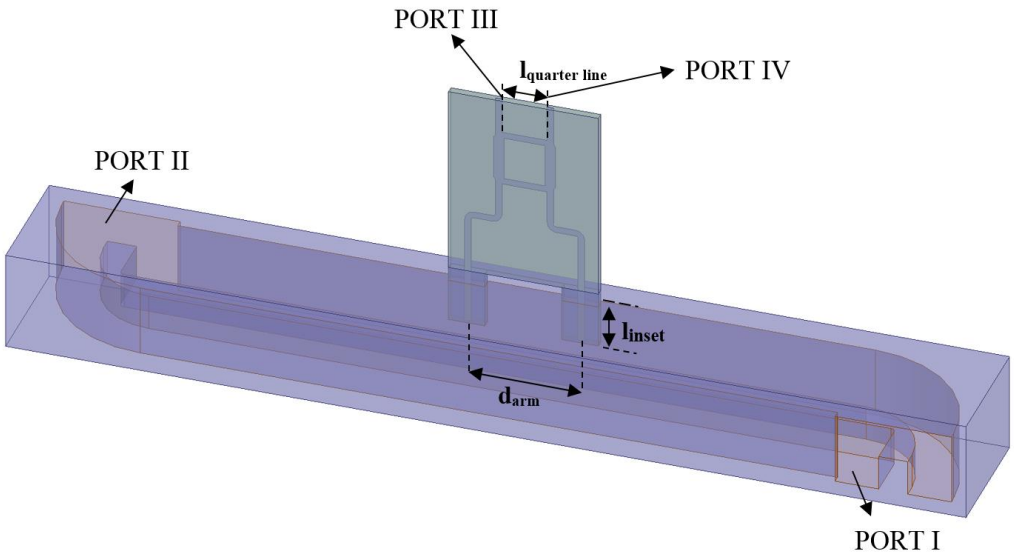

Figure 3.17. Unit cell for the hybrid coupler feeding.

In order to investigate the reflection differences between the two arms of the coupler connected to the waveguide, as well as non-idealities in the turns and transitions of the coupler geometry, the unit cell in Figure 3.17 is simulated for different inset lengths (l_{inset}) to determine proper values for separations between the

arms (d_{arm}) and quarter-wave line lengths ($l_{quarter\ line}$). Since the return loss of a unit cell is most crucial for f_{bs}, d_{arm} and $l_{quarter\ line}$ are selected as $d_{arm} = 0.429\lambda_c$ and $l_{quarter\ line} = 0.171\lambda_c$, so that the return loss of the unit cell is minimum at f_{bs} for different inset lengths. Return loss values for different inset lengths with respect to frequency are presented in Figure 3.19.

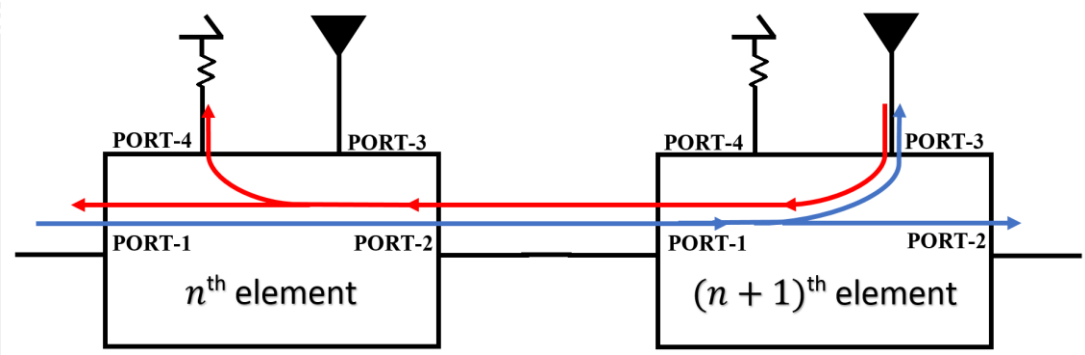

Figure 3.18. Illustration of the signals transmitted to and reflected from antennas.

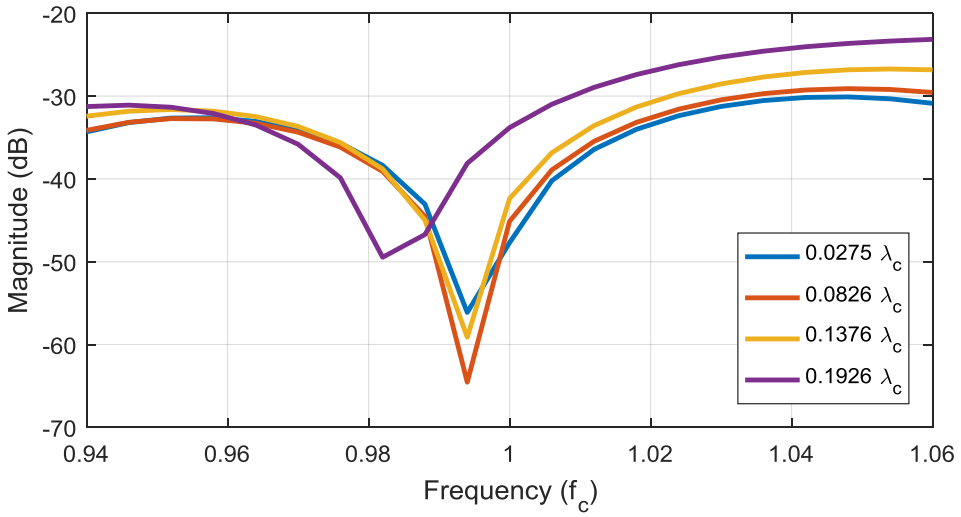

Figure 3.19. Return loss of the unit cell with hybrid-coupler feeding for different inset lengths with respect to frequency.

3.1.4. Array Design

The unit cell with the hybrid coupler feeding structure is used as an element to form the whole beamformer. A total of 56 unit cells are cascaded and terminated by a matched load at the end of the array that dissipates 5% of the input power. As mentioned, the hybrid coupler feeding delivers the required power to excite the antenna array in the elevation axis.

3.1.4.1. Characterization

To obtain the required coupling values to synthesize the desired Taylor excitation, inset lengths are swept from $0.028\lambda_c$ to $0.215\lambda_c$ with $0.011\lambda_c$ steps. The coupling values are given in Figure 3.20. It can be stated that coupling values from -37 dB to -9 dB can be obtained. Moreover, the coupling values show a flat behavior over the frequency band as in the case of the single-probe feeding structure. Coupling values monotonically increase with the length of the inset at five frequencies, which can be observed more easily in Figure 3.21.

The return loss from the input port ($|S_{11}|_{dB}$) can be seen in Figure 3.22, which is below -38 dB at f_{bs}. The return loss from the coupling port ($|S_{33}|_{dB}$), given in Figure 3.23, is very low compared to that of the unit cell with the single-probe feeding structure (see Figure 3.13), as expected.

The phase of S_{21} ($\angle S_{21}$), which corresponds to the progressive phase between the array elements, is almost the same for different values of the inset length at a specific frequency, as given in Figure 3.24. Although, the main source of the progressive phase between the elements is $\angle S_{21}$, different insets result in couplings with different phases at port 3, as can be seen in Figure 3.25. This phase error is expected to create some problems in the scanning performance of the array. However, it can easily be overcome by extending the stripline at the end of the port properly. This extension is done in a meandered fashion to preserve the alignment of the antenna elements. This process is explained in detail in Section 3.1.4.4.

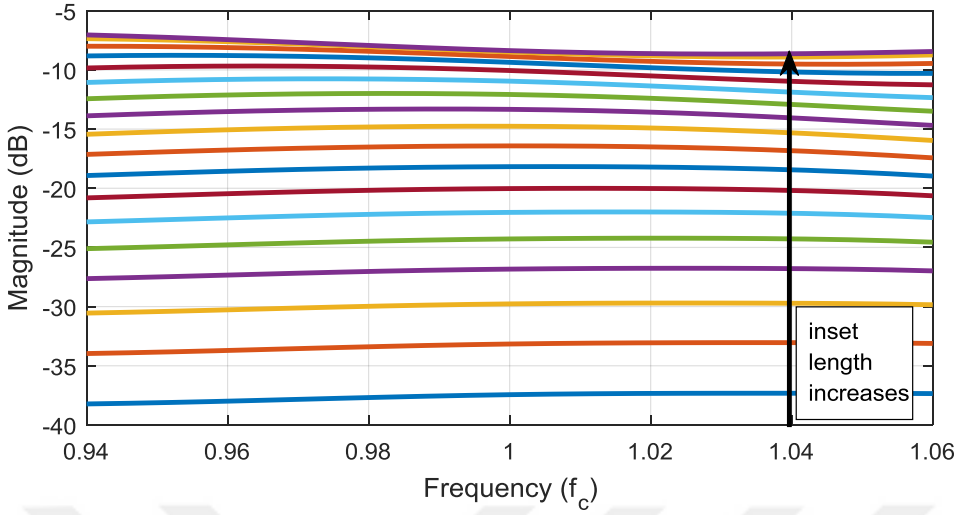

Figure 3.20. Coupling for different values of the inset length with respect to frequency.

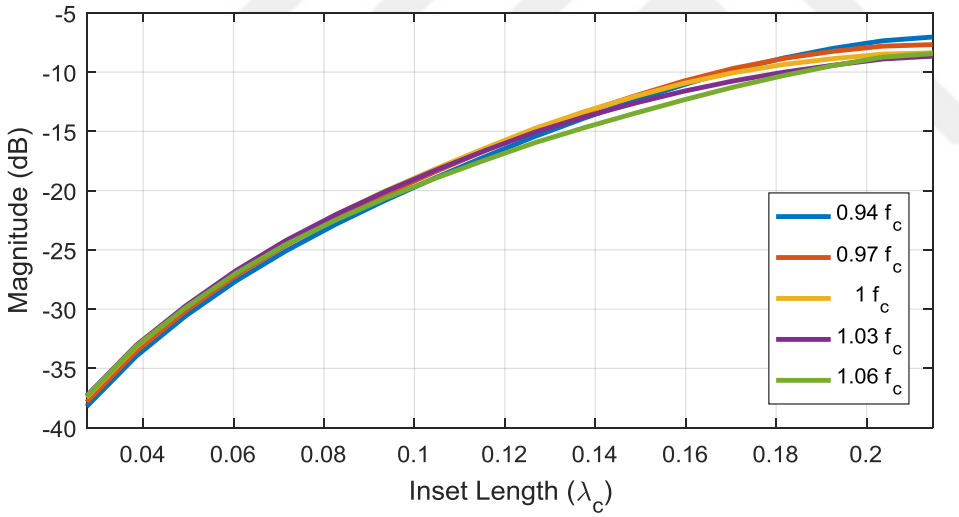

Figure 3.21. Coupling with respect to the inset length at five different frequencies.

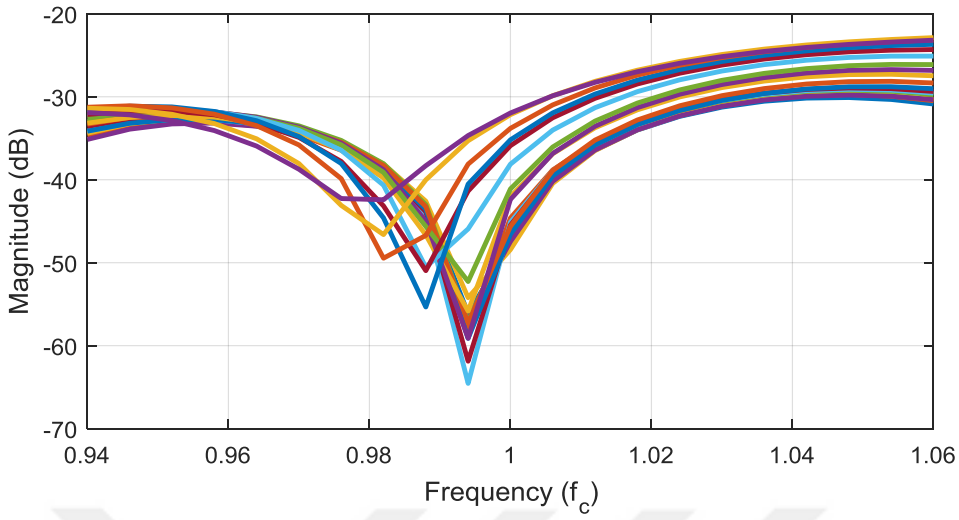

Figure 3.22. Return loss from the input port ($|S_{11}|_{dB}$) for different values of the inset length with respect to frequency.

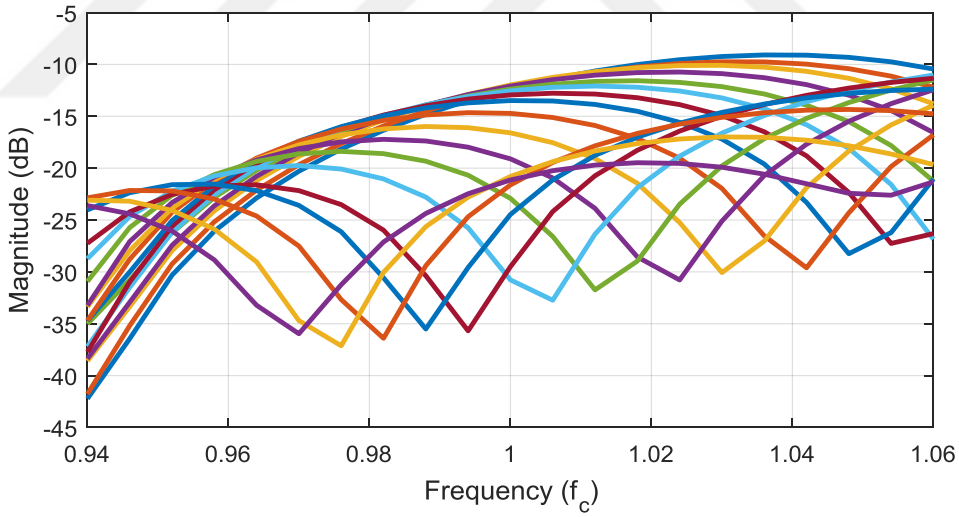

Figure 3.23. Return loss from the coupling port ($|S_{33}|_{dB}$) for different values of the inset length with respect to frequency.

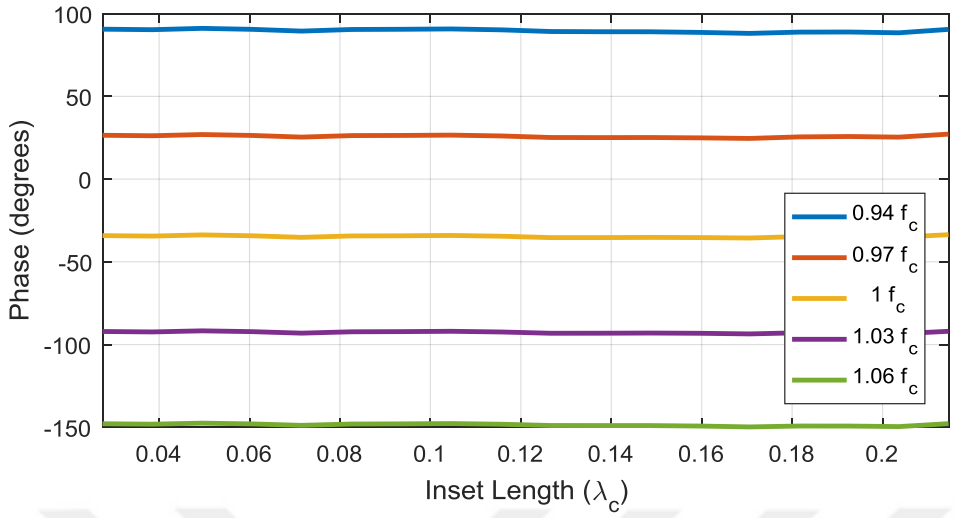

Figure 3.24. Progressive phase between the elements with respect to the inset length at different frequencies.

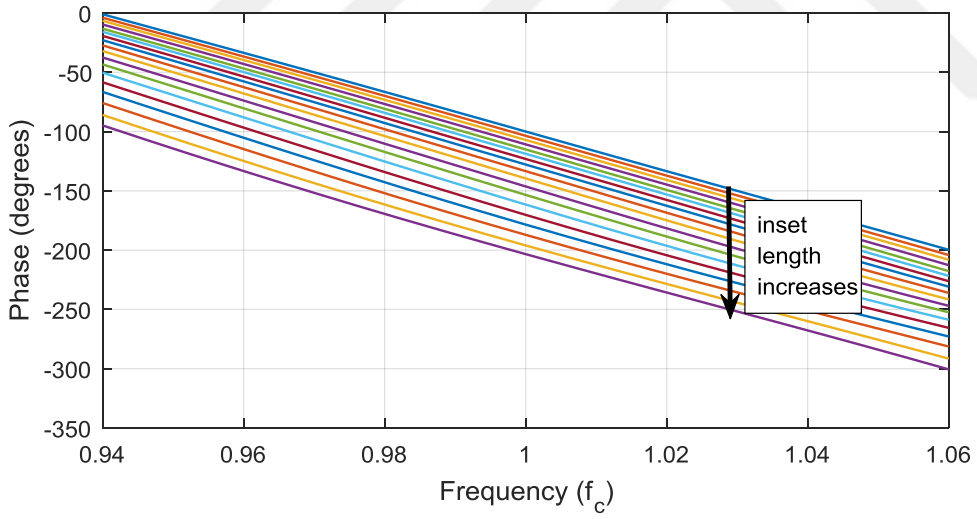

Figure 3.25. Phase of the coupled power for different values of the inset length with respect to frequency.

3.1.4.2. Initial Selection

The amount of coupling required through stripline ports can be calculated by using (2.25) for a lossless array. In order to include the losses, (2.25) is modified as

$$C_n = \frac{P_n}{P_L + \sum_{k=n}^{N} P_k + \sum_{k=n}^{N} P_{loss_k}}, \tag{3.6}$$

where C_n is the required coupling value for the n^{th} element, P_n is the power coupled to the n^{th} stripline port, and P_L is the power dissipated at the load. In addition, P_{loss_n} represents the power loss in the n^{th} element that can be written as

$$P_{loss_n} = p_{loss_n} P_{in_n}, \tag{3.7}$$

where

$$P_{in_n} = P_L + \sum_{k=n}^{N} P_k + \sum_{k=n}^{N} P_{loss_k}. \tag{3.8}$$

In the above, p_{loss_n} is the loss for the n^{th} element when the input power is equal to 1 and P_{in_n} is the power entered to the n^{th} element. In addition, p_{loss_n} can be calculated as

$$p_{loss_n} = 1 - \left(|S_{21}|_n{}^2 + |S_{31}|_n{}^2\right), \tag{3.9}$$

which is the power that is neither coupled to the stripline port nor transferred to the consecutive element, where $|S_{21}|_n$ and $|S_{31}|_n$ are the network parameters for the n^{th} element. In these equations, numbering of the elements starts from the input, i.e., 1$^{\text{st}}$ element is the one closest to the input and 56$^{\text{th}}$ element is the one closest to the matched

load. Since the determination of p_{loss_n} is not possible before selecting the elements, it is averaged for all variations that are obtained via characterization, i.e.,

$$p_{loss_{avg}} = \frac{\sum_{k=1}^{n_c}\left(1 - \left(|S_{21}|_k{}^2 + |S_{31}|_k{}^2\right)\right)}{n_c}, \qquad (3.10)$$

where $|S_{21}|_k$ and $|S_{31}|_k$ are the network parameters for each variation in the n_c-element characterization set.

The required coupling values for an array of 56 elements using Taylor line-source excitation with SLL = -25 and $\bar{n}$ = 3, as well as with 5% of the input power absorbed at the load and including averaged losses are calculated and given in Figure 3.26. The characterized S-parameters are interpolated for the inset lengths with $0.00275\lambda_c$ steps. By interpolation, inset lengths can be determined more precisely for the required coupling values. The elements are selected according to the interpolated characterization data such that the coupling for each element ($|S_{31}|$) is almost equal to the required coupling. The selection is made at f_c. Selected coupling values are given in Figure 3.27 along with the required coupling values. Unit cells, which are the elements of the 56-element array, with the selected parameters are cascaded by the formulation given in the next section to observe if the desired excitation is achieved.

3.1.4.3. Cascading

To cascade 3-port networks, which are the unit cells of the array, the used formulation is presented in this section. The configurations of the ports to be cascaded are illustrated in Figure 3.28 for three elements. Power enters each network from port 1 and is transferred to the next cell through port 2 while some coupling to port 3 occurs. In the design, port 2 of the n^{th} element is connected to port 1 of the $(n+1)^{th}$ element, while port 3 is connected to the antenna array in the elevation axis. In addition, port 1 of the first element is the input of the beamformer, while port 2 of the last (56^{th}) element is connected to the matched load.

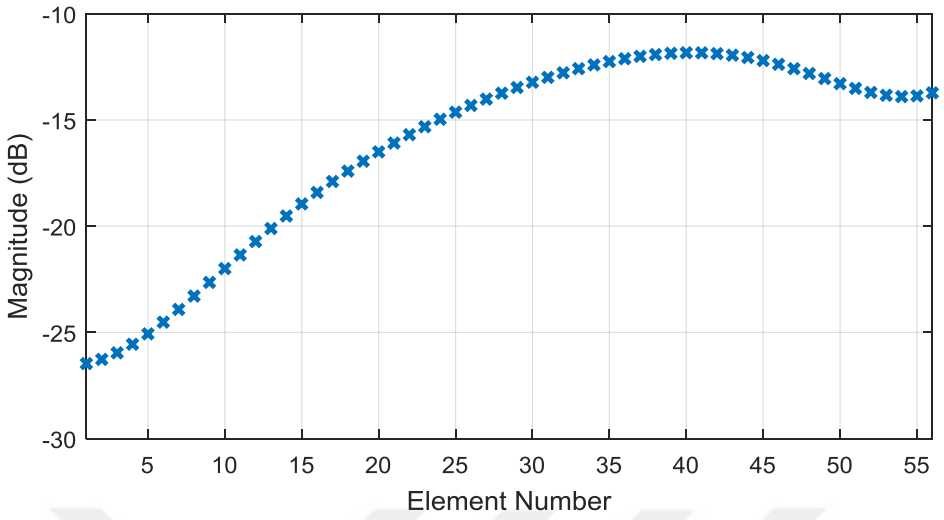

Figure 3.26. Required coupling values.

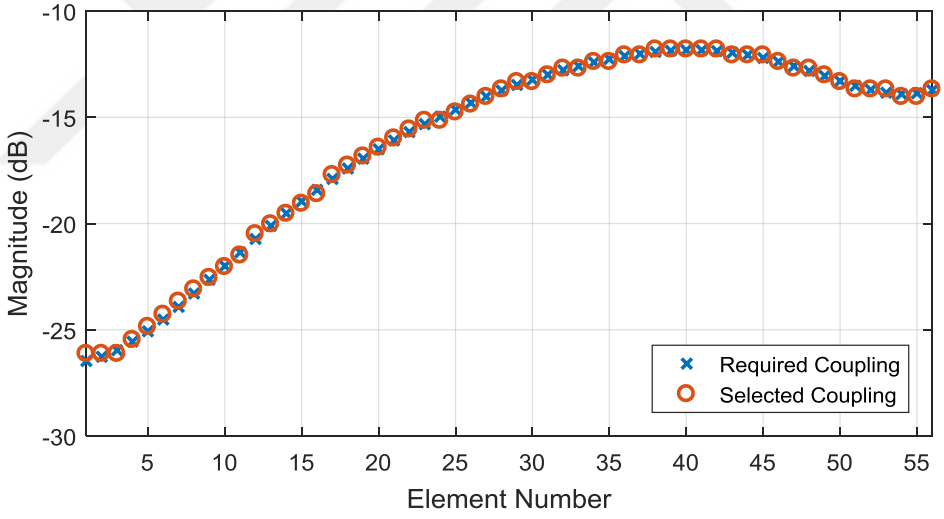

Figure 3.27. Selected and required coupling values for 56 elements.

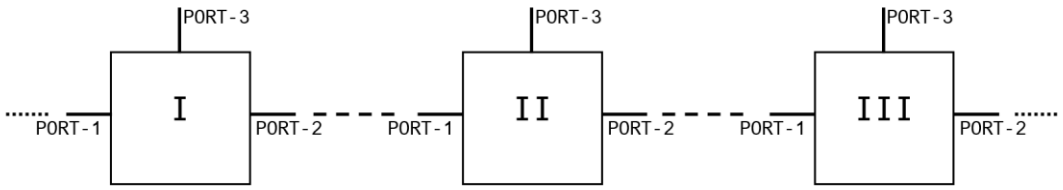

Figure 3.28. Configuration of the cascade operation.

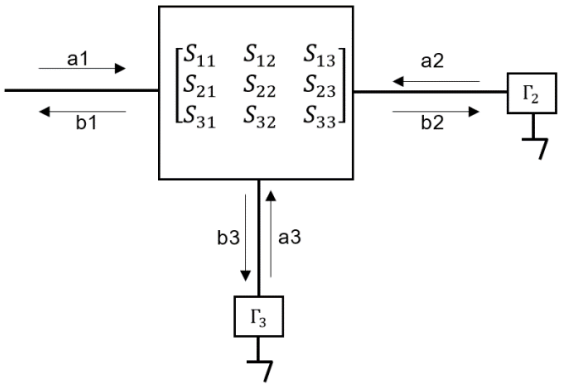

Figure 3.29. A 3-port network device.

Considering one of those elements and referring to Figure 3.29, the related S matrix can be written as

$$[b] = \begin{bmatrix} b_1 \\ b_2 \\ b_3 \end{bmatrix} = [S][a] = \begin{bmatrix} S_{11} & S_{12} & S_{13} \\ S_{21} & S_{22} & S_{23} \\ S_{31} & S_{32} & S_{33} \end{bmatrix} \begin{bmatrix} a_1 \\ a_2 \\ a_3 \end{bmatrix}. \qquad (3.11)$$

Dividing into submatrices, (3.11) can also be written as

$$\begin{bmatrix} b_1 \\ \tilde{b} \end{bmatrix} = \begin{bmatrix} S_{11} & X \\ Y & Z \end{bmatrix} \begin{bmatrix} a_1 \\ \tilde{a} \end{bmatrix}, \qquad (3.12)$$

where

$$X = [S_{12} \quad S_{13}], \quad Y = \begin{bmatrix} S_{21} \\ S_{31} \end{bmatrix}, \quad Z = \begin{bmatrix} S_{22} & S_{23} \\ S_{32} & S_{33} \end{bmatrix} \tag{3.13}$$

$$\tilde{b} = \begin{bmatrix} b_2 \\ b_3 \end{bmatrix}, \quad \tilde{a} = \begin{bmatrix} a_2 \\ a_3 \end{bmatrix}. \tag{3.14}$$

Since a_2/b_2 is equal to the reflection coefficient from port 2 (Γ_2) and a_3/b_3 is equal to the reflection coefficient from port 3 (Γ_3), $\tilde{a}$ can be written as

$$\tilde{a} = \begin{bmatrix} a_2 \\ a_3 \end{bmatrix} = \begin{bmatrix} \Gamma_2 & 0 \\ 0 & \Gamma_3 \end{bmatrix} \begin{bmatrix} b_2 \\ b_3 \end{bmatrix} = \Gamma \tilde{b}. \tag{3.15}$$

From (3.12) we have

$$b_1 = S_{11} a_1 + X\tilde{a} \tag{3.16}$$

and

$$\tilde{b} = Y a_1 + Z\tilde{a}. \tag{3.17}$$

Substituting (3.15) into (3.17), we obtain

$$\tilde{b} = (I - Z\Gamma)^{-1} Y a_1. \tag{3.18}$$

and

$$\tilde{a} = \Gamma(I - Z\Gamma)^{-1} Y a_1. \tag{3.19}$$

Finally, substituting (3.19) into (3.16), b_1 can be written as

$$b_1 = a_1(S_{11} + X\Gamma(I - Z\Gamma)^{-1}Y). \qquad (3.20)$$

By (3.18) and (3.20), knowing reflections from the coupling ports (from antennas) and from the load at the end of array, signals entering and leaving each network can be calculated.

In the following, reflections from the coupling ports and the load are assumed to be zero and the coupled powers to the stripline ports are calculated at five frequencies. This calculation gives the excitations for the arrays in the elevation axis. Excitations are given in magnitude in Figure 3.30 for five frequencies, from f_{low} to f_{high} with $0.030f_c$ steps. It is observed that there are some disturbances in the excitation pattern. To eliminate these disturbances, an optimization is performed.

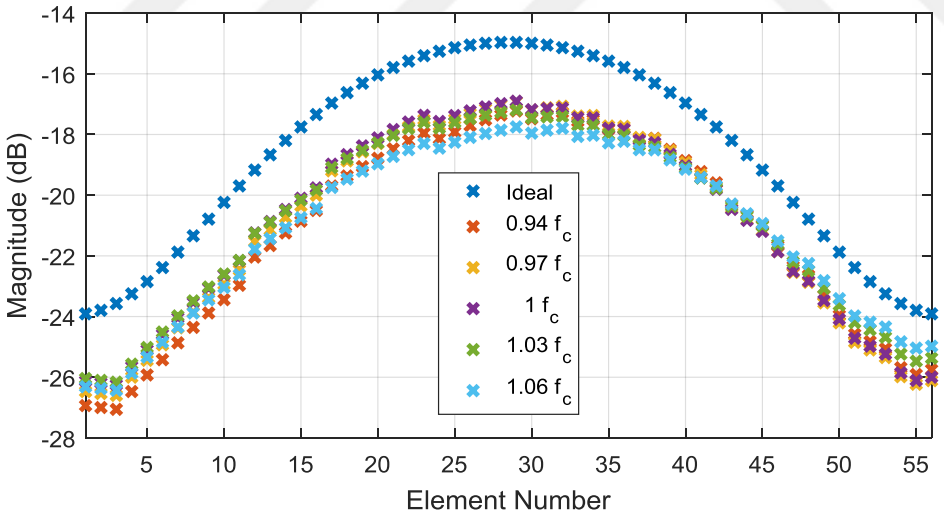

Figure 3.30. Excitation magnitudes for the initially selected elements.

Starting with initial guesses for the inset lengths, the normalized excitation magnitudes are optimized to match the ideal normalized excitation magnitudes. Minimax optimization, which seeks for a minimum of the worst-case values of a number of variables, is performed with the help of the MATLAB optimization toolbox. As stated, the inset lengths selected in Section 3.1.4.2 are used as the starting point. Bounds are specified as the minimum and maximum lengths used for the characterization, i.e., $0.028\lambda_c$ to $0.215\lambda_c$. The optimization process is very fast and an optimal solution is obtained in a few minutes. The set obtained as the output of the optimization forms the excitations given in Figure 3.31 (in magnitude) and in Figure 3.32 (in phase). Normalized excitation magnitudes for the ideal Taylor distribution, the initially selected set, and optimized set at f_c are given in Figure 3.33. It is observed that the coupling values follow the Taylor distribution. For f_c, normalized array factors calculated only by the excitation magnitudes, i.e., ignoring phase distributions, for the ideal Taylor distribution and the optimized set are compared in Figure 3.34.

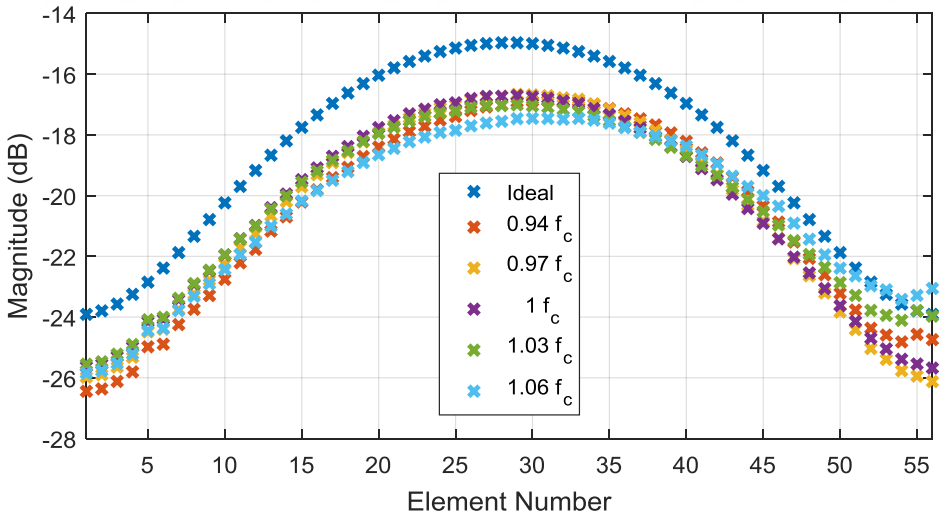

Figure 3.31. Excitation magnitude of the elements obtained by optimization.

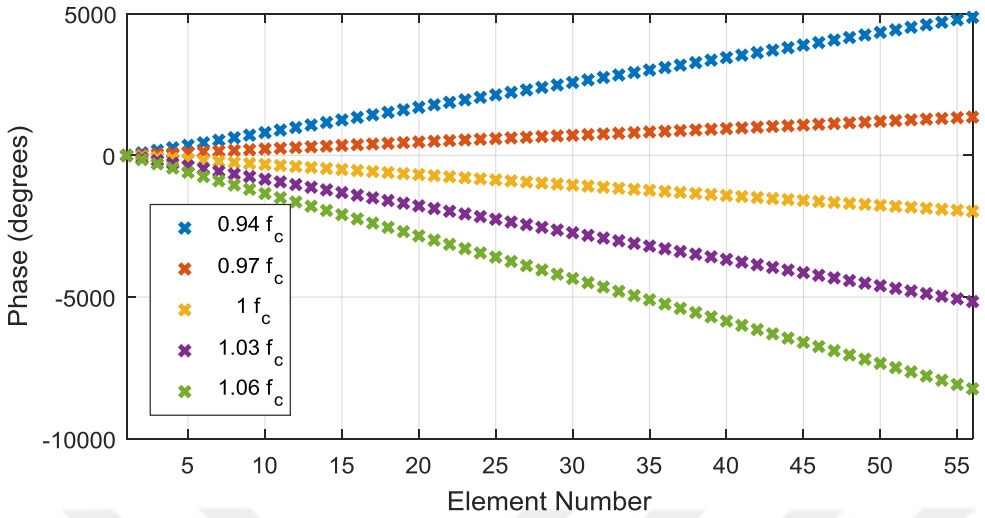

Figure 3.32. Excitation phase.

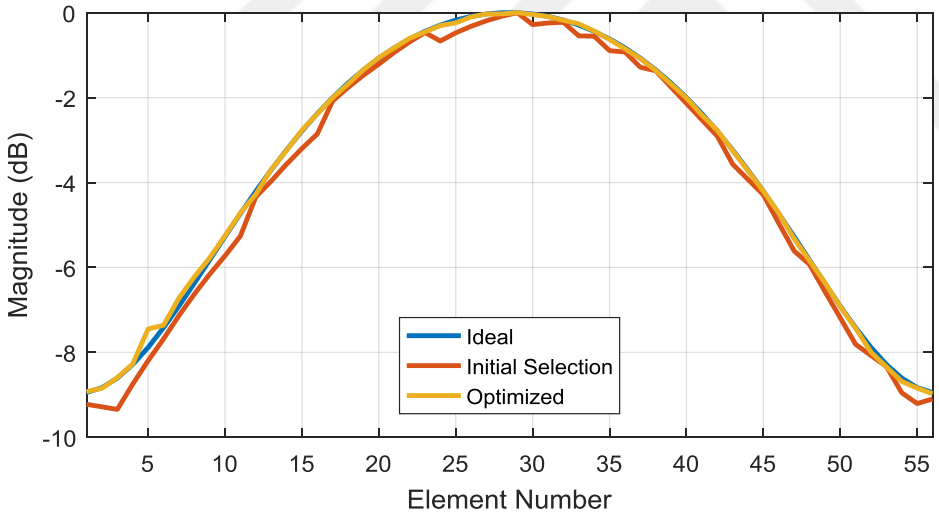

Figure 3.33. Normalized excitation magnitudes at f_c.

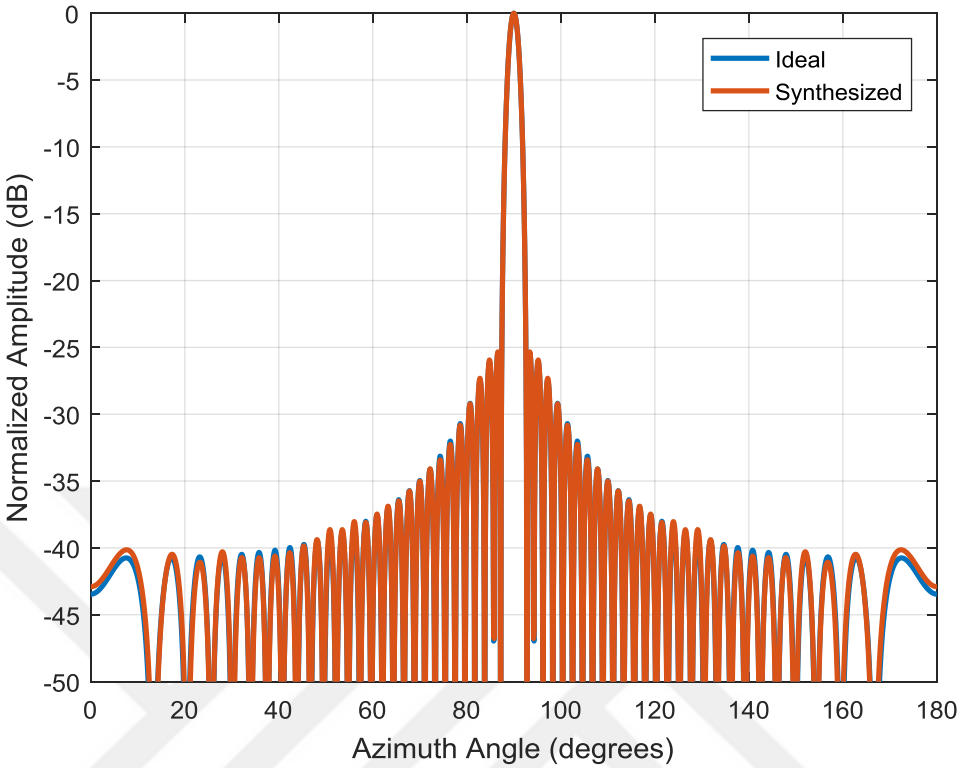

Figure 3.34. Array factor calculated with a uniform phase.

3.1.4.4. Phase Correction

The patterns synthesized with the excitations of the optimized set are given in Figure 3.35, together with the ideal patterns, at five frequencies. It is observed that the scanning performance does not deteriorate significantly but side-lobe levels are increased due to the phase error explained in 3.1.4.1. To eliminate the phase error and suppress side lobes, striplines are extended. The phases of the excitations are plotted in Figure 3.36 with linear fitting at five different frequencies. The differences between the linear-fitting values and the obtained phases are given in Figure 3.37.

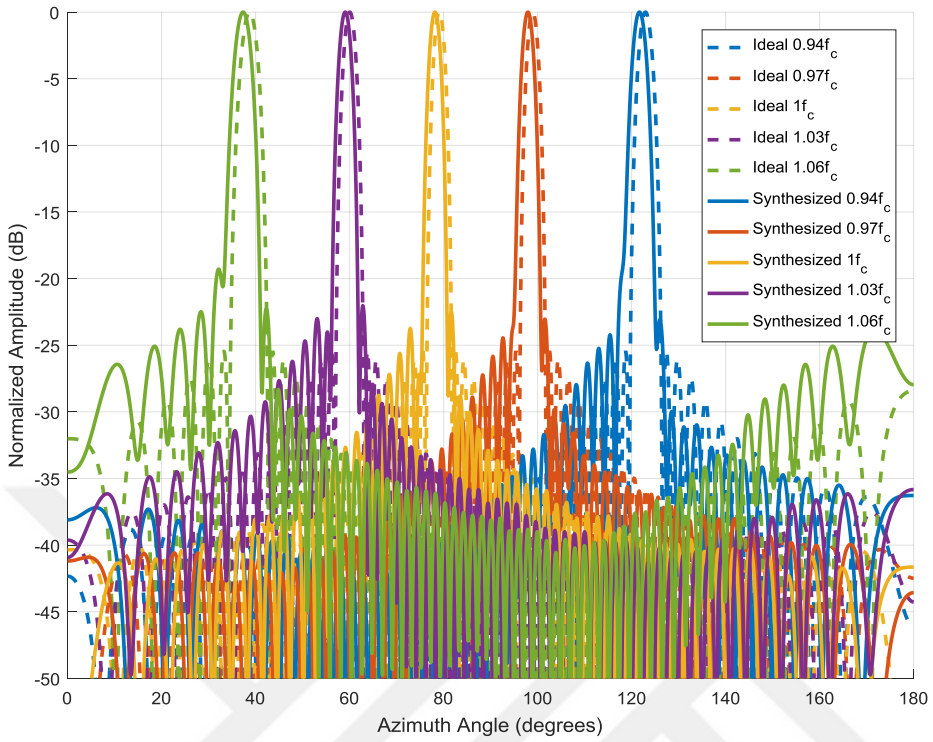

Figure 3.35. Array factor (ideal versus synthesized).

The striplines are extended such that they cover the differences between linear fitting phases and the obtained phases. As mentioned, the extension is done in a meandered fashion to preserve the alignment of the antenna elements as shown in Figure 3.38. Since the guided wavelengths inside and outside the waveguide are different for the stripline, extensions cannot be simply equal to the length difference between the selected insets. The phase introduced by an extension of length $l_{extension}$ can be written as

$$\beta_{extension} = -k_g l_{extension}, \qquad (3.21)$$

where k_g is the wavenumber for the stripline outside the waveguide.

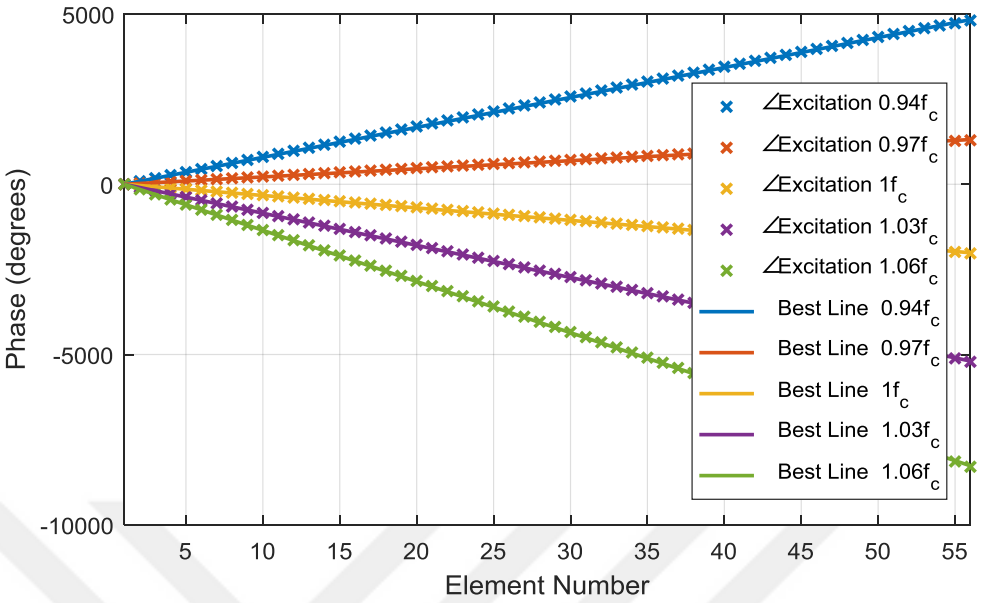

Figure 3.36. The obtained excitation phases and the best fitting lines.

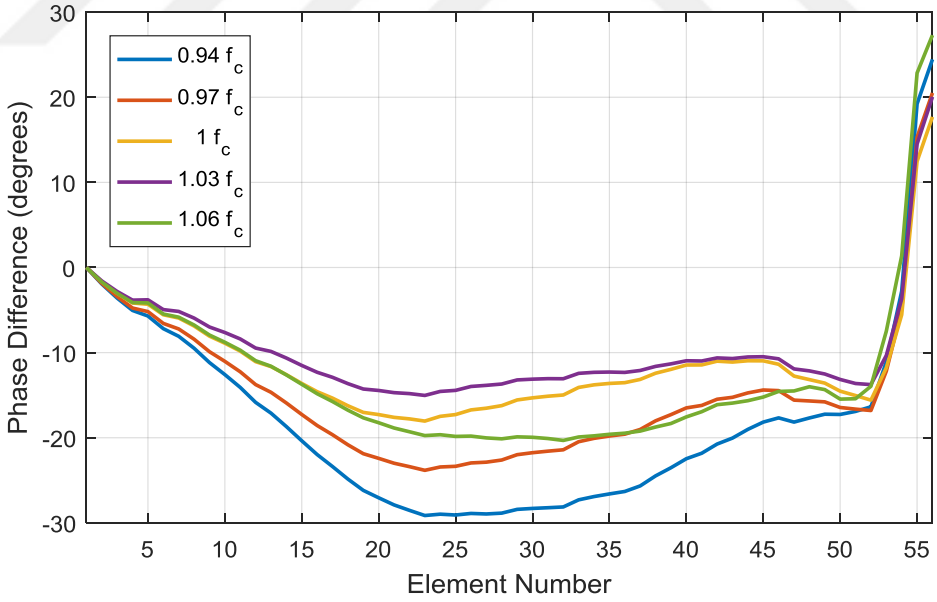

Figure 3.37. Difference between the best fitting lines and the obtained excitation phases.

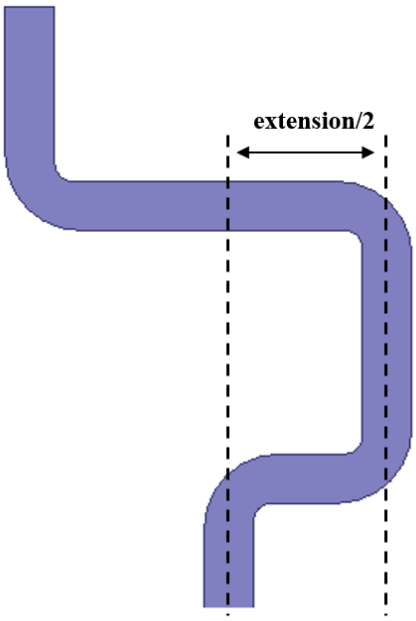

Figure 3.38. Extension of the striplines

The required extensions are obtained with an optimization in order to find an optimal solution for different frequencies. The frequencies included in the optimization are f_{low}, $0.970f_c$, f_c, $1.03f_c$, and f_{high}. Genetic algorithm optimization, which is based on the natural selection theory, is performed with the help of the MATLAB optimization toolbox. Genetic algorithm does not require an initial guess, and bounds are specified as $\pm\lambda_{g_{stripline}}/2$ at f_c. This optimization process is also very fast and an optimal solution is obtained in a few minutes. The synthesized patterns including the extensions for five frequencies are given in Figure 3.39. It can be stated that the errors due to the deviations of the phases from the ideal values are reduced and lower side-lobe levels (below -20.8 dB) are obtained.

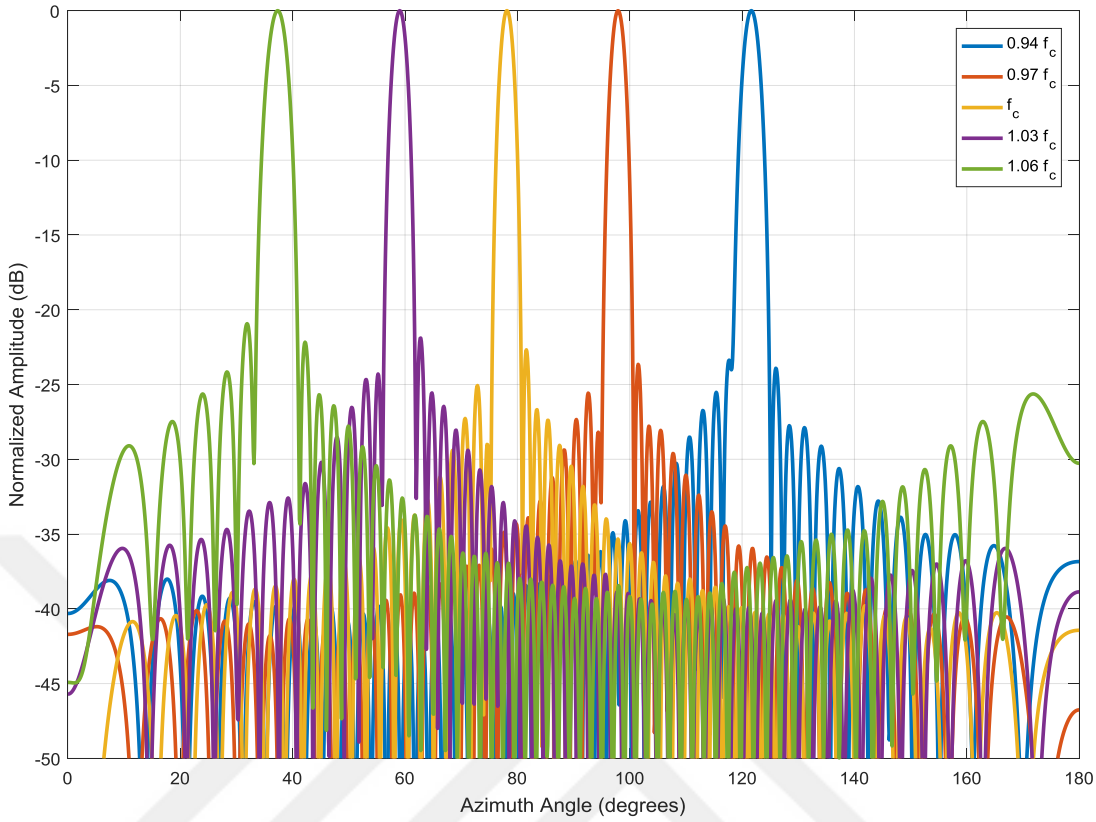

Figure 3.39. Array factor calculated by employing additional phases due to stripline extensions.

3.1.4.5. Final Beamforming Network

By cascading the selected unit cells and extending the line at the coupling port of the coupler, the array is modelled as shown in Figure 3.40 and Figure 3.41, and then simulated. In Figure 3.42, normalized magnitudes of the obtained coupling coefficients at fc are plotted together with the ideal and expected values (see Figure 3.33). At five frequencies, array factors calculated with expected and obtained coupling coefficients are given in Figure 3.43 (see Figure 3.39). Moreover, in Figure 3.44, scanning performance of the beamformer network can be seen at 12 frequencies.

In Figure 3.45 and Figure 3.46, plots for the solution convergence and the required memory are presented respectively. At the end of the 34th adaptive pass in

Ansoft HFSS®, the number of elements becomes 19,828,700, while the required memory reaches 514.74 GB. Since it is a large simulation problem that requires large computational power, it is important to obtain coupling coefficients in the MATLAB environment. As can be seen in Figure 3.42 and Figure 3.43, calculation of coupling coefficients in the MATLAB environment provides accurate results. In Figure 3.47, the array factor of the final beamforming network calculated with the expected coupling coefficients are compared to the array factor calculated with the obtained coupling coefficients for different adaptive passes at the solution frequency (1.06 f_c). It can be seen that the solution converges to the expected result.

Figure 3.40. Final beamformer network.

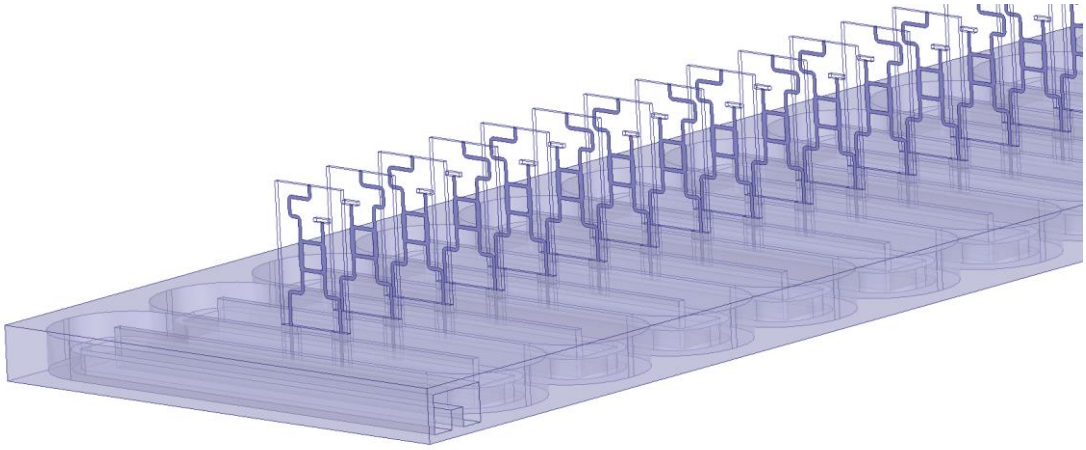

Figure 3.41. Final beamformer network (zoomed view).

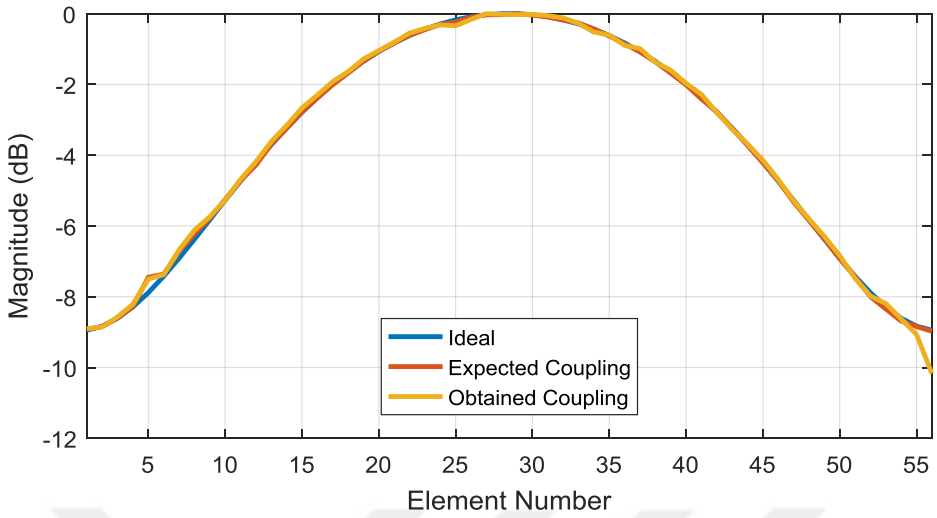

Figure 3.42. Expected and obtained coupling coefficients

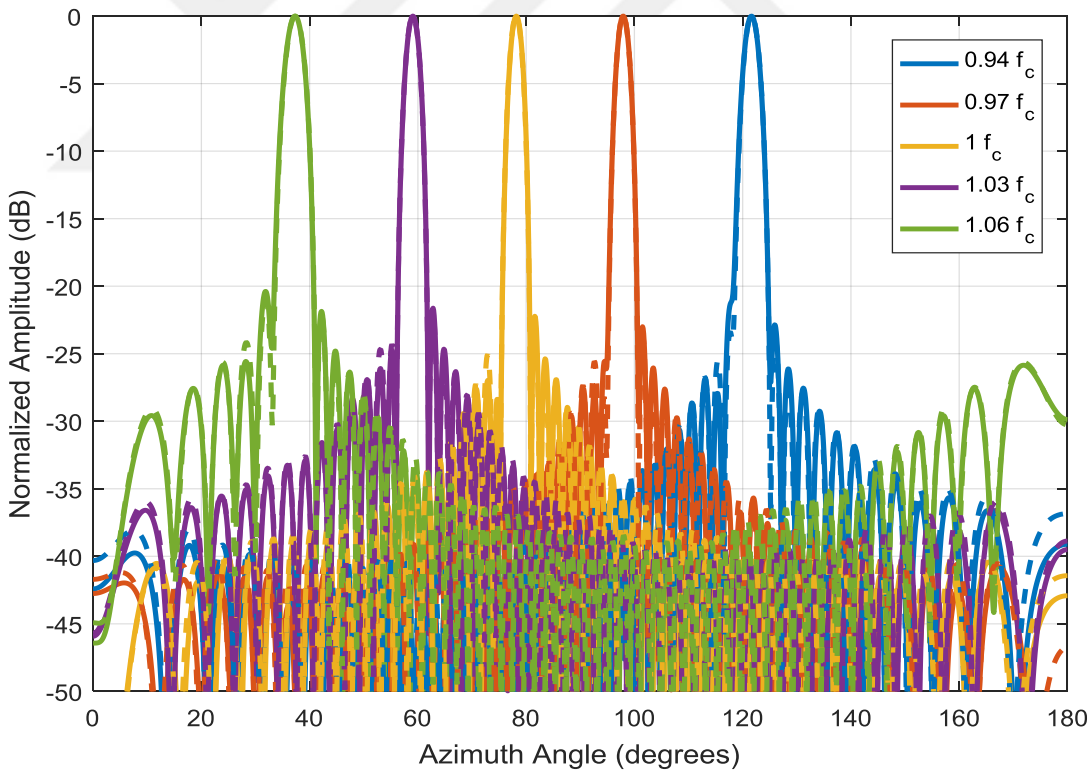

Figure 3.43. Array factor calculated with the expected (dashed line) and the obtained (solid line) coupling coefficients.

The total loss of the waveguide beamformer with respect to frequency is given in Figure 3.48. The return loss and the power absorbed by the load are further presented in Figure 3.49. The increase of losses at f_{bs} is expected due to scan blindness phenomenon, as previously discussed.

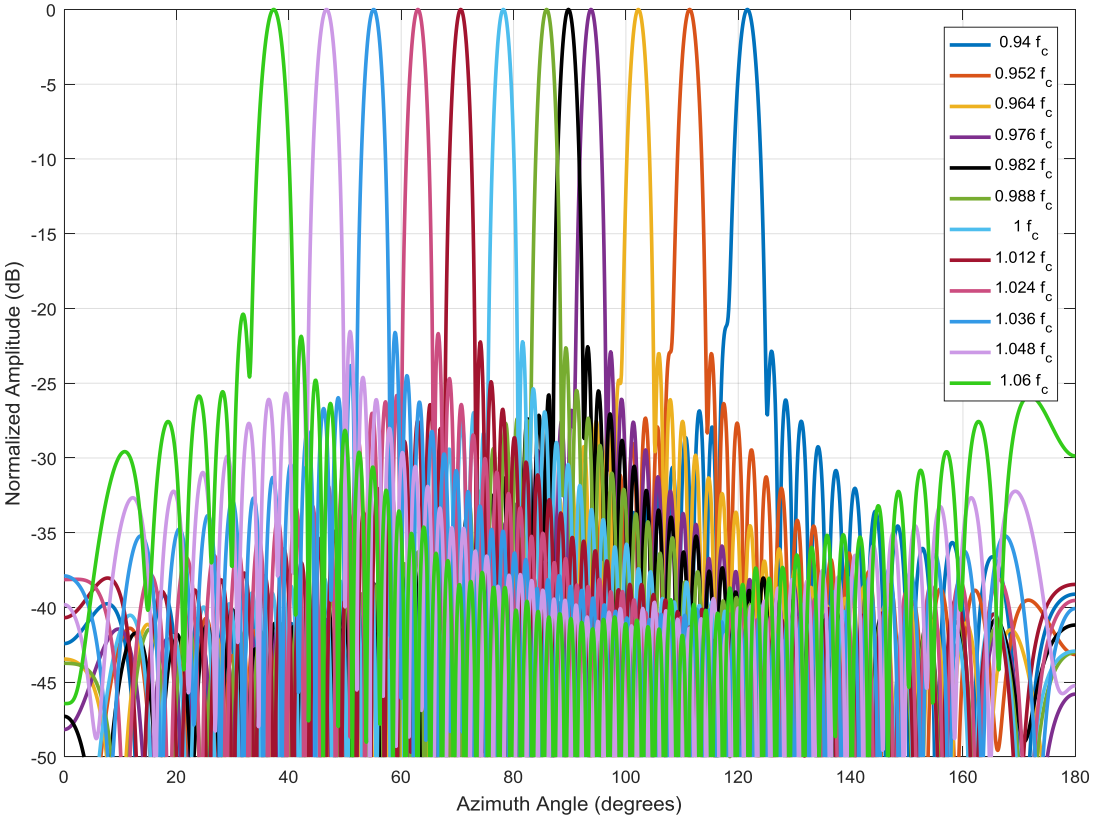

Figure 3.44. Array factor of the final beamforming network.

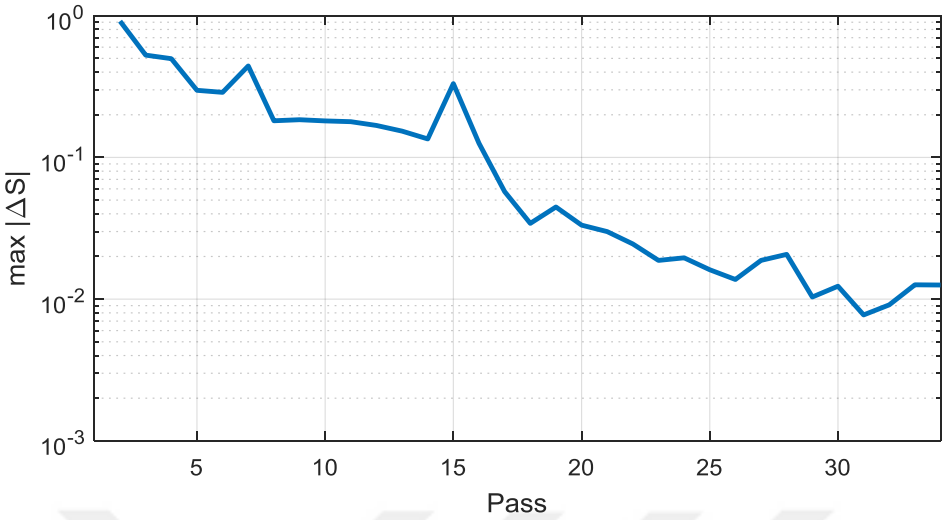

Figure 3.45. Convergence of the solution of the final beamforming network.

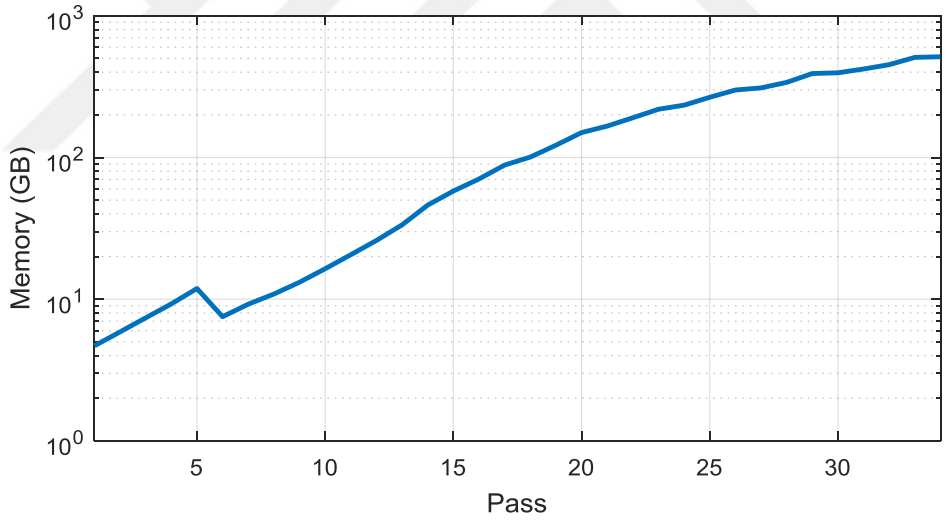

Figure 3.46. Required memory for the simulation of the final beamforming network.

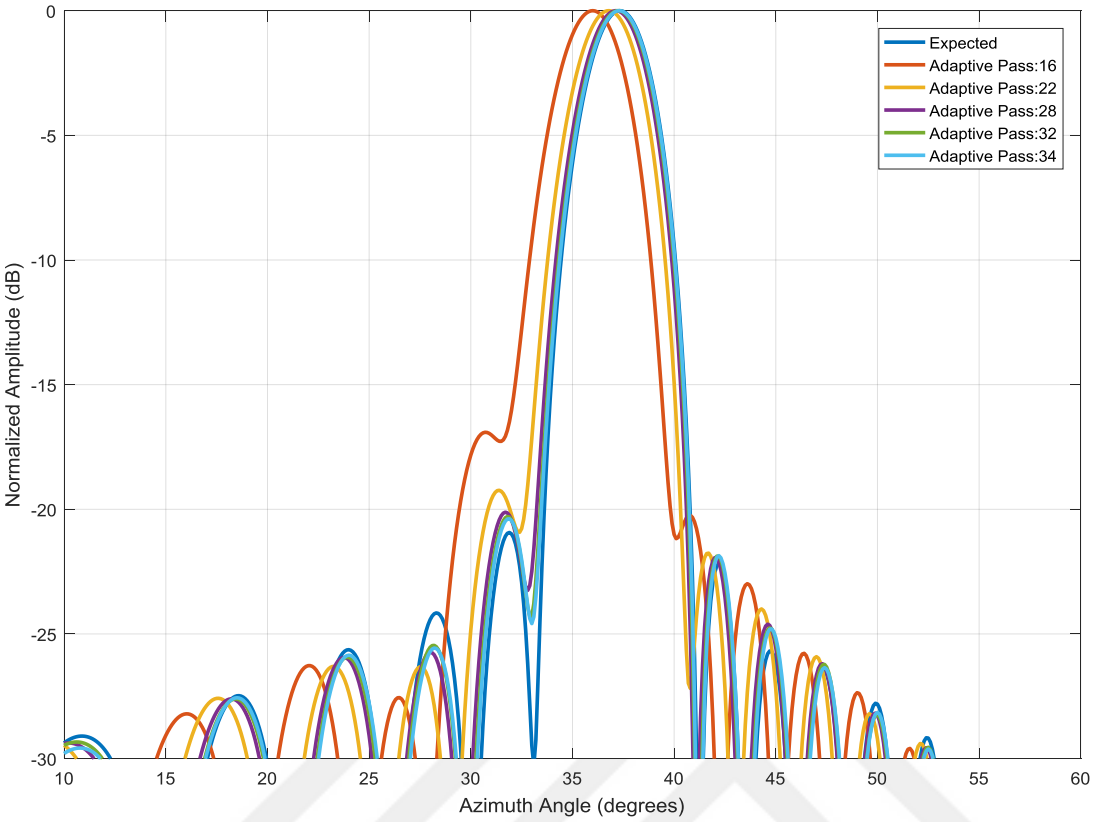

Figure 3.47. Array factor of the final beamforming network calculated with the obtained coupling coefficients for different adaptive passes and with the expected coupling coefficients at 1.06 f_c.

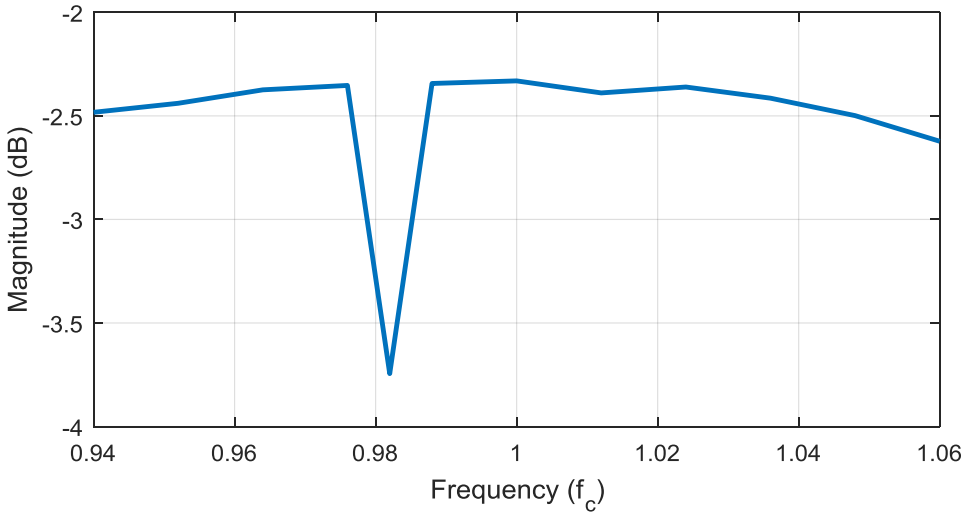

Figure 3.48. Loss of the final beamforming network.

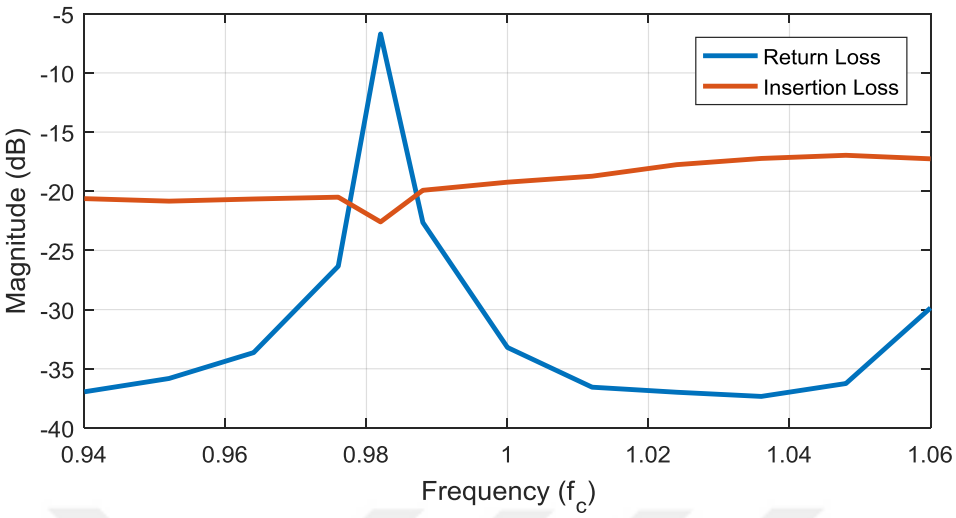

Figure 3.49. Return loss and insertion loss of the beamforming network.

3.2. Generation of Elevation Pattern

As mentioned previously, Vivaldi antennas that form an important class of TSAs are used to generate the array in this study. The properties of TSAs are given in Section 2.4 and the motivation to use Vivaldi antennas as radiating elements is mentioned in Section 1.2. In the following, the full-wave simulations are performed by using Ansoft HFSS®, where the metallizations are modeled as copper.

3.2.1. Pattern Synthesis in the Elevation Axis

As given in Table 1.1, the antenna needs to have 9° half-power beamwidth at broadside. It is worth to mention that obtaining elevation patterns at the conical cuts results in broadening of the beam as the beam deviates from broadside. Thus, half-power beam is specified in broadside direction. Since side-lobe level is not specified, uniform excitation can be realized in the elevation axis.

From array-factor calculation, eight array elements with uniform excitation and antenna spacing of $0.715\lambda_c$ lead to radiation patterns with no grating lobes over

the frequency band of operation (f_{low}-f_{high}) and 9° beamwidth at f_{bs}. The normalized array factors for five samples in the frequency band are shown in Figure 3.50.

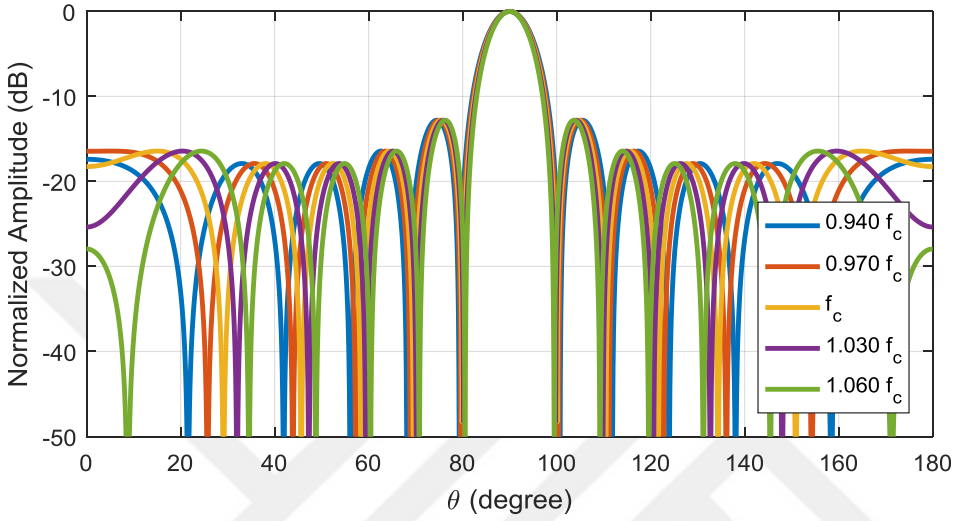

Figure 3.50. Normalized array factor for the elevation pattern.

3.2.2. Stripline-to-Slotline Transition

The material selected and the geometry designed for stripline probes in Section 3.1.3.1 are also used in the design of the antenna. The first step of the process is to design the feeding section of a Vivaldi structure. The antenna is fed by a stripline-to-slotline transition, and the transition is realized by the model shown in Figure 3.51. Two identical transitions are cascaded, while the return and insertion losses of the model are examined for various lengths of the slotline and stripline stubs, i.e., L_{sl} and L_{st}. For the parameter values given in Table 3.4, return loss values lower than −17dB are obtained over the frequency band of operation, as shown in Figure 3.52. The obtained insertion loss values are depicted in Figure 3.53.

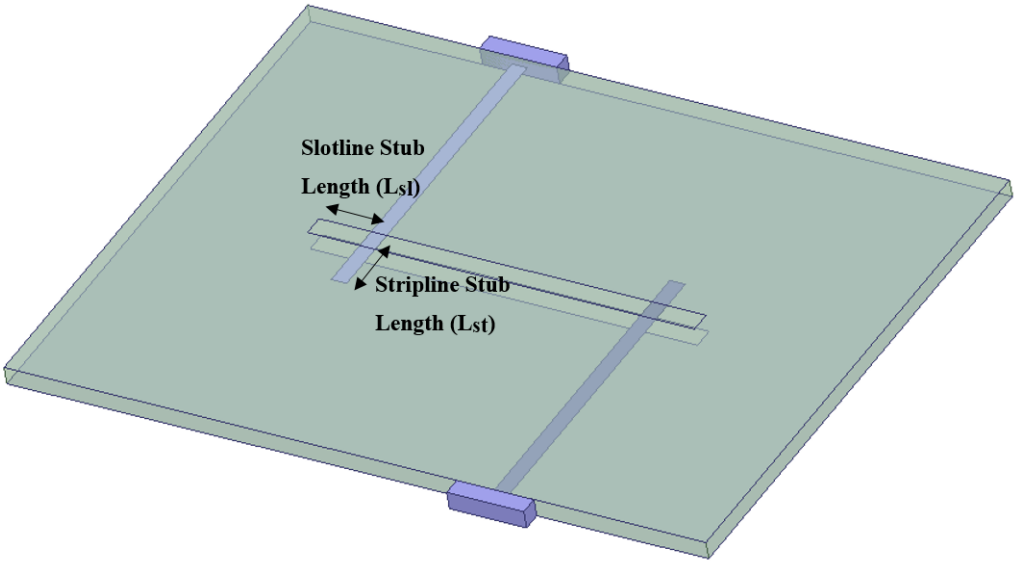

Figure 3.51. Stripline-to-slotline transition.

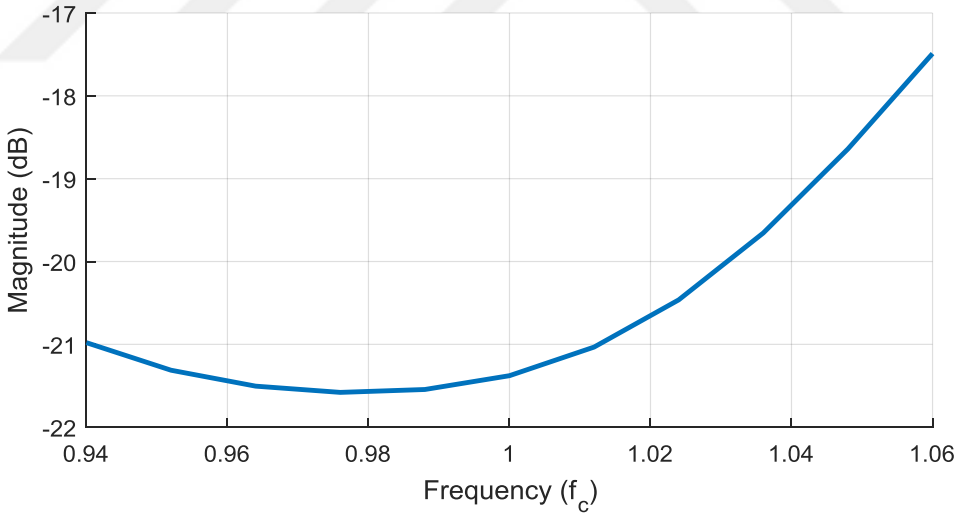

Figure 3.52. Return loss of the stripline-to-slotline transition in Figure 3.51.

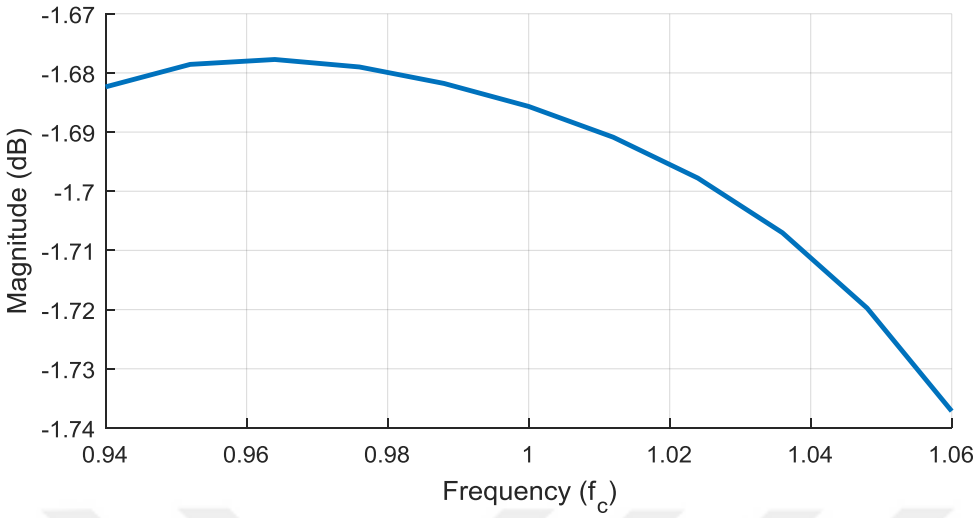

Figure 3.53. Insertion loss of the stripline-to-slotline transition in Figure 3.51.

Table 3.4. Design parameters of the stripline-to-slotline transition.

Design Parameter	**Value (in terms of λ_c)**
Slotline Stub Length (L_{sl})	0.0834
Stripline Stub Length (L_{st})	0.0787

3.2.3. Vivaldi Element Design

The designed antenna model is shown in Figure 3.54 with the related design parameters. Another parameter that is not shown in Figure 3.54 but related to the design is the taper rate R. The exponential opening of the antenna is defined with the taper rate and the endpoints of the taper, i.e., $P_1(x_1, y_1)$ and $P_2(x_2, y_2)$, as

$$x = c_1 e^{Ry} + c_2 \qquad (3.22)$$

$$c_1 = \frac{x_1 - x_2}{e^{Ry_1} - e^{Ry_2}} \tag{3.23}$$

$$c_2 = x_1 - c_1 e^{Ry_1}. \tag{3.24}$$

The parameters feed distance (f_d), taper extension (t_e), and substrate extension (s_e) are determined and given in Table 3.5. Since antenna spacing, as well as slotline and stripline stub lengths are already determined previously, the parameters to be selected are taper length (L), aperture width (W), slotline width (W_{sl}), uniform slotline length (L_u) , backwall offset (L_b) and taper rate (R). To determine the optimal parameters that result in low return loss, the optimization setup of the Ansoft HFSS® software is used.

Table 3.5. Determined design parameters.

Design Parameter	**Value (in terms of λ_c)**
Feed Distance (f_d)	0.1722
Taper Extension (t_e)	0.0275
Substrate Extension (s_e)	0.0275

For the overall design, mutual coupling effects in both E- and H-planes should be considered. Mutual coupling effects are involved in the design process by using the infinite array approach. This approach treats the given structure, which is named as unit cell, as if there are infinitely many identical copies with the same excitation coefficient amplitudes connected to each other. In the Ansoft HFSS® software, the infinite array approach is applied by assigning boundaries to the walls of the unit cell.

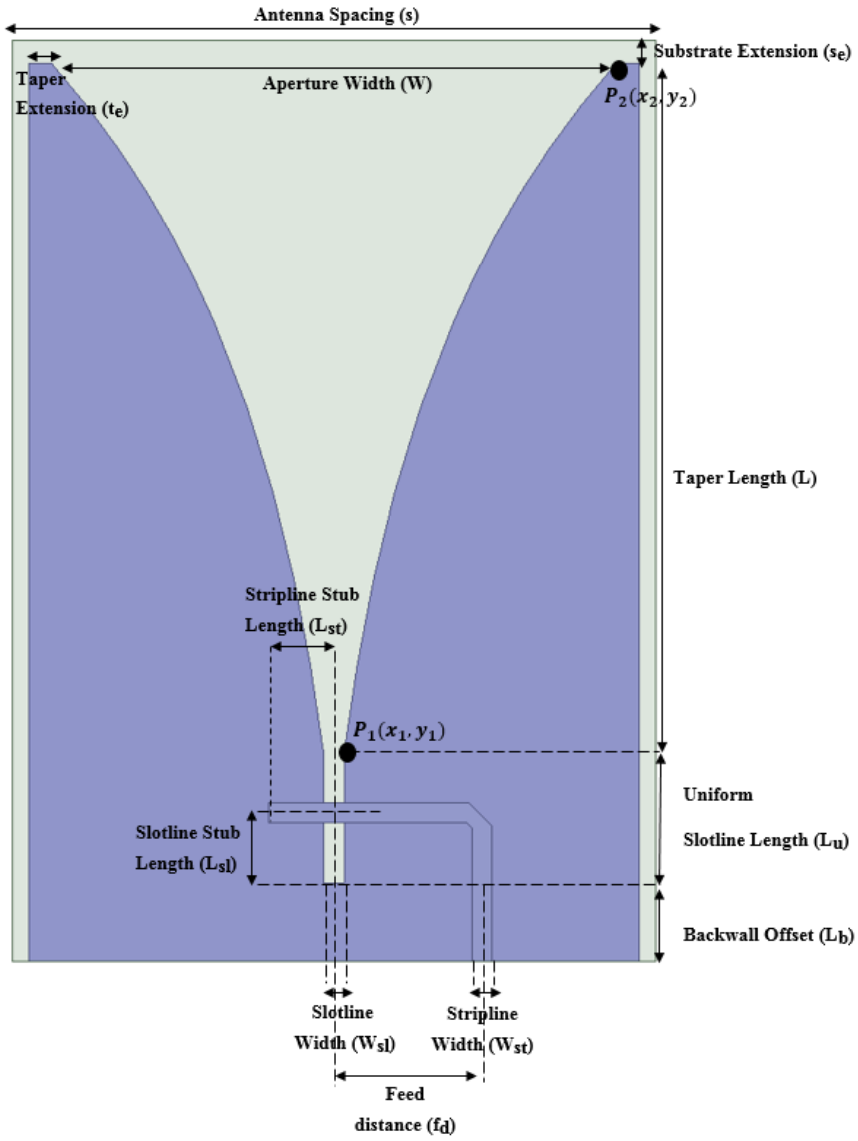

Figure 3.54. Vivaldi antenna and parameters.

One of the boundaries is assigned as “Master Boundary” and other one is assigned as “Slave Boundary”. The master and slave boundaries are exactly matched except for a possible phase difference. In the Vivaldi antenna design, on the surfaces of the rectangular vacuum in which the antenna is placed, master and slave boundaries are defined in both E- and H- planes. The surface in front of the antenna is defined as the radiation boundary, while the back surface is assumed to be perfect electric conductor

For the E-plane, defined master and slave boundaries are shown in Figure 3.55. Since there is not scanning on the elevation axis, there are not any phase differences across these boundaries.

For the H-plane, defined master and slave boundaries are shown in Figure 3.56. Due to scanning on the azimuth axis, a phase difference should be introduced between the master and slave boundaries. Since the scanning, and hence, the phase delay between two consecutive units are determined by the frequency, the phase delay between the two boundaries should also be frequency-dependent. Progressive phase for 21 frequencies for the elementary meandered waveguide section (see Table 3.2) is formulated by a 3rd degree polynomial as

$$Phase\ Delay = -0.8673f^3 + 48.4423f^2 - 1008.55f + 7314.30, \quad (3.25)$$

which is used in the simulations to present the phase difference between the master and slave boundaries in the H-plane where f is in GHz. The phase delay values which are listed in Table 3.2 and the formulated phase delay values are examined in Figure 3.57.

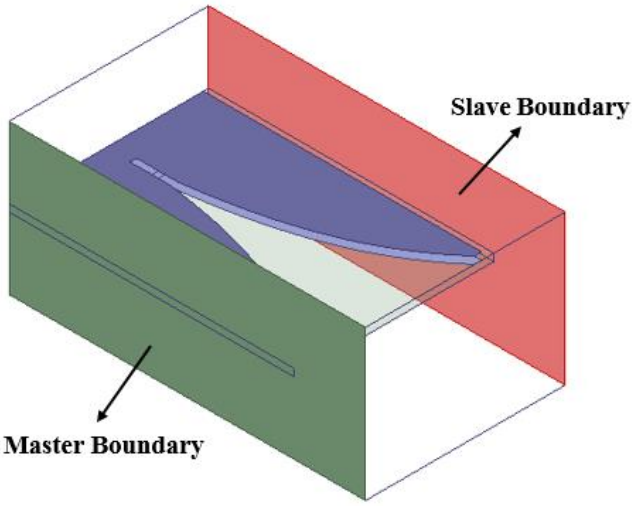

Figure 3.55. Boundaries on the E-plane.

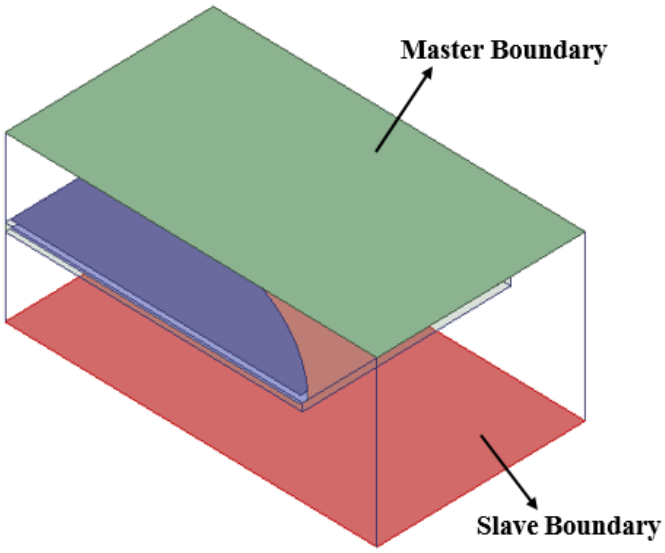

Figure 3.56. Boundaries on the H-plane.

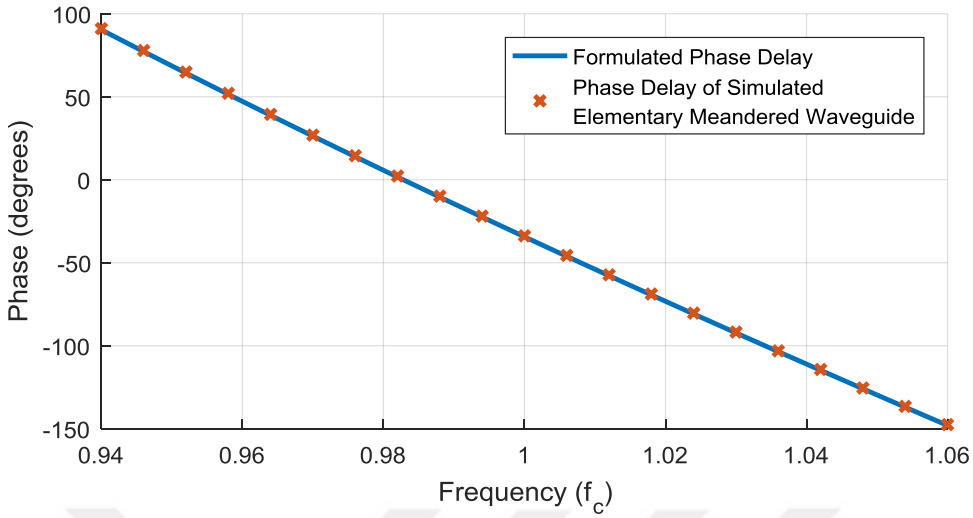

Figure 3.57. Phase delay.

Table 3.6. Design parameters of the Vivaldi antenna element.

Design Parameter	**Value (in terms of λ_c)**
Antenna Spacing (s)	0.7155
Stripline Width (W_{st})	0.0242
Slotline Stub Length (L_{sl})	0.0834
Stripline Stub Length (L_{st})	0.0787
Feed Distance (f_d)	0.1722
Taper Extension (t_e)	0.0275
Substrate Extension (s_e)	0.0275
Taper Length (L)	0.5043
Aperture Width (W)	0.6434
Slotline Width (W_{sl})	0.0511
Uniform Slotline Length (L_u)	0.2979
Backwall Offset (L_b)	0.1190
Taper Rate (R)	462.4

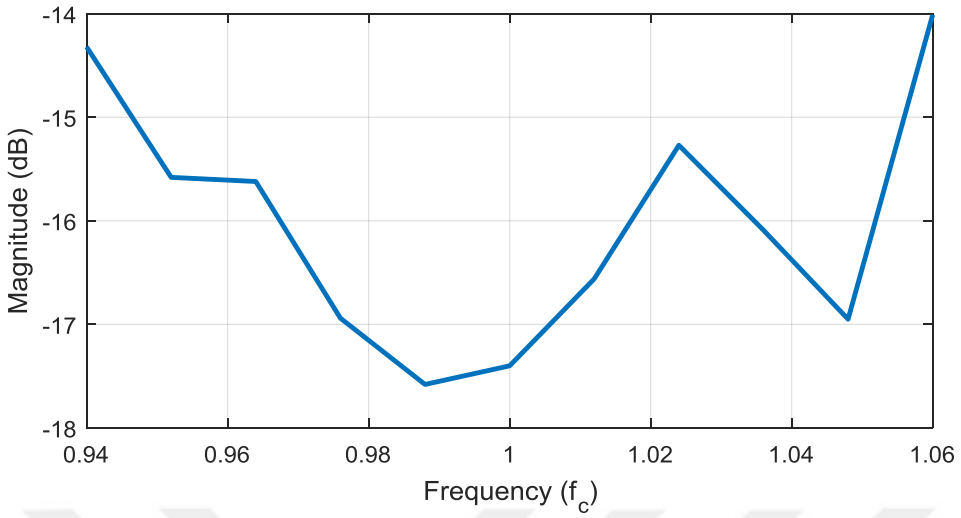

Figure 3.58. Return loss of the Vivaldi antenna element.

The optimization is performed to obtain return loss values less than −12 dB in the frequency band of operation sampled at five points. By means of the optimization, the antenna parameters are determined as listed in Table 3.6. The return loss of the Vivaldi element over the frequency band of operation is given in Figure 3.58.

3.2.4. 8x1 Vivaldi Array Design

Eight Vivaldi elements (designed in the previous section) are placed along a straight line with s = $0.715\lambda_c$ spacing as shown in Figure 3.59. Considering periodic boundaries, phase delays are applied on the H-plane boundaries, as applied to the single antenna. The active return loss of each element is given in Figure 3.60 in the case of uniform excitation. The total loss of the 8x1 Vivaldi array is given in Figure 3.61.

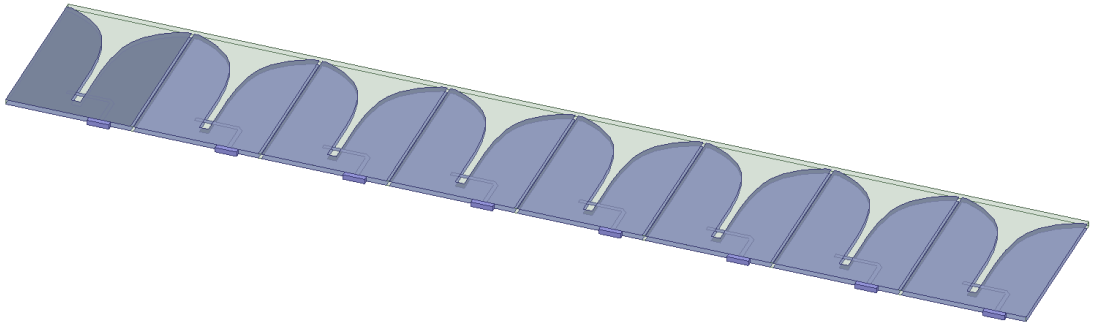

Figure 3.59. 8x1 Vivaldi array.

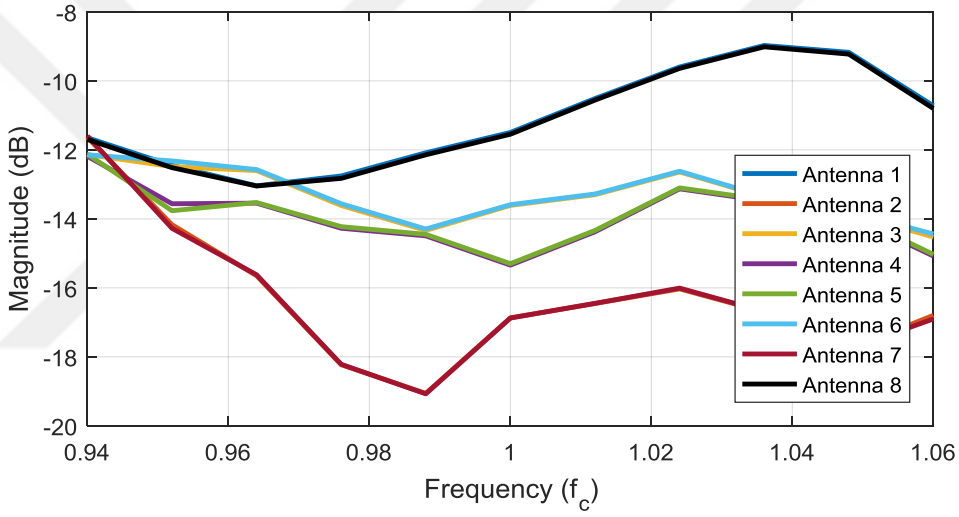

Figure 3.60. Active return loss values for the 8x1 Vivaldi array in Figure 3.59.

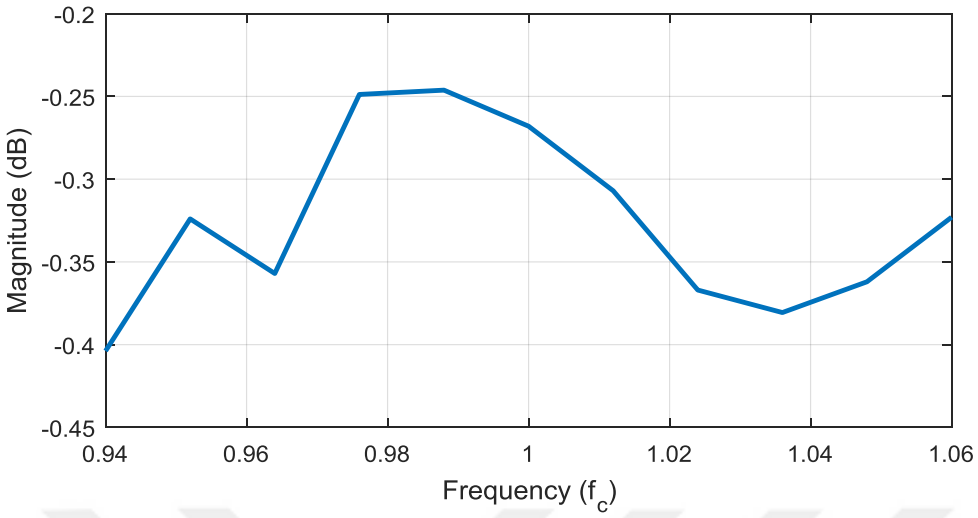

Figure 3.61. Loss of the 8x1 Vivaldi array in Figure 3.59

Arrays that operate over a narrow frequency band can be excited with a power divider, as illustrated in Figure 3.62 for an array of eight elements. In a narrow frequency band, such a this structure can provide an equal phase distribution among the antennas. The power divider in Figure 3.62 is designed such that it creates an equal phase distribution at f_c to synthesize the required beam at the elevation. This design is simulated at five different frequencies (f_{low}, $0.970f_c$, f_c, $1.03f_c$, and f_{high}). Excitation phases at different ports are given in Figure 3.63, while normalized array factors synthesized with those excitations are given in Figure 3.64. It can be stated that, in this design that has 12% frequency bandwidth, this kind of a power divider cannot provide equal phases for antenna excitations and it leads to pattern deterioration.

To realize the desired uniform excitation, an 8-way equal power divider that consists of seven stripline Wilkinson power dividers is designed. The Wilkinson power divider is a 3-port network that is matched at all ports by dissipating the reflected power from the output ports by a resistor [41]. An illustration for a Wilkinson power divider with an equivalent transmission line circuit is shown in Figure 3.65.

Since the antenna and the probes are matched to 50Ω, the power divider is also designed for a characteristic impedance of Z_0 = 50Ω. Quarter-wave lines have the impedance of $Z_0\sqrt{2}$ = 70.71Ω and width 0.013λ_c, while the value of the resistor is 100Ω.

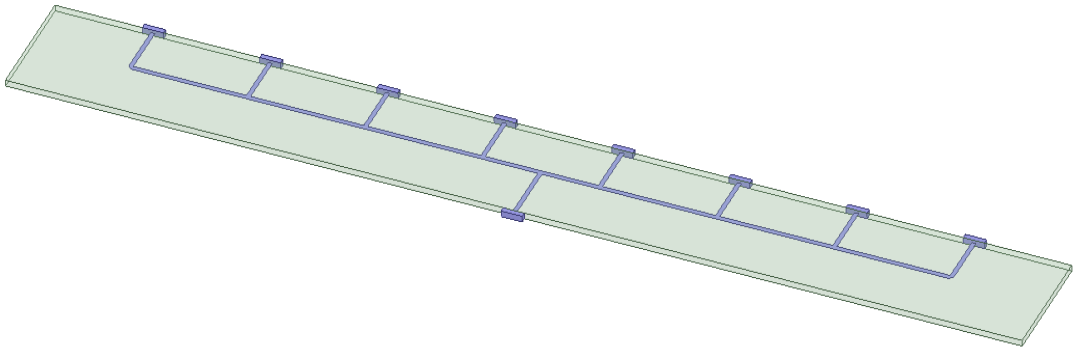

Figure 3.62. Power divider.

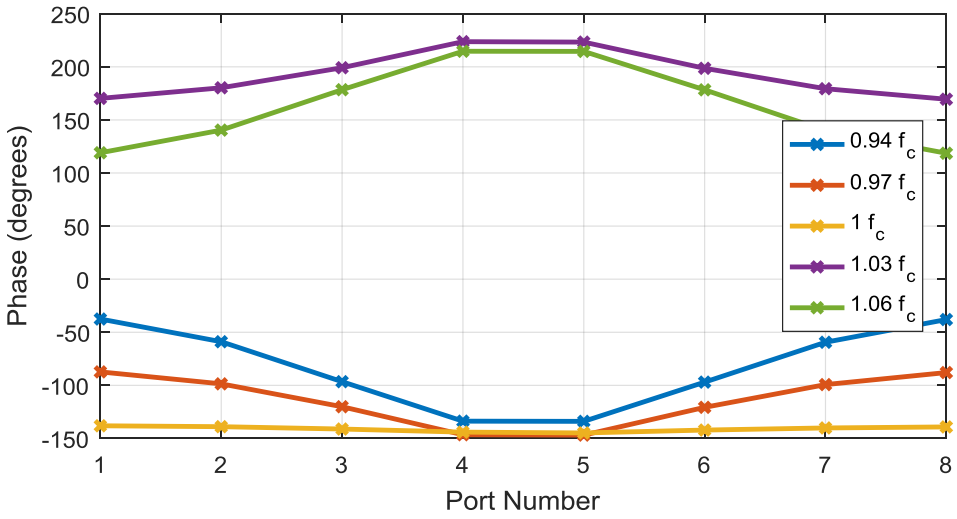

Figure 3.63. Excitation phases.

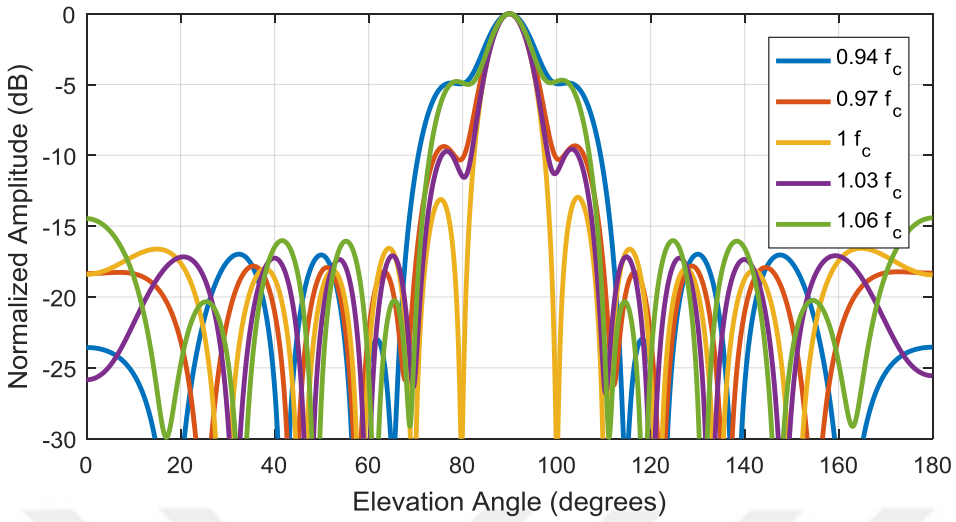

Figure 3.64. Calculated array factor.

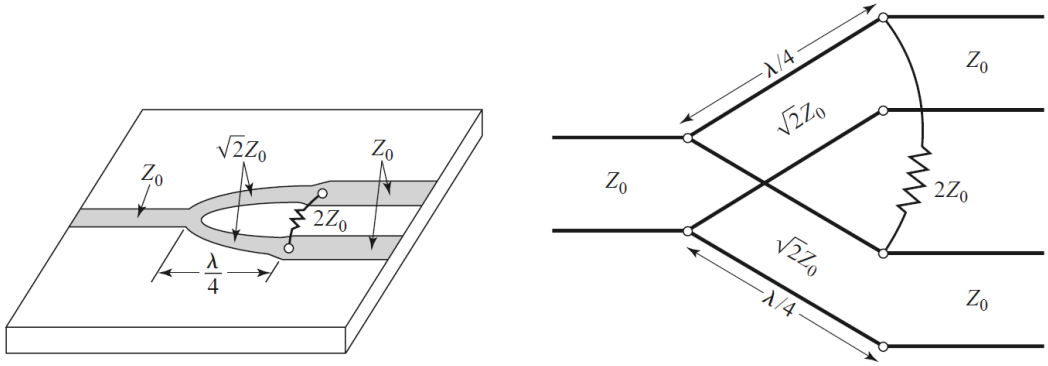

Figure 3.65. Wilkinson power divider and equivalent transmission line circuit. Reprinted from "Microwave engineering" by Pozar, D. M., 2011, John Wiley & Sons. © 2011 John Wiley & Sons.

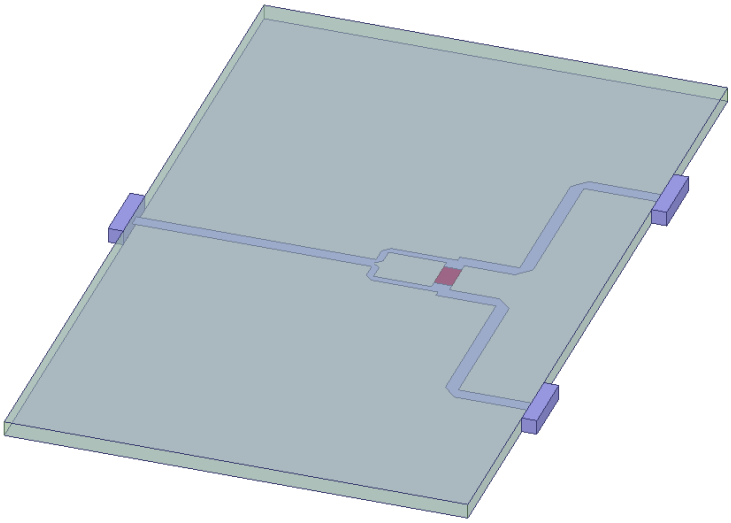

Figure 3.66. The Wilkinson power divider before input matching.

First, a Wilkinson power divider with two output ports shown in Figure 3.66 is designed. However, due to reflections at the transitions, a mismatch at the input port is observed. This mismatch can be seen in the Smith Chart in Figure 3.67, which shows the network parameter S_{11}. To match the divider at the input port, a quarter-line transformer is introduced. Specifically, a quarter-line transformer with characteristic impedance $Z_{transformer} = \sqrt{Z_0 Z_{in}}$ (where Z_0 = 50Ω) is inserted at a location such that the impedance seen from the power divider is real and equal to Z_{in}. The matched 2-way power divider is shown in Figure 3.68, whereas the obtained S_{11} is given in Figure 3.69.

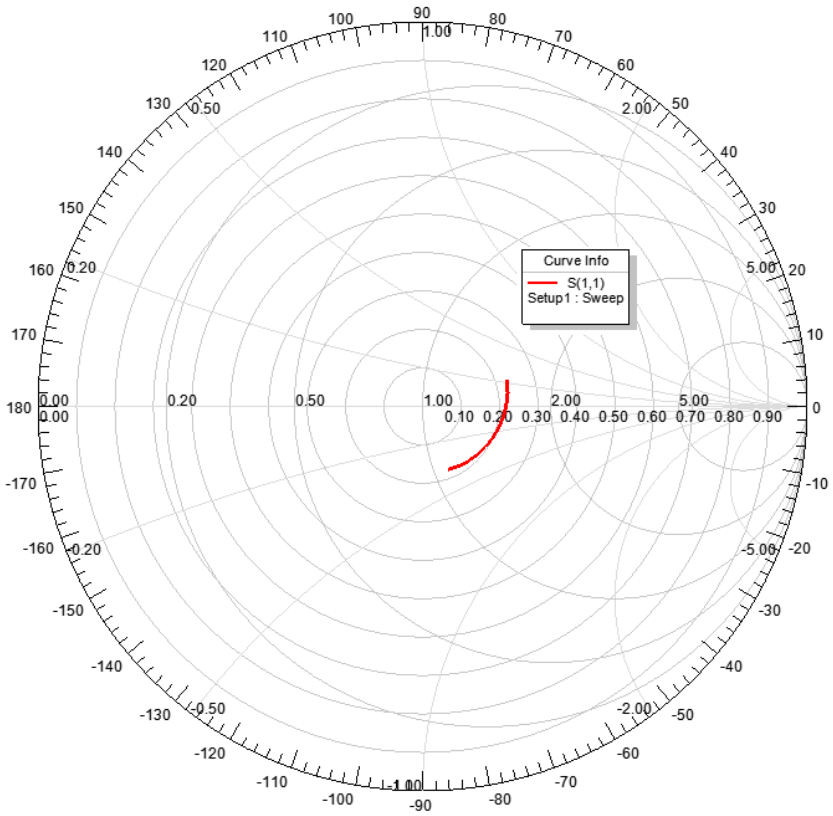

Figure 3.67. Smith Chart for the Wilkinson power divider before input matching.

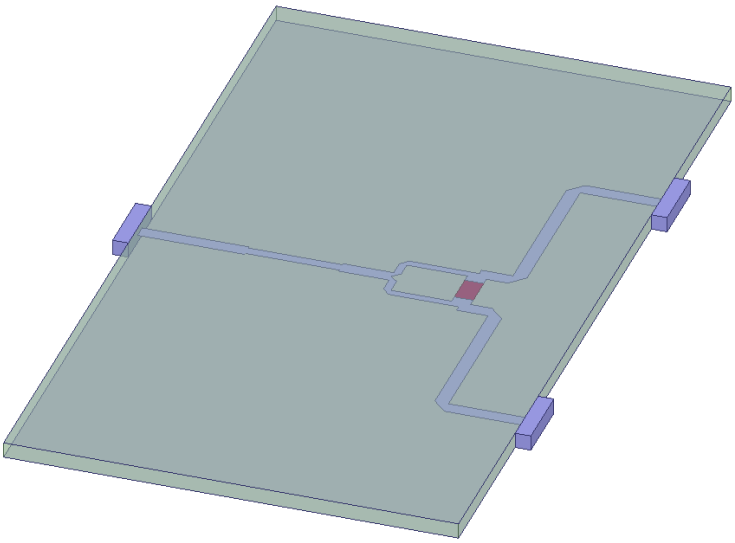

Figure 3.68. The Wilkinson power divider after the input matching.

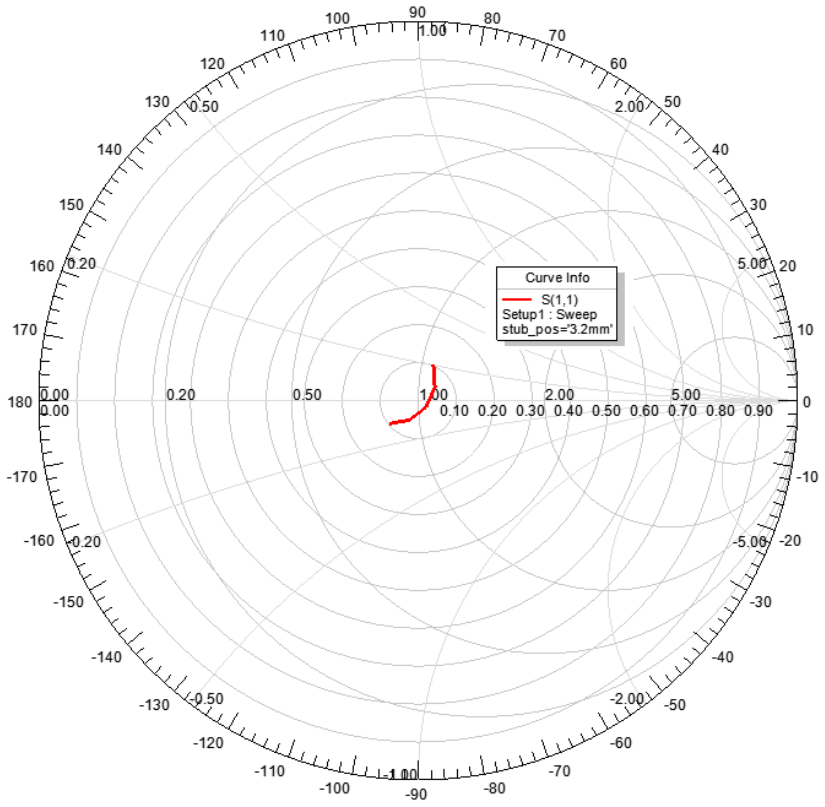

Figure 3.69. Smith Chart for the Wilkinson power divider after input matching.

Three of the designed 2-way power dividers are placed together in order to have a 4-way power divider, as shown in Figure 3.70. The 4-way power divider is matched at the input port with a procedure as in the 2-way power divider. Connecting two 4-way power dividers via a 2-way power divider, and tuning the position and width of the quarter-wave transformer at the input port to obtain the best matching, the 8-way power divider shown in Figure 3.71 is obtained. The corresponding Smith chart result for S_{11} is given in Figure 3.72. Return losses of all ports of the 8-way power divider are plotted in Figure 3.73, while the insertion loss plots are given in Figure 3.74. In Figure 3.75, total loss of the power divider is plotted.

The designed power divider is connected to the array shown in Figure 3.59 and the overall structure in Figure 3.76 is obtained. Applying periodic boundaries in the H-plane, the array is simulated. The normalized elevation pattern at the broadside is plotted in Figure 3.77, while the return loss at the input port and the total loss of the structure are given in Figure 3.78 and Figure 3.79, respectively.

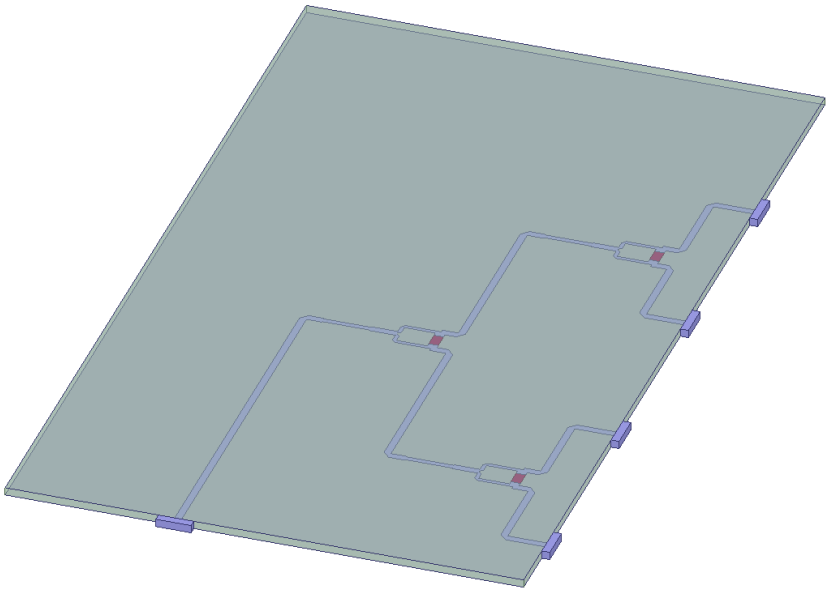

Figure 3.70. 4-way power divider before input matching.

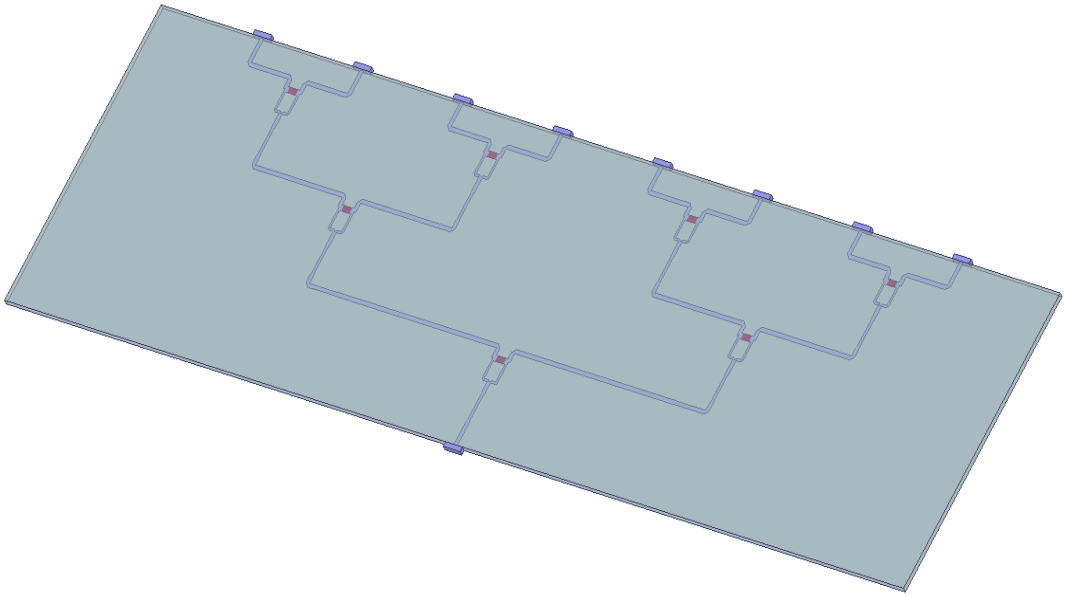

Figure 3.71. The 8-way power divider.

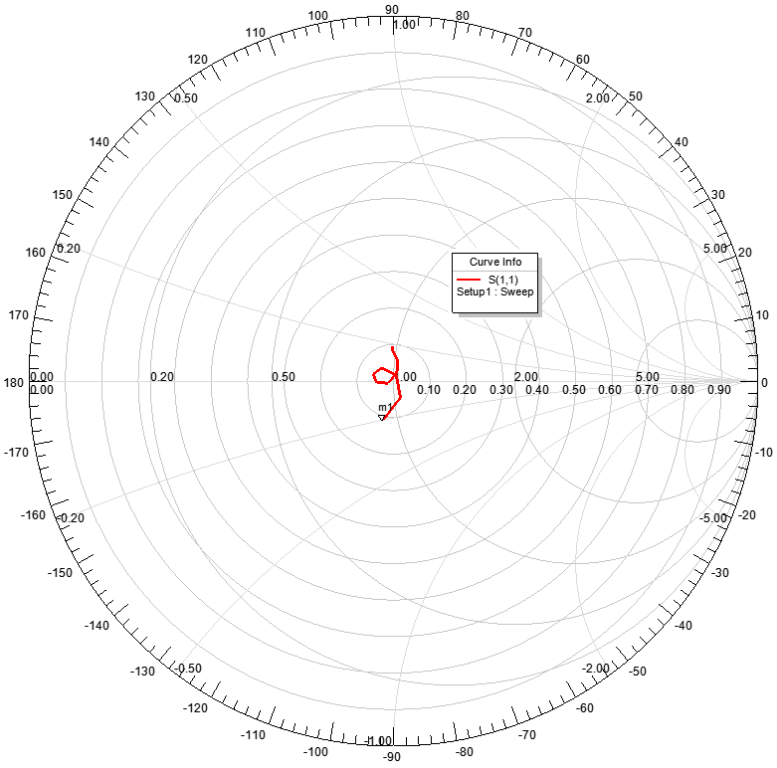

Figure 3.72. Smith Chart for the 8-way power divider in Figure 3.71.

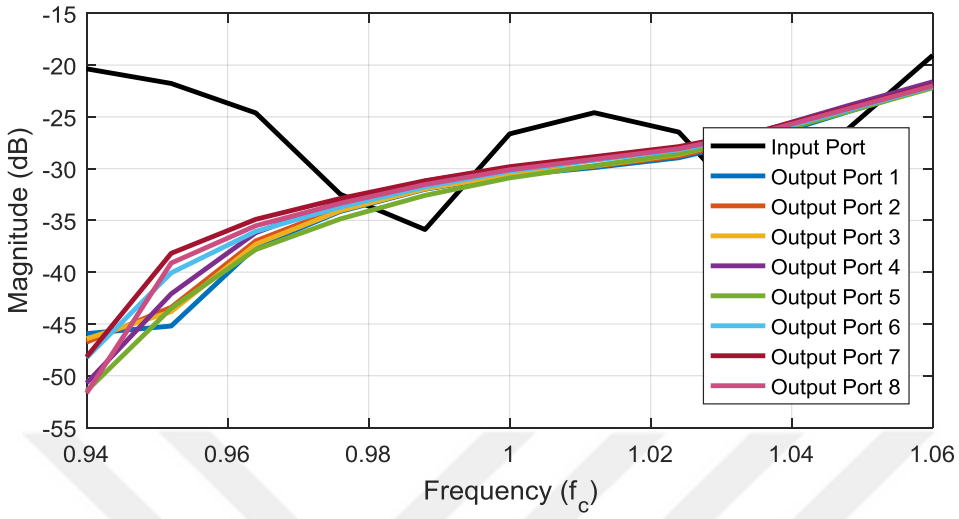

Figure 3.73. Return loss values for the 8-way power divider.

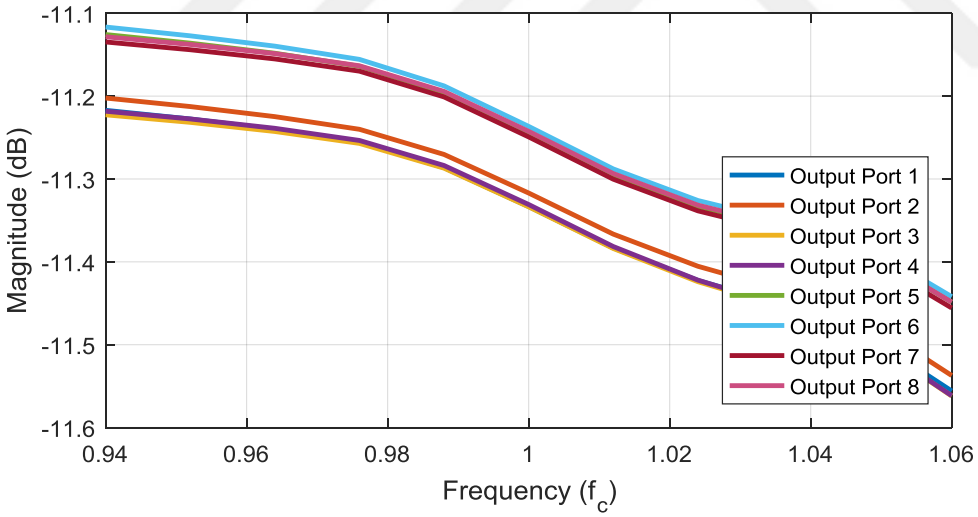

Figure 3.74. Insertion loss values for the 8-way power divider.

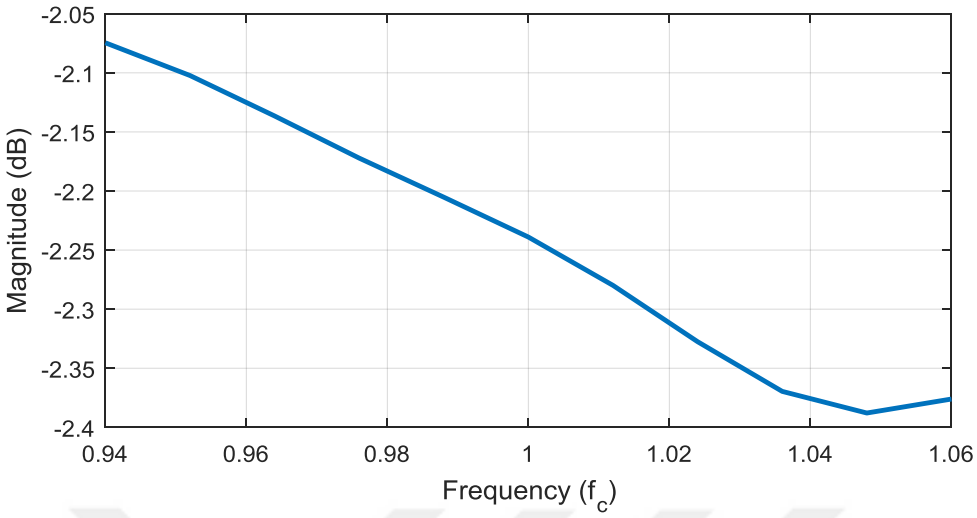

Figure 3.75. Loss of the power divider.

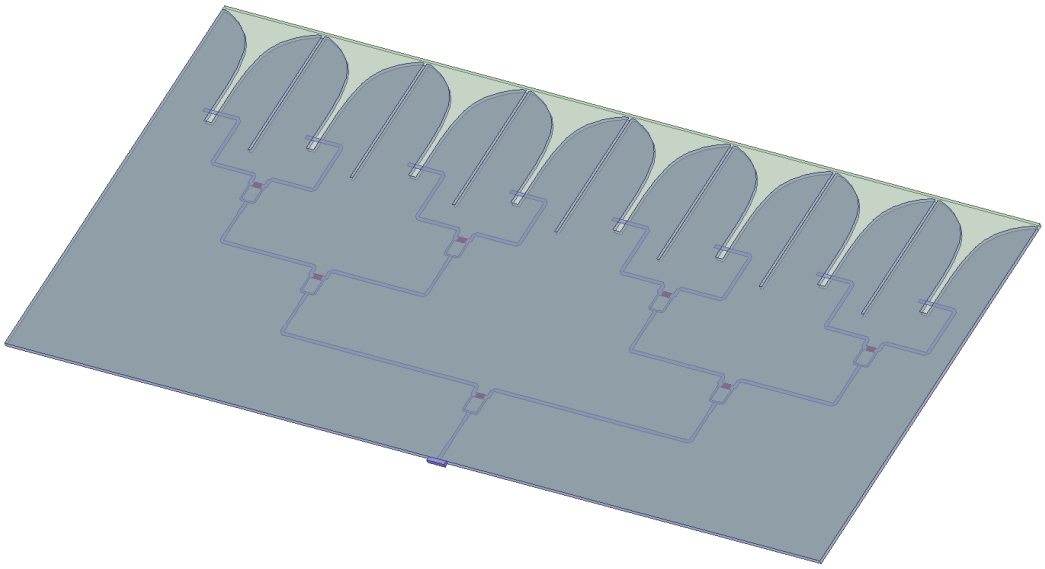

Figure 3.76. 8x1 Vivaldi array combined with the designed power divider network.

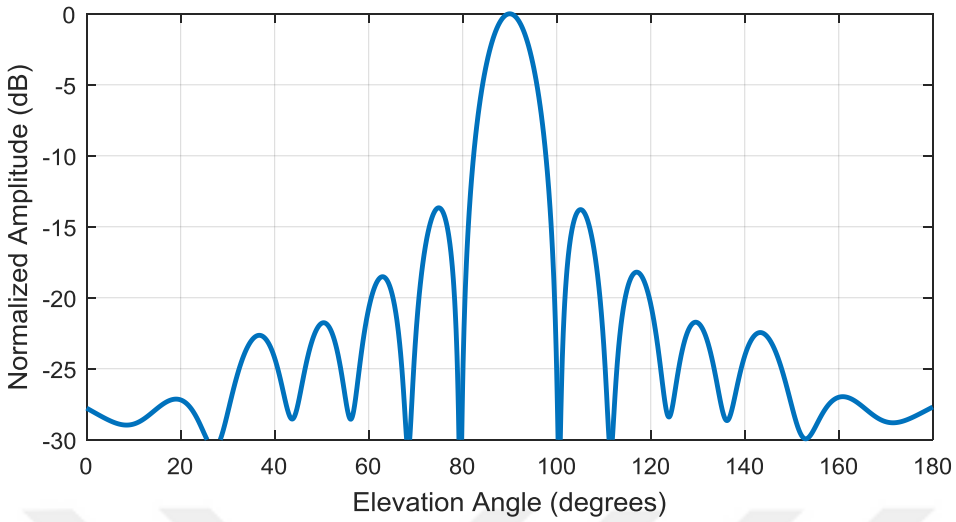

Figure 3.77. Elevation pattern of the 8x1 Vivaldi array with the power divider network.

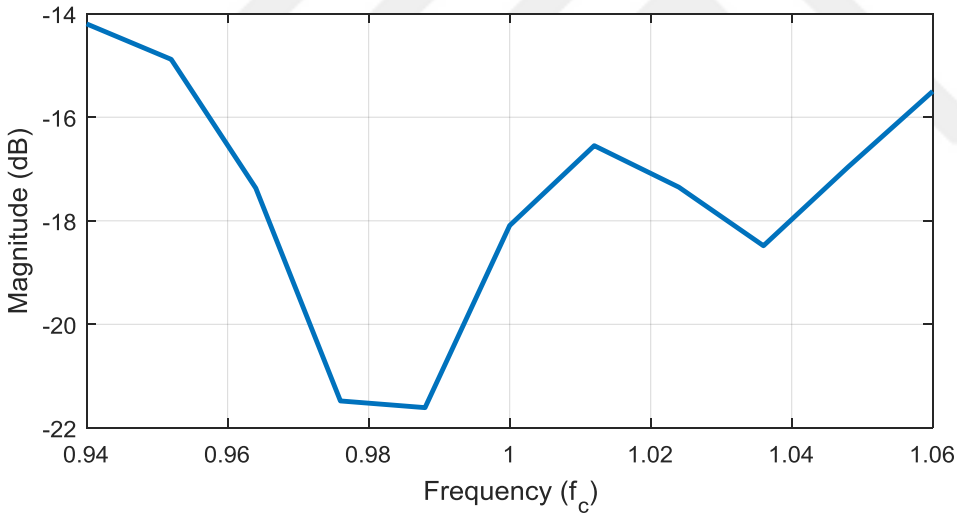

Figure 3.78. Return loss of the 8x1 Vivaldi array with the power divider network.

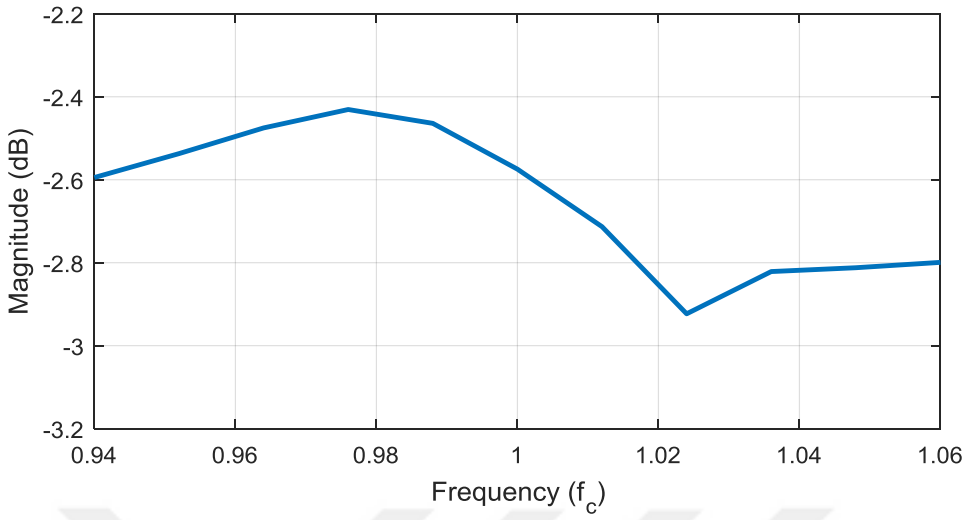

Figure 3.79. Loss of the 8x1 Vivaldi array with the power divider.

3.2.5. 56x8 Vivaldi Array Design

8x1 Vivaldi arrays are lined up along the frequency scanning axis as shown in Figure 3.80 and Figure 3.81. The excitation of the array is realized by the magnitudes of couplings obtained by the waveguide beamformer and the phases obtained by using (3.25). Normalized elevation patterns that are obtained at the conical cuts of the scan directions are given in Figure 3.82. The scanning performance in the azimuth axis is further shown in Figure 3.83 in terms of the realized gain.

The difference between the realized gain and the directivity with respect to frequency is given in Figure 3.84, which represents the loss of the 56x8 Vivaldi array fed by the 8-way power divider. The loss increases as the beams deviate from the broadside. The sources of the loss can be stated as the one due to the antenna array and the one due to the power divider. The loss due to the power divider can be calculated as -2.25 dB at the frequency of f_c in Figure 3.74. Lower loss values with this antenna architecture could be achieved if it was not necessary to form a narrow beam in the elevation axis. In that case, a single element would be employed for the

vertical axis and the loss due to the elevation beamformer, i.e., 8-way power divider, could be eliminated.

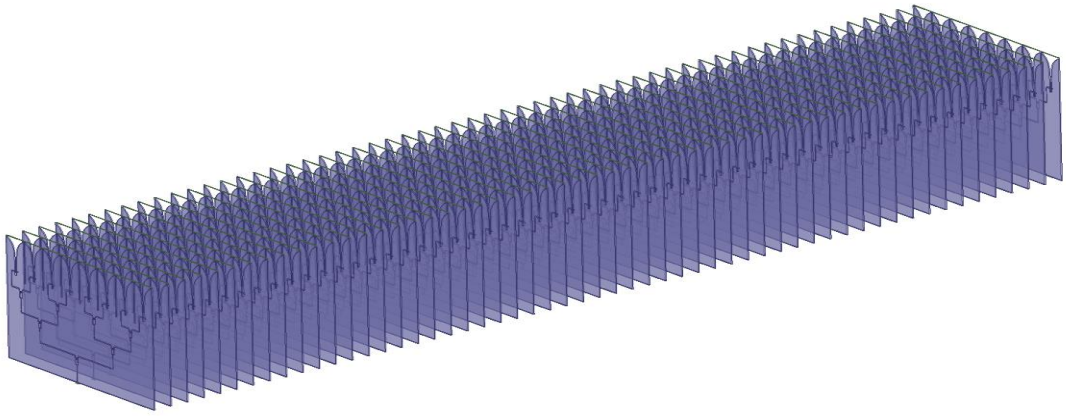

Figure 3.80. 56x8 Vivaldi array.

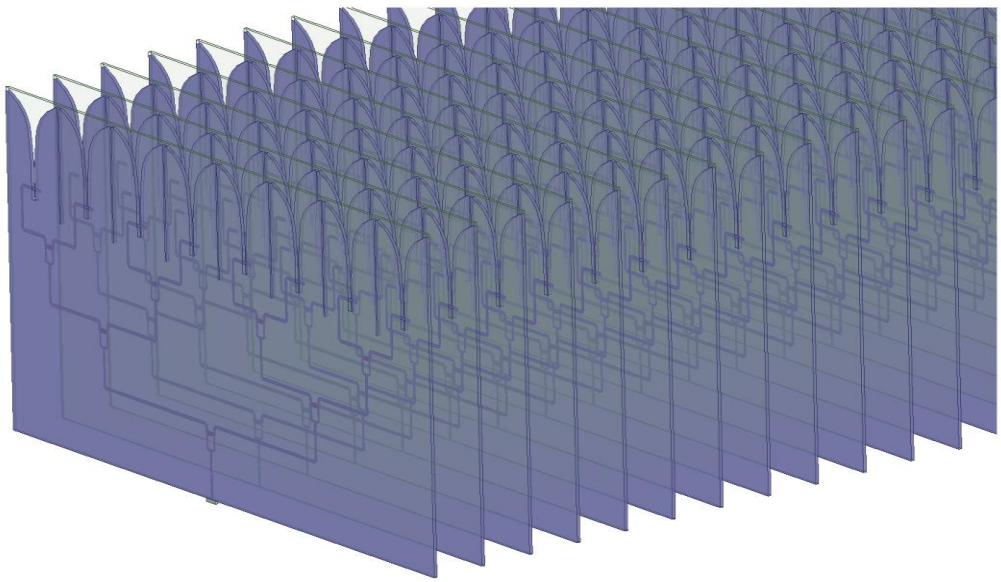

Figure 3.81. 56x8 Vivaldi array (zoomed view).

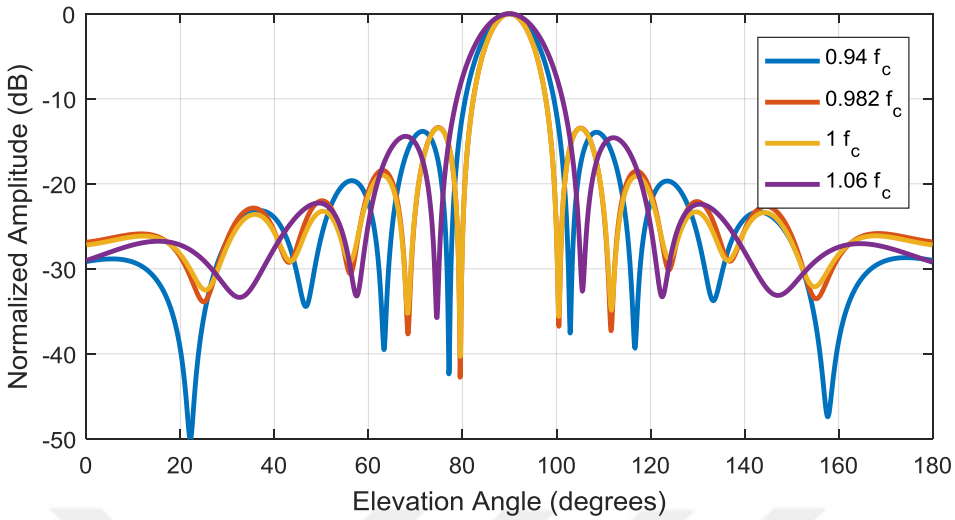

Figure 3.82. Elevation pattern of the 56x8 Vivaldi array in Figure 3.80 and Figure 3.81.

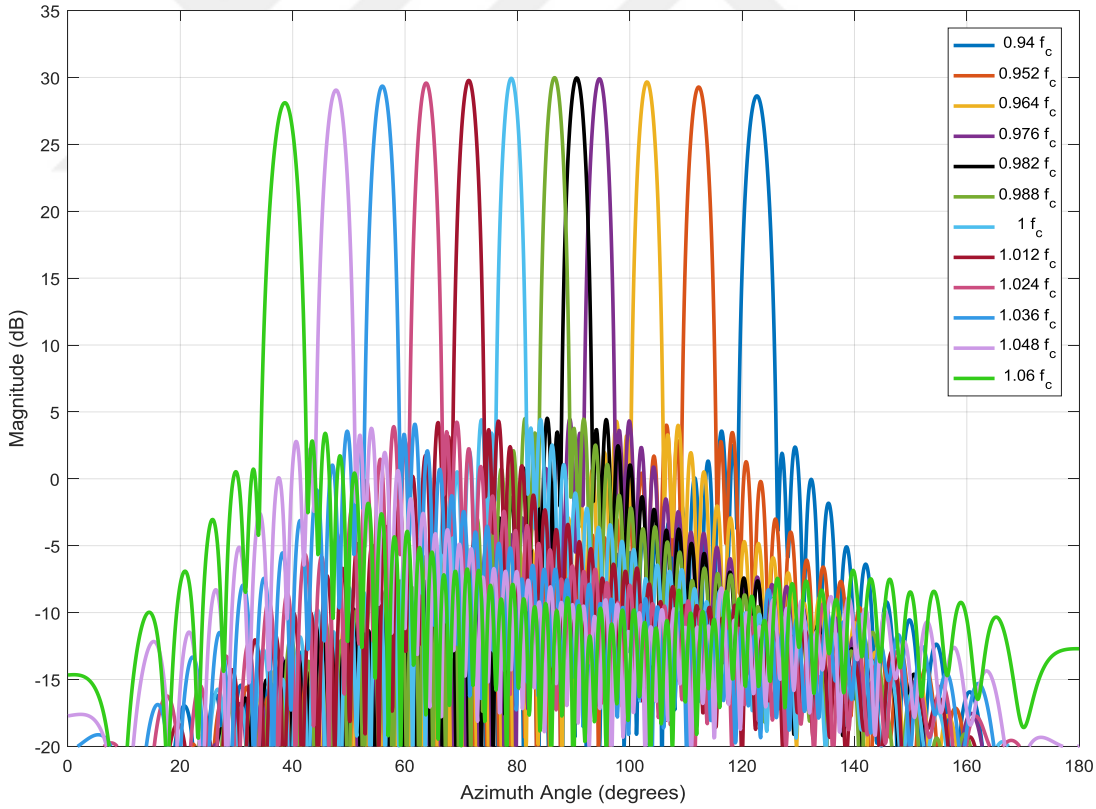

Figure 3.83. Scanning performance of the 56x8 Vivaldi array in Figure 3.80 and Figure 3.81.

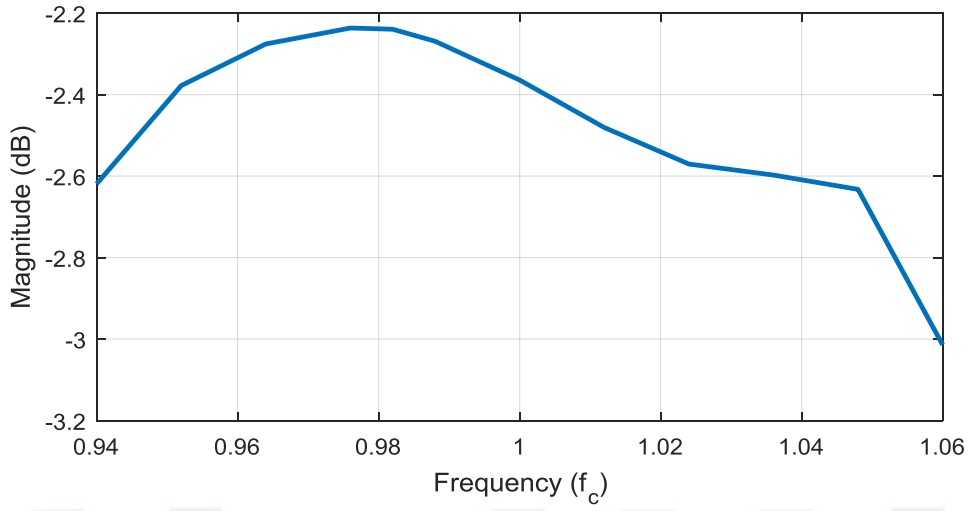

Figure 3.84. Total loss of the 56x8 Vivaldi array fed by the 8-way power divider obtained by using only the array of 56 elevation arrays, waveguide and probe transition lossless are not considered.

3.3. Final Design

The final design is formed by combining the 56x8 Vivaldi array with the beamformer network as shown in Figure 1.1 and Figure 1.2. In Figure 3.85 and Figure 3.86, plots for the solution convergence and the required memory are presented respectively. At the end of the 26th adaptive pass, number of mesh elements become 20,927,000 while the required memory reaches 473.7 GB. In Figure 3.87, patterns are given for different adaptive passes at the solution frequency (1.06 fc).

Normalized elevation patterns that are obtained at the conical cuts of the scan directions are given in Figure 3.88. It is observed that the half-power beamwidth of the antenna in elevation is 9.2° at the broadside. The patterns in the azimuth axis is further given in Figure 3.89 in terms of the realized gain. The normalized pattern in the azimuth axis is given in Figure 3.90.

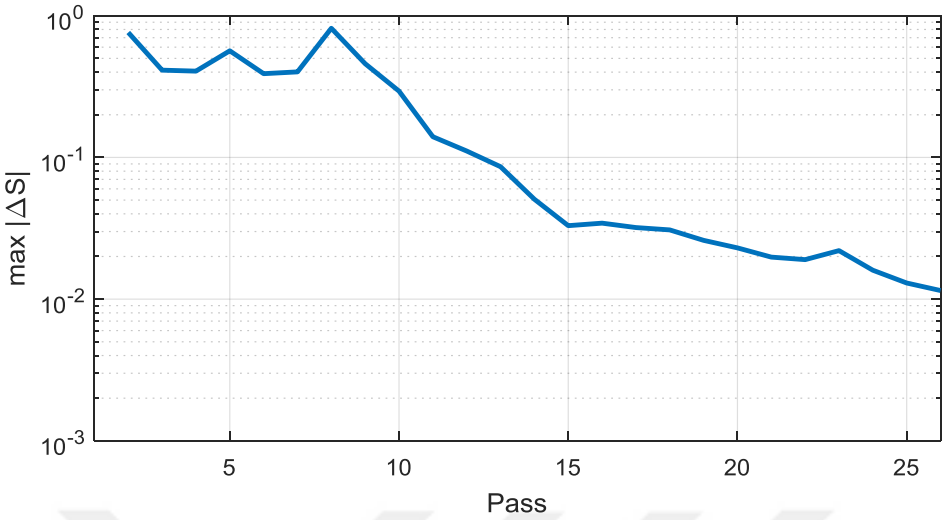

Figure 3.85. Convergence of the solution of the final beamforming network.

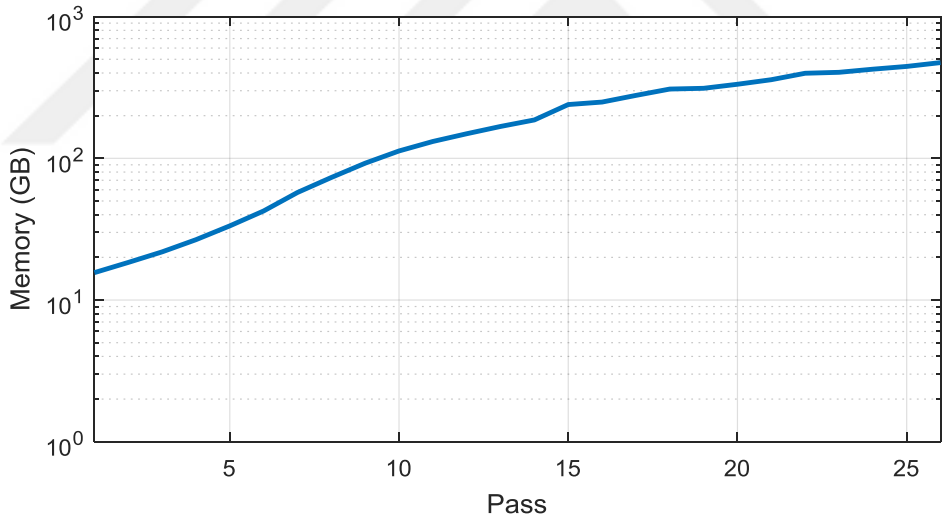

Figure 3.86. Required memory of the simulation of final beamforming network.

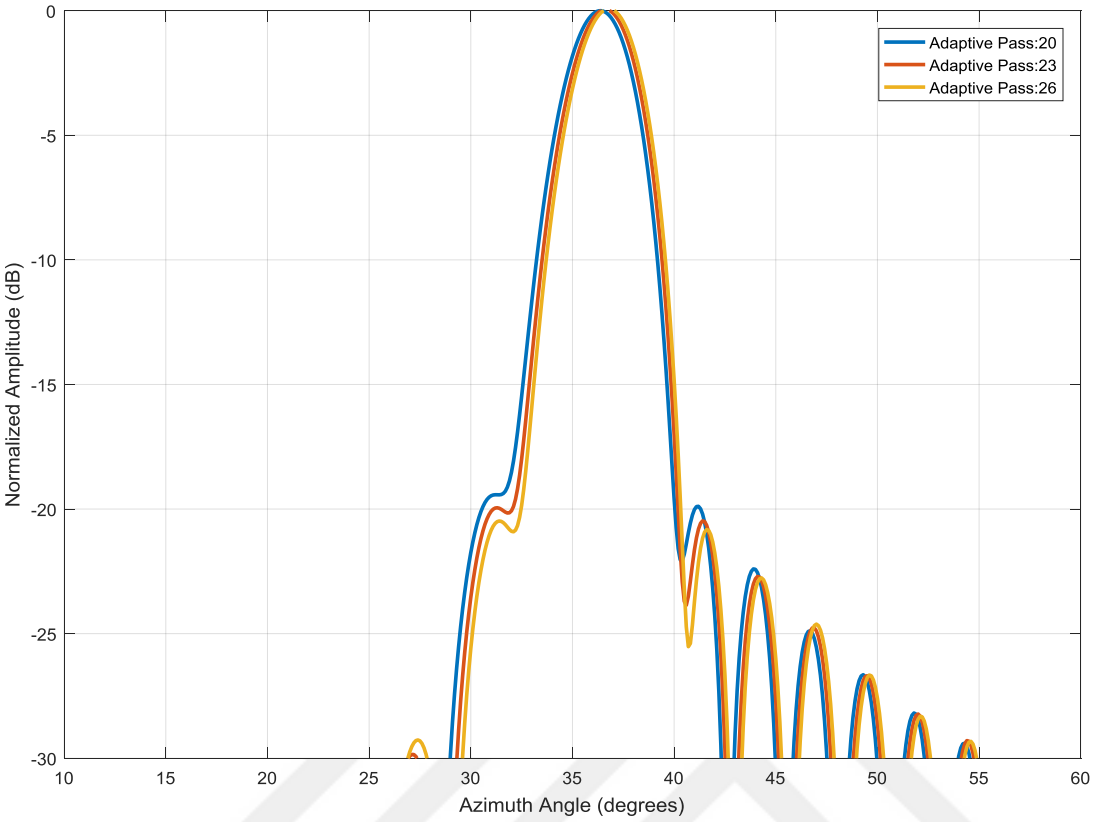

Figure 3.87. Array factor of the final beamforming network calculated with the obtained coupling coefficients for different adaptive passes and with the expected coupling coefficients at 1.06 f_c.

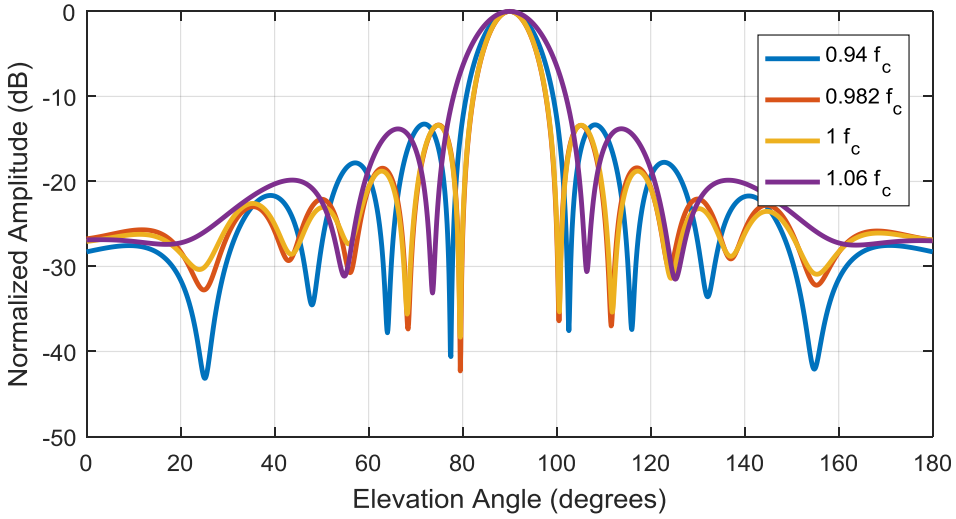

Figure 3.88. Elevation pattern obtained with the final design.

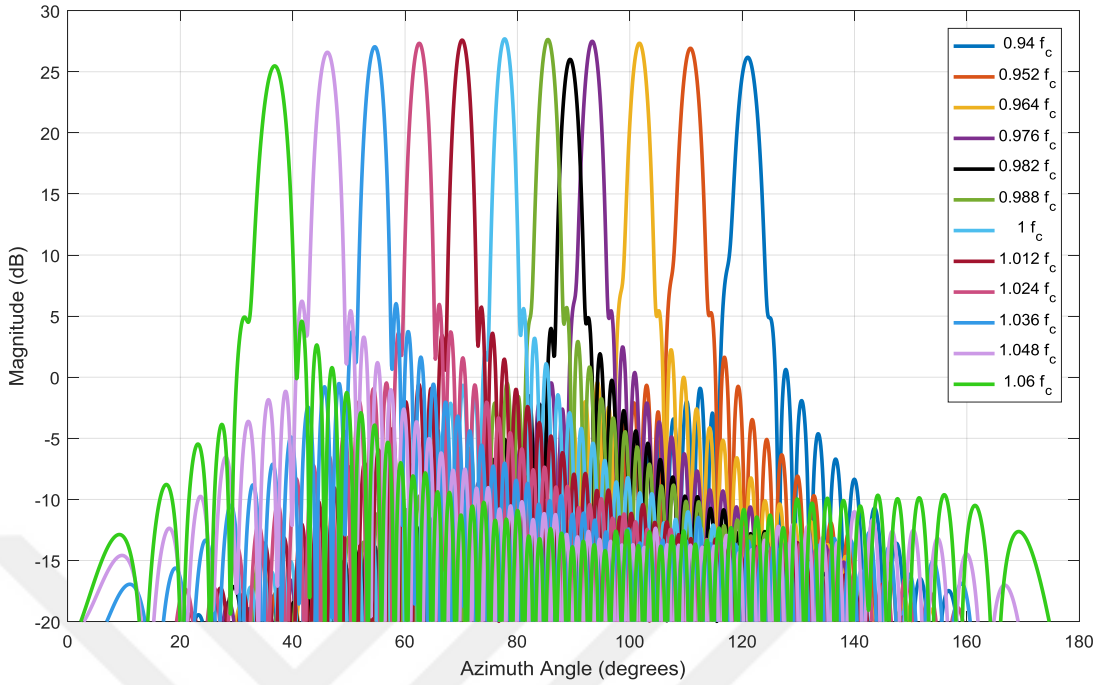

Figure 3.89. Azimuth pattern in terms of the realized gain obtained with the final design.

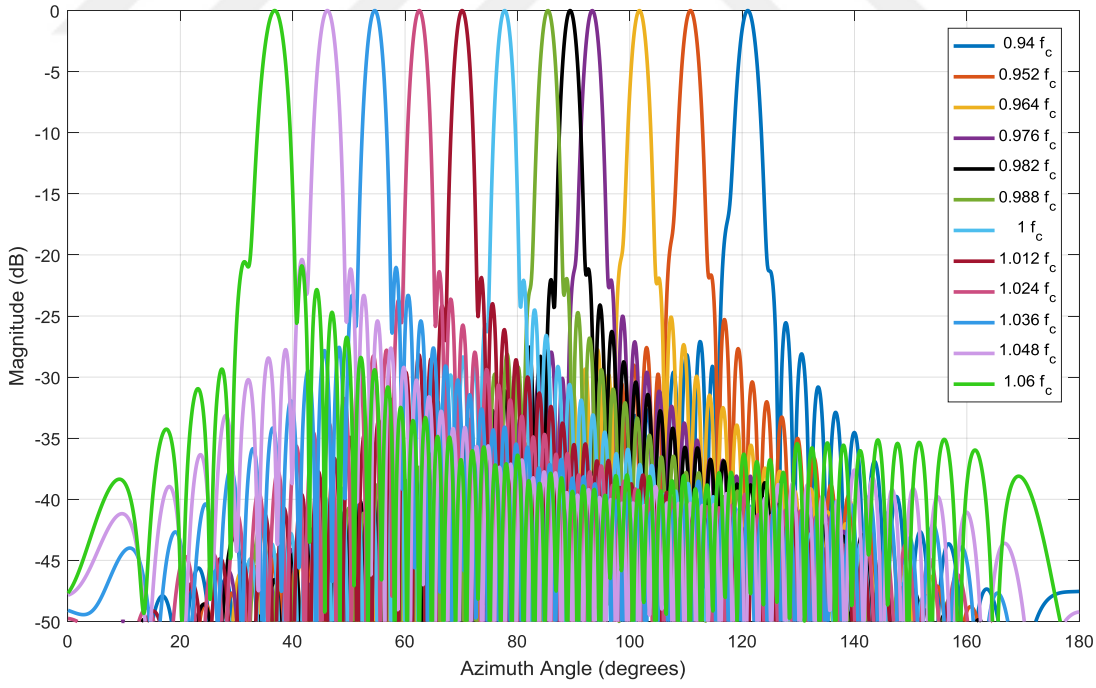

Figure 3.90. Normalized azimuth pattern obtained with the final design.

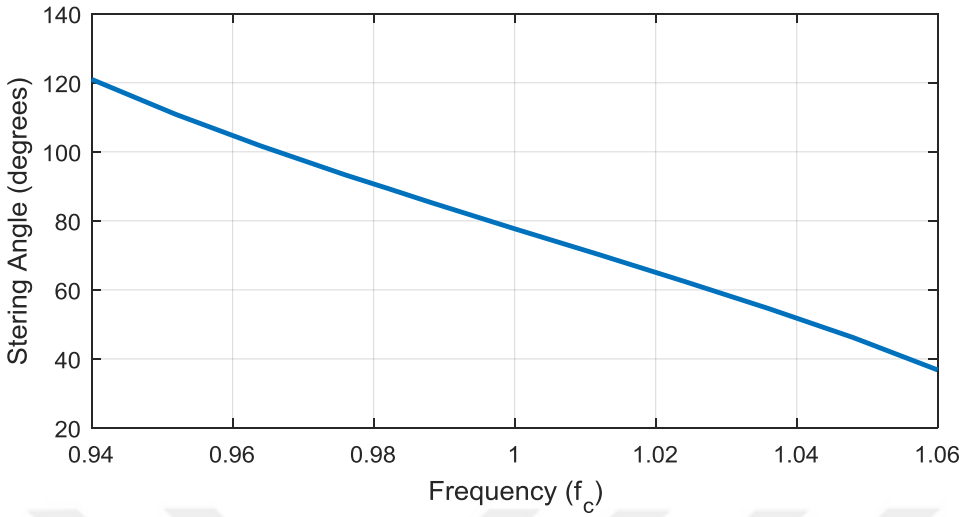

Figure 3.91. Steering angles with respect to the frequency for the final design.

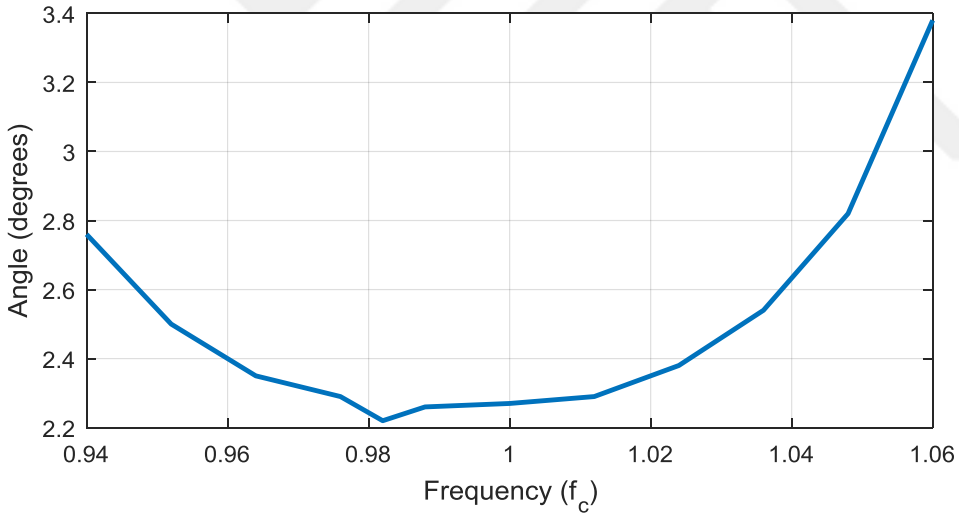

Figure 3.92. Half-power beamwidth values in the azimuth axis with respect to the frequency obtained with the final design.

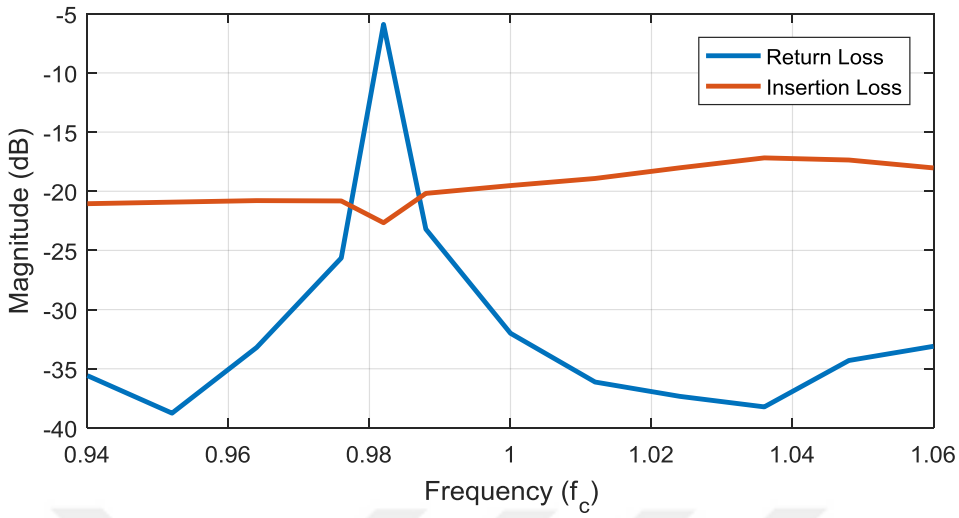

Figure 3.93. Return loss values and the power absorbed by the load for the final design.

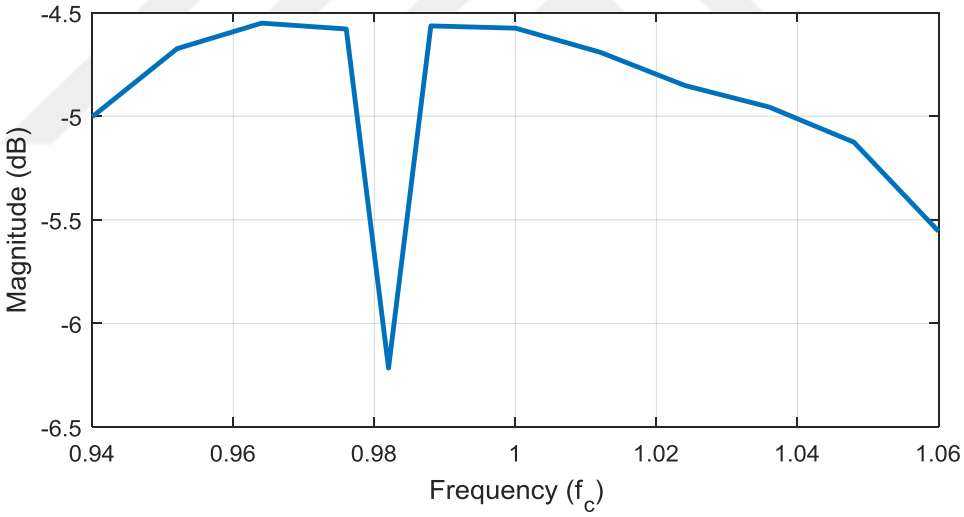

Figure 3.94. Total loss of the final design.

In Figure 3.91, steering angles are plotted with respect to frequency. It is observed that the antenna can scan from 36.8° to 121° as the frequency decreases. In Figure 3.92, half-power beamwidth values in the azimuth axis are given with respect to frequency. The beamwidth is equal to 2.2° at the broadside and the beams expand as the pattern deviates from the broadside. Side-lobe levels are below −20.5 dB for the operating frequency band.

Return loss and power absorbed by the load at the end of the array are given in Figure 3.93. The increase in the return loss at f_{bs} is something expected, as discussed previously. The difference between the peak values of the realized gain and the directivity, which is the overall loss of the antenna, is given in Figure 3.94.

The overall loss of the antenna can be divided into three parts, i.e., losses due to the beamformer network (see Figure 3.48), the 8-way power divider network (see Figure 3.75), and the antenna elements (see Figure 3.61). At the frequency for broadside radiation, the total loss is approximately −6 dB due to high return loss at the input port due to scan blindness phenomenon. For other frequencies, the total loss is below approximately −5.5 dB with maximum loss at f_{high}. At f_{high}, approximately −2.6 dB of the loss is due to the beamformer section, −2.5 dB of the loss is due to the 8-way power divider, and −0.4 dB of the loss is due to the stripline array of Vivaldi antennas. If it was not necessary to form a narrow beam in the elevation axis, a single element (or less number of elements) would be employed for the vertical axis and the loss of the 8-way power divider would be eliminated (reduced).

CHAPTER 4

FABRICATION AND MEASUREMENTS

Some prototypes related to the design procedure presented in this thesis are fabricated and tested under the technical opportunities of ASELSAN. In this chapter, measurement results obtained with the fabricated prototypes are compared with the simulation results. Fabricating and testing the complete design is left as a future work due to time limits.

4.1. S-Parameter Measurements

4.1.1. Stripline-to-Microstrip-line Transition

Due to small thickness of the dielectric card, stripline-to-microstrip-line transition and surface mount SMP connectors are decided to be used for the tests of the prototypes that have stripline ports in the simulations:

- Hybrid coupler
- 8-way power divider
- 8x1 Vivaldi array combined with the 8-way power divider.

Stripline-to-microstrip-line transition makes it possible to match surface mount SMP connectors to the stripline structure. The designed stripline-to-microstrip-line transition is shown in Figure 4.1, while its return loss plotted in Figure 4.2. The designed transition is connected back-to-back and simulated to compare with the measurement results. The printed circuit boards (PCBs) shown in Figure 4.3 are fabricated and combined using screws and support material to realize stripline-to-microstrip-line transitions that are connected back-to-back. In Figure 4.4, the fabricated stripline-to-microstrip-line transitions that are connected back-to-back and

the measurement setup is shown. Before measurements, SOLT (Short-Open-Load-Through) calibration is performed with an SMP calibration kit.

In Figure 4.5, simulation and measurement results for the return loss values of the stripline-to-microstrip-line transitions that are connected back-to-back are compared. It is observed that the transition is proper to use in the further tests. The differences between the simulation and measurement results may be due to the effect of the SMP connectors that are not included in the simulations, non-idealities in the fabrication process, and other uncertainties in the measurement setup.

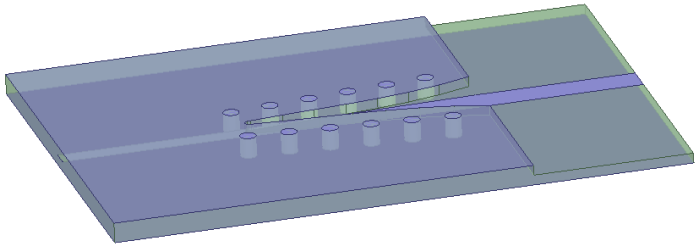

Figure 4.1. Designed stripline-to-microstrip-line transition.

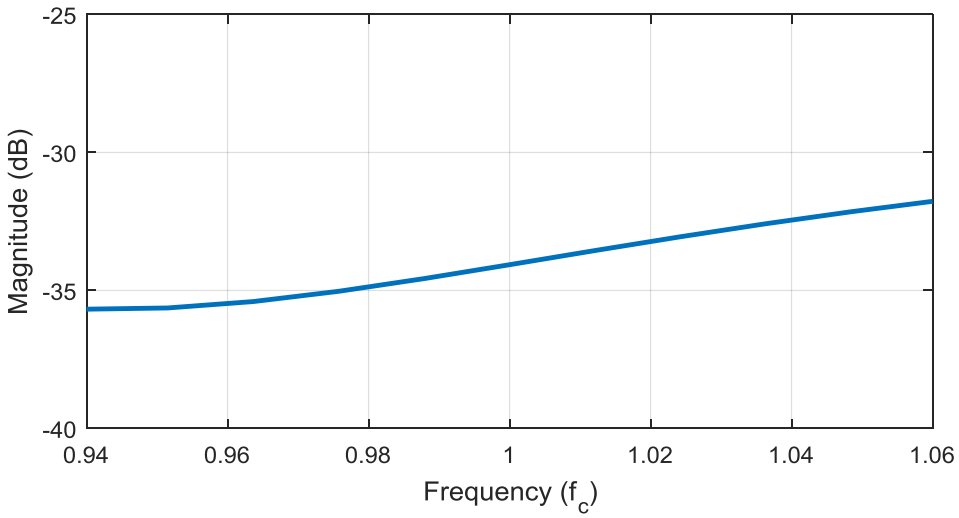

Figure 4.2. Return loss of the designed stripline-to-microstrip-line transition.

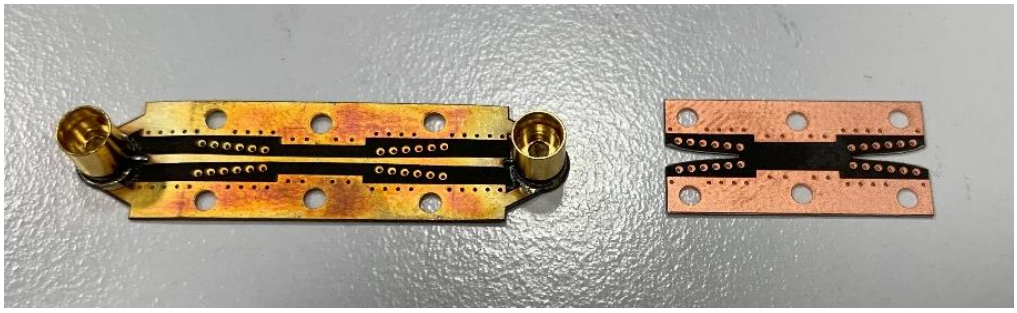

Figure 4.3. PCBs for the stripline-to-microstrip-line transitions that are connected back-to-back.

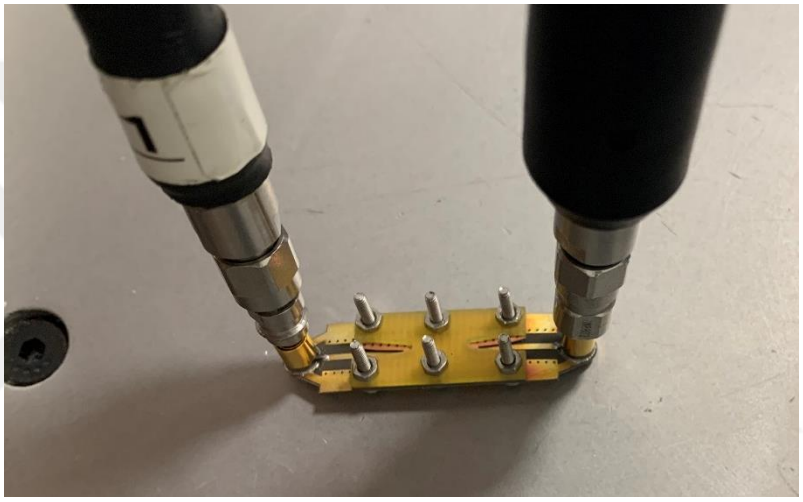

Figure 4.4. Fabricated stripline-to-microstrip-line transitions that are connected back-to-back and the measurement setup.

4.1.2. Ridged-Waveguide-to-Standard-Waveguide Transition

Transition from waveguide to coaxial connector is required for the tests of the prototypes that include ridged waveguide ports:

- Unit cell with a stripline probe
- Unit cell with hybrid coupler probe
- 8x1 Vivaldi array combined with the 8-way power divider and hybrid coupler probe.

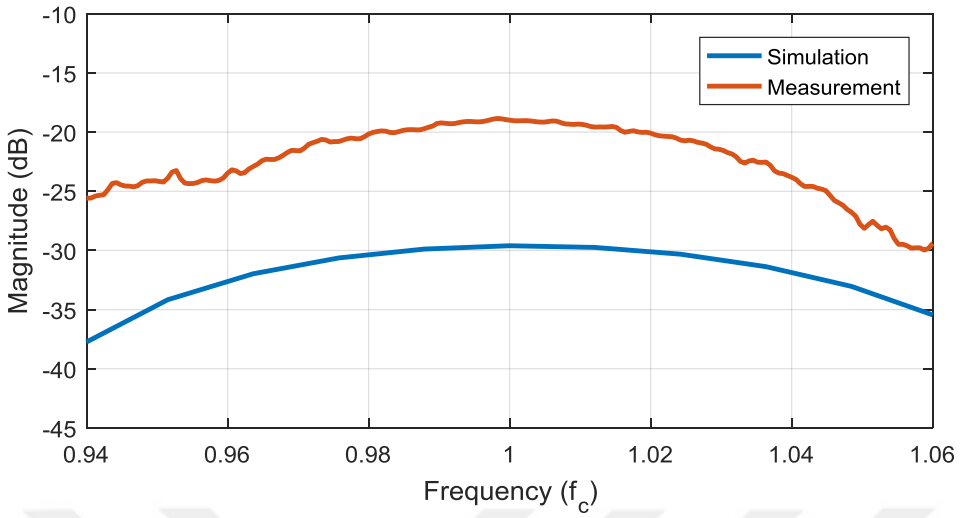

Figure 4.5. Comparison of the simulation and measurement results for the return loss of the stripline-to-microstrip-line transitions that are connected back-to-back.

For these tests, an adapter that transmits power from SMA to a standard waveguide is used by also employing a transition from ridged-waveguide to standard waveguide. The ridged-waveguide-to-standard-waveguide transition is designed to use in the tests that include ridged waveguide ports. The model for the designed transition is shown in Figure 4.6 along with the return loss given in Figure 4.7. The designed transition is connected back-to-back and simulated to compare with the measurement results. In Figure 4.8, the fabricated ridged-waveguide-to-standard-waveguide transitions that are connected back-to-back and the measurement setup is shown. Before measurements, TRL (Thru-Reflect-Line) calibration is performed, while SMA-to-standard-waveguide adapters are included in the calibration.

In Figure 4.9, simulation and measurement results for the return loss values of the ridged-waveguide-to-standard-waveguide transitions that are connected back-to-back are compared. It is observed that this transition is proper to use in the further tests that include ridged waveguide ports. The difference between the simulation and measurement results may be caused by from the misalignment of the components together with non-idealities in the fabrication process and other uncertainties in the

measurement setup. To observe the effect of the alignment via simulations, the design in Figure 4.6 is connected back-to-back in a way that the transitions are misaligned by small amounts. Simulation results for aligned and misaligned cases are compared in Figure 4.10. It can be stated that the quality of the alignment significantly affects the return loss performance of the structure, and hence, may indeed cause the difference between the ideal simulation and measurement results.

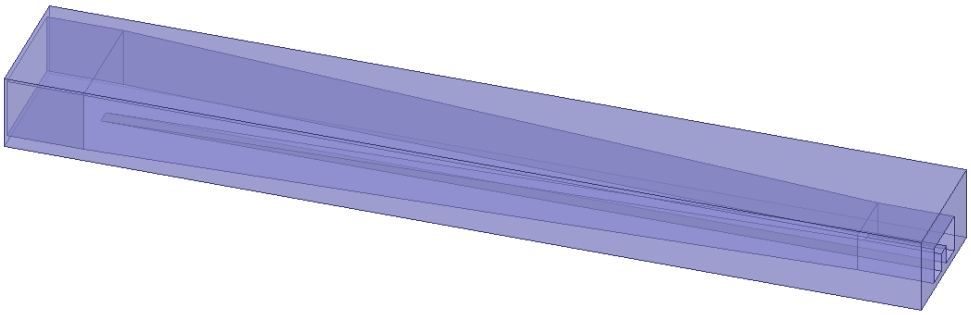

Figure 4.6. Designed ridged-waveguide-to-standard-waveguide transition.

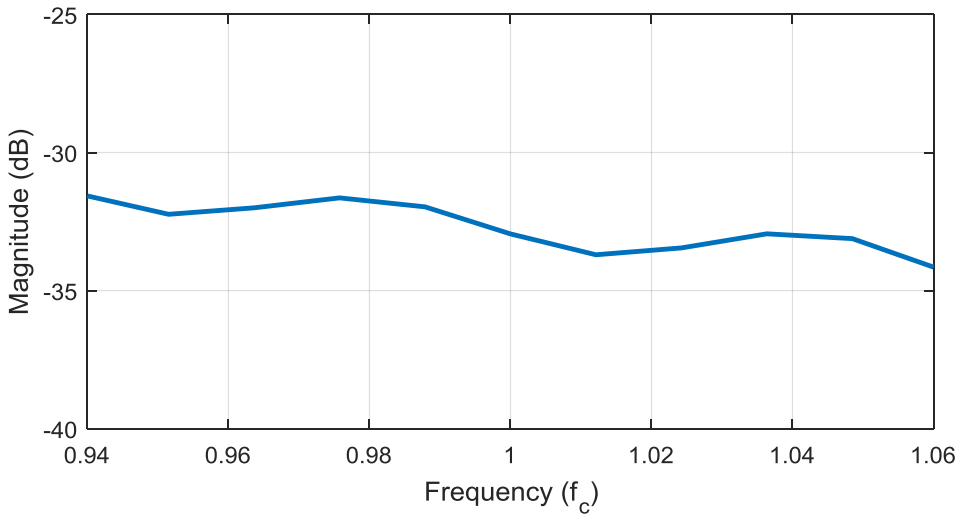

Figure 4.7. Return loss of the designed ridged-waveguide-to-standard-waveguide transition.

Figure 4.8. Fabricated ridged-waveguide-to-standard-waveguide transitions that are connected back-to-back and the measurement setup.

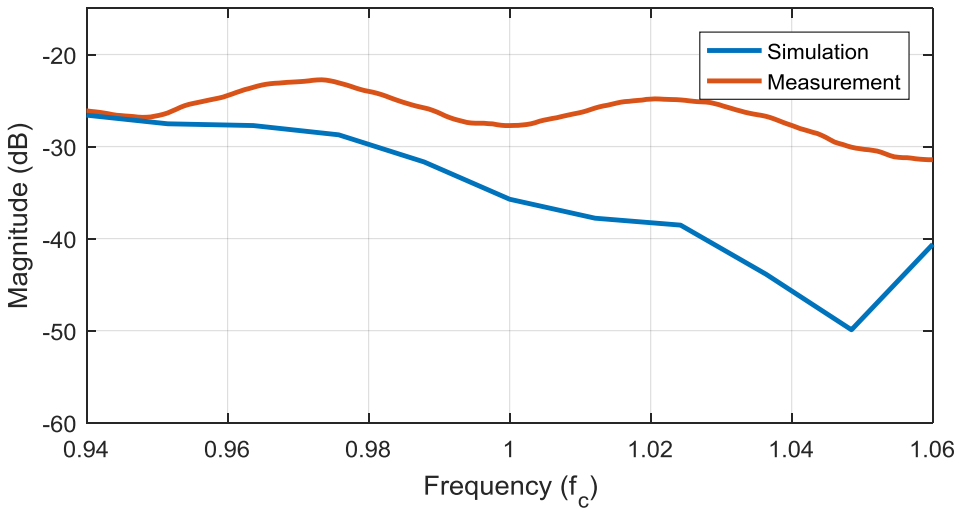

Figure 4.9. Comparison of the simulation and measurement results for the return loss of the ridged-waveguide-to-standard-waveguide transitions that are connected back-to-back.

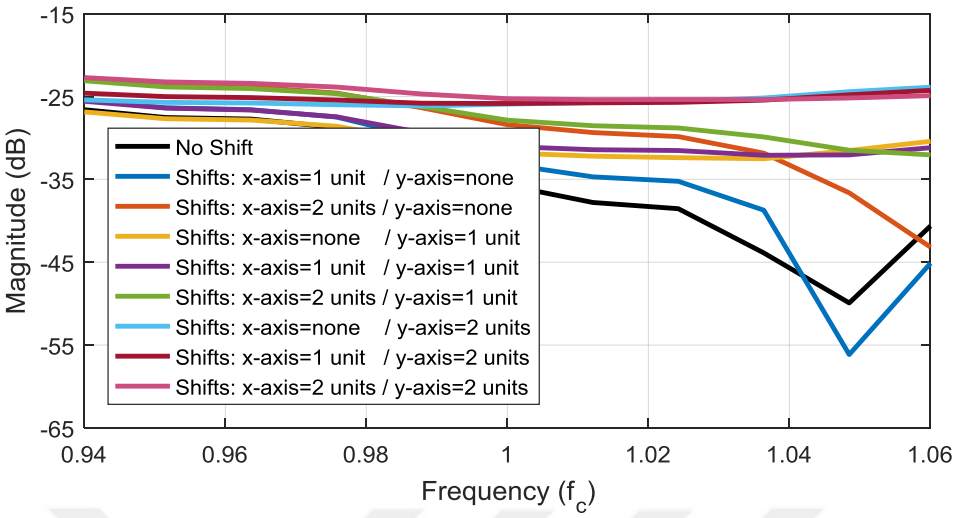

Figure 4.10. Comparisons of the return loss values for the aligned (No Shift) and misaligned back-to-back connected ridged-waveguide-to-standard-waveguide transitions. (For misaligned transitions: x-axis is along the long side of the waveguide, y-axis is along the short side of the waveguide, 1 unit = 0.0138 λ_c)

4.1.3. Unit Cell with the Single Probe

Unit cell with the single probe (see Figure 3.10) is fabricated with stripline-to-microstrip-line transitions connected at the stripline ports by joining the PCBs shown in Figure 4.11 using screws and support material and then mounting this structure on the ridged-waveguide section shown in Figure 4.12. The resulting unit cell with a single probe is shown in Figure 4.13. For measurements, both ridged-waveguide ends of the unit cell are connected to the ridged-waveguide-to-standard-waveguide transitions as shown in Figure 4.14. Before measurements, SOLT (Short-Open-Load-Through) calibration is performed with an SMA calibration kit. Thus, SMA-to-standard-waveguide and SMA-to-SMP adapters are not included in the calibrations.

To observe the effect of the probe inset length on coupling, after each S-parameter measurement, the dielectric card is demounted from the setup and the inset length is shortened for a new measurement (see Figure 4.15). Measurements are performed for five different inset lengths. For each inset length, the measurement

setup in Figure 4.14 is further modeled and simulated. In Figure 4.16, the simulation and measurement results for the coupling are compared for different inset lengths. Despite the measurement uncertainties mentioned in Section 4.1.1−4.1.2, as well as the effects of the adapters that are not included in the calibrations and possible errors on the measured inset lengths, the unit cell measurement results show reasonable consistency with simulation results. Moreover, since the PCBs are combined with screws, at the section of the probe that is inside the waveguide PCBs may not be fully attached which may also affect the results.

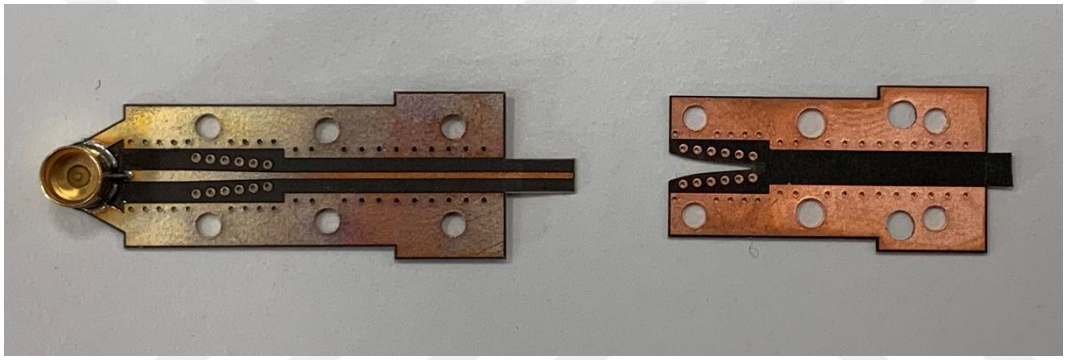

Figure 4.11. PCBs for the single probe.

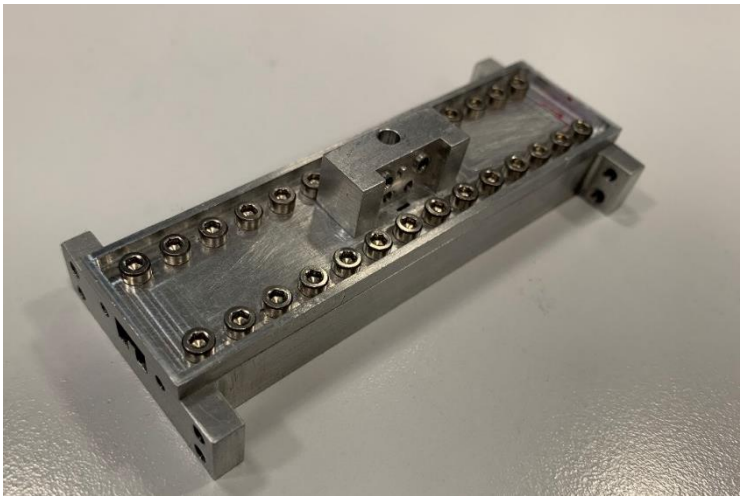

Figure 4.12. Ridged-waveguide section to mount the single probe.

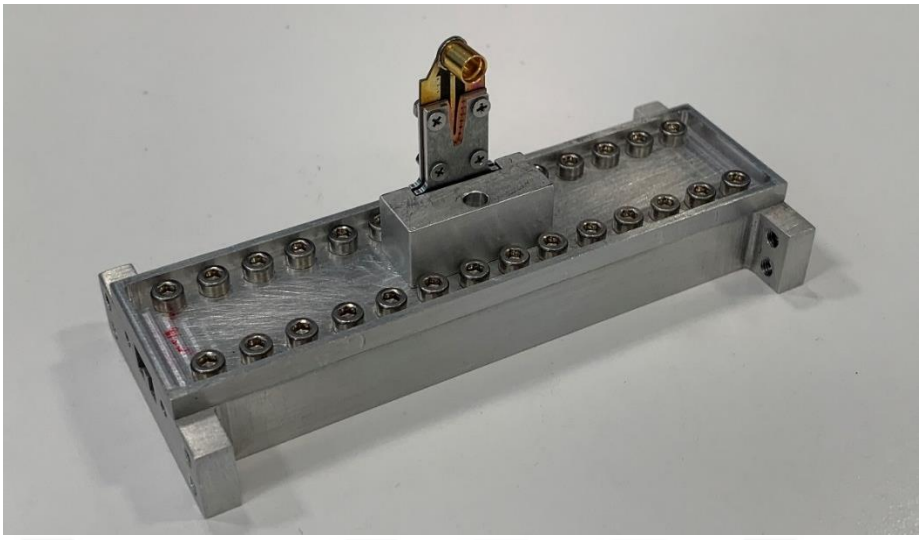

Figure 4.13. Fabricated unit cell with the single probe.

Figure 4.14. Measurement setup for the unit cell with the single probe.

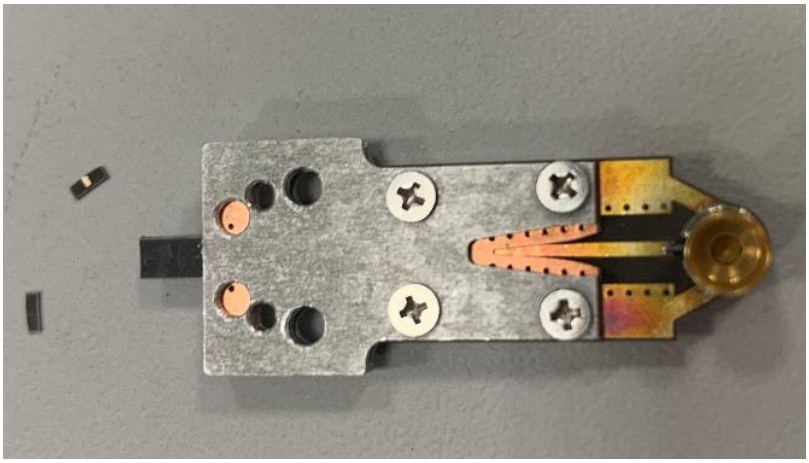

Figure 4.15. Shortening the inset length of the single probe.

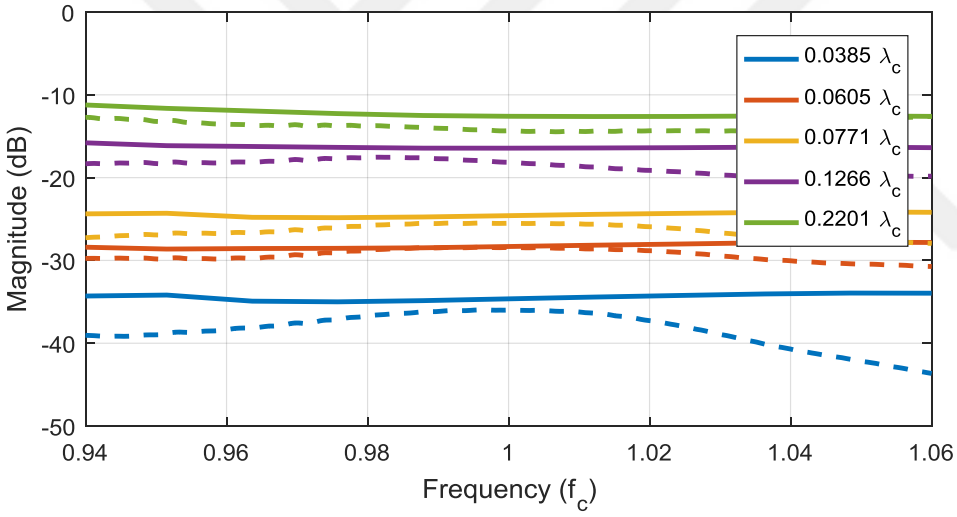

Figure 4.16. Comparison of the simulation (solid line) and the measurement (dashed line) results for the coupling of the unit cell with the single probe.

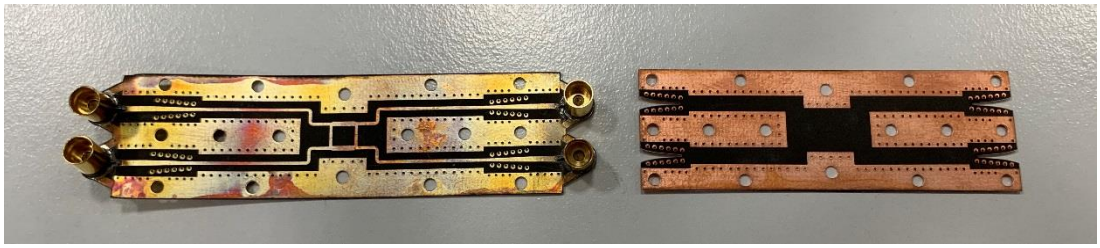

Figure 4.17. PCBs for the hybrid coupler structure.

4.1.4. Hybrid Coupler

The hybrid coupler used in the unit cell with a hybrid coupler probe (see Figure 3.17) is modeled again with stripline-to-microstrip-line transitions connected at the stripline ports. The PCBs shown in Figure 4.17 are fabricated and combined using screws and support material. In Figure 4.18, the fabricated hybrid coupler and its measurement setup are shown. Before measurements, SOLT (Short-Open-Load-Through) calibration is performed with an SMP calibration kit.

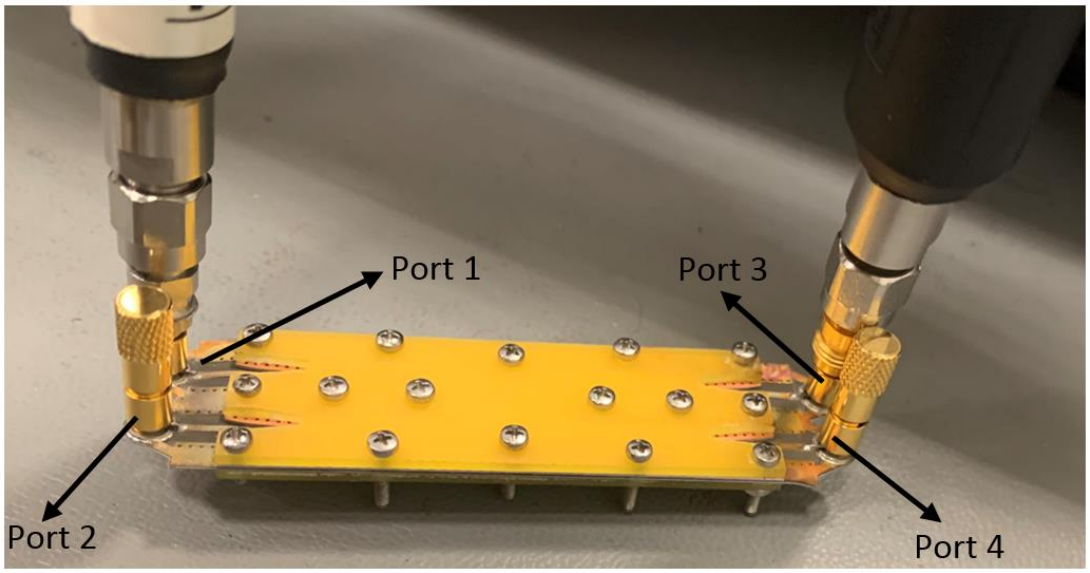

Figure 4.18. Fabricated hybrid coupler and the measurement setup.

In Figure 4.19 and Figure 4.20, coupling values (S_{31} and S_{41} in Figure 4.18) obtained via simulation and measurement are presented. In Figure 4.21, phase differences between S_{31} and S_{41} are plotted for both simulation and measurement results. The differences between the simulation and measurement results may be due to the uncertainties mentioned in Section 4.1.1.

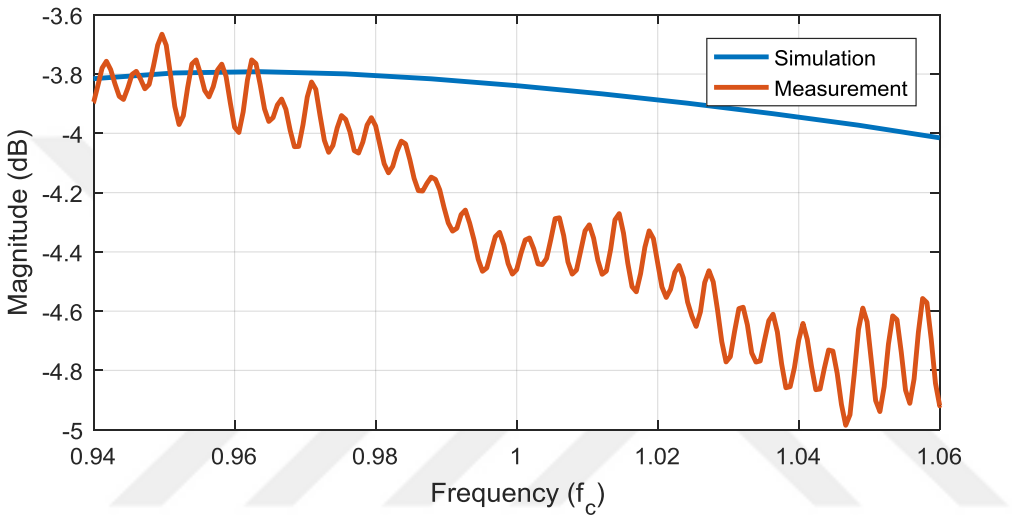

Figure 4.19. Comparison of the simulation and measurement results for the coupling (S_{31}) of the hybrid coupler.

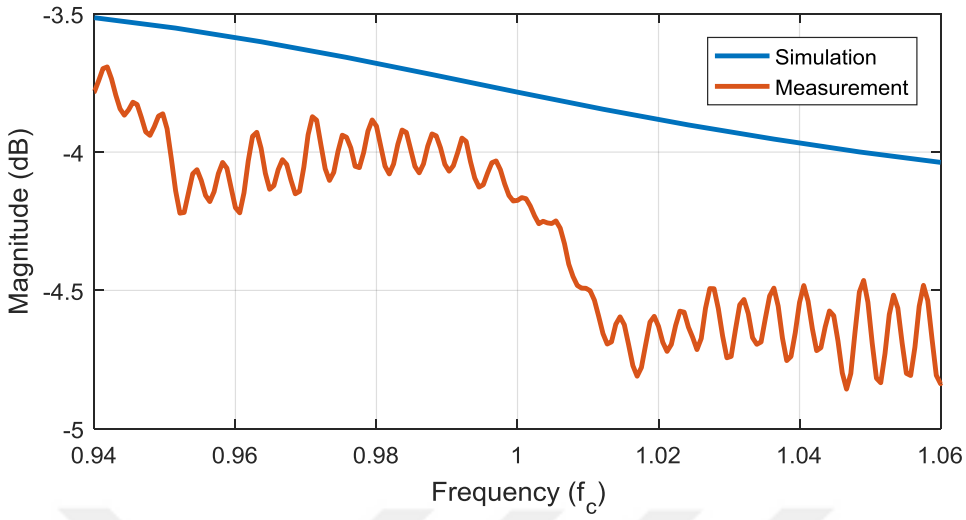

Figure 4.20. Comparison of the simulation and measurement results for the coupling (S_{41}) of the hybrid coupler.

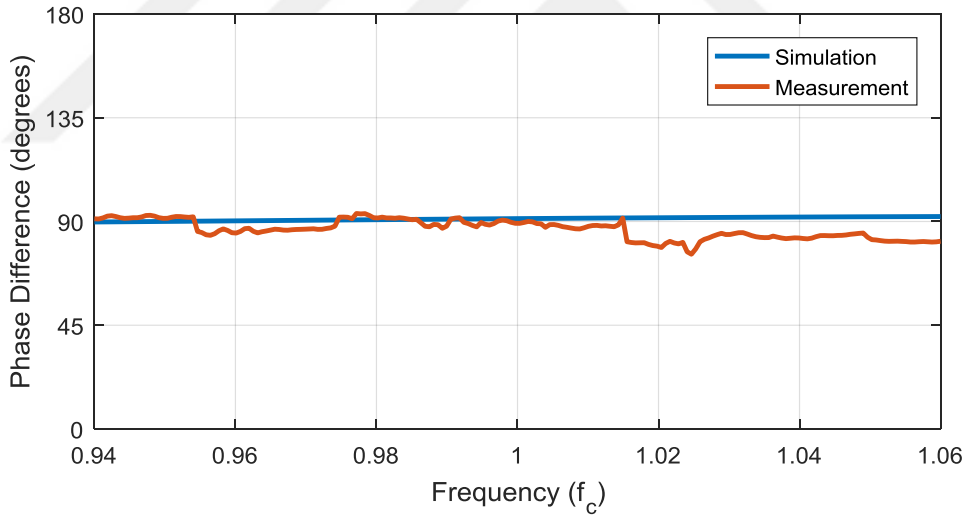

Figure 4.21. Comparison of the simulation and measurement results for the phase difference between S_{31} and S_{41}.

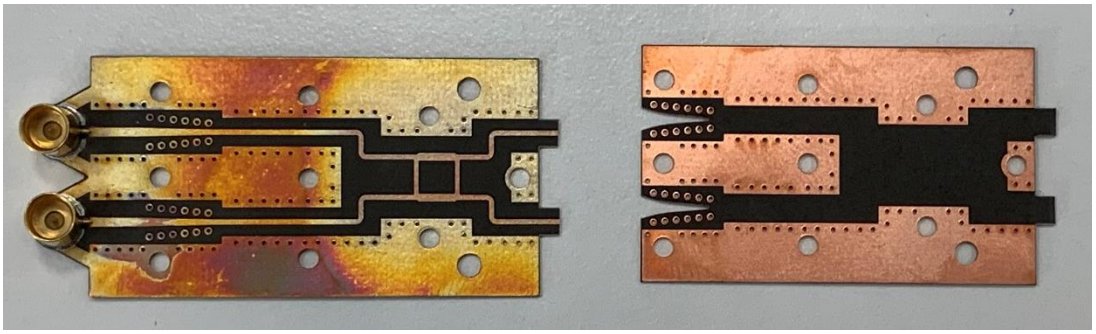

Figure 4.22. PCBs for the hybrid coupler probe.

4.1.5. Unit Cell with the Hybrid Coupler Probe

Unit cell with the hybrid coupler probe (see Figure 3.17) is fabricated with stripline-to-microstrip-line transitions connected at the stripline ports by joining the PCB cards shown in Figure 4.22 using screws and support material and then mounting this structure on the ridged-waveguide section shown in Figure 4.23. The fabricated unit cell with the hybrid coupler probe is shown in Figure 4.24. For measurements, similar to the unit cell with the single probe, both ridged-waveguide ends of the unit cell are connected to the designed ridged-waveguide-to-standard-waveguide transitions as shown in Figure 4.25. Calibration for the unit cell with the single probe is also used in this setup.

To observe the effect of the inset length on coupling, after each S-parameter measurement, the dielectric card is demounted from the setup and the inset length is shortened for a new measurement (see Figure 4.26). Measurements are performed for six different inset lengths. For each inset length, the measurement setup in Figure 4.25 is further modeled and simulated. In Figure 4.27, the simulation and measurement results for the coupling are compared for different inset lengths. Despite the measurement uncertainties mentioned for the measurement of unit cell with the single probe (Section 4.1.3), measurements of the unit cell with the hybrid coupler probe lead to coherent results with simulations. The effects of the errors in the coupling values are further investigated at Section 4.3 by an error analysis.

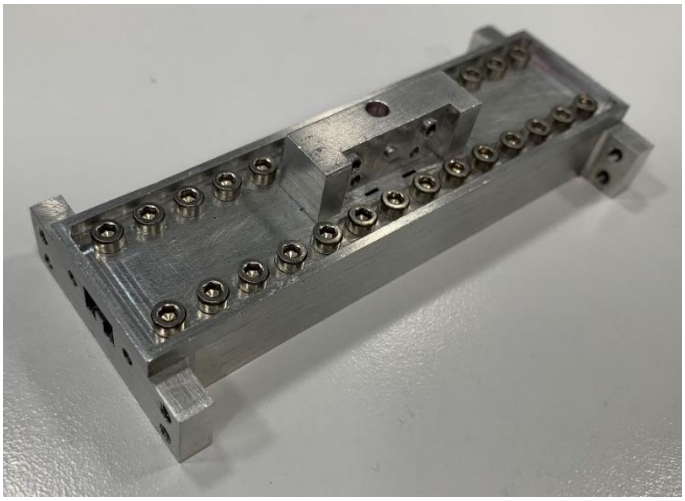

Figure 4.23. Ridged waveguide section to mount the hybrid coupler probe.

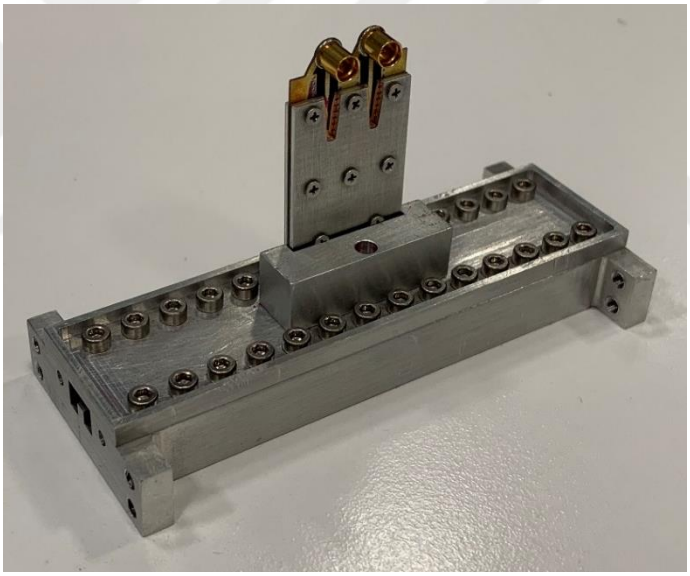

Figure 4.24. Fabricated unit cell with the hybrid coupler probe.

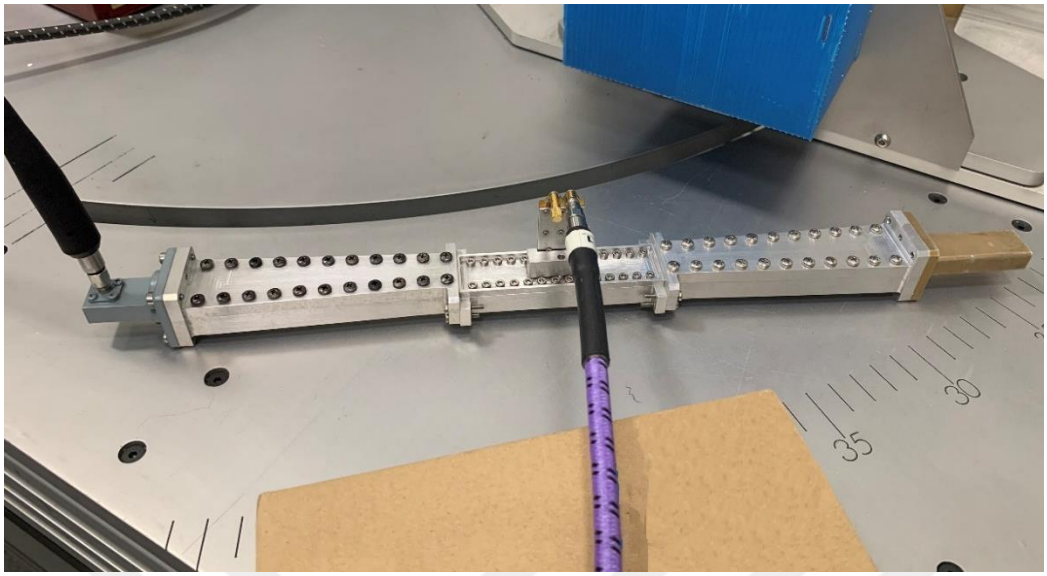

Figure 4.25. Measurement setup for the unit cell with the hybrid coupler probe.

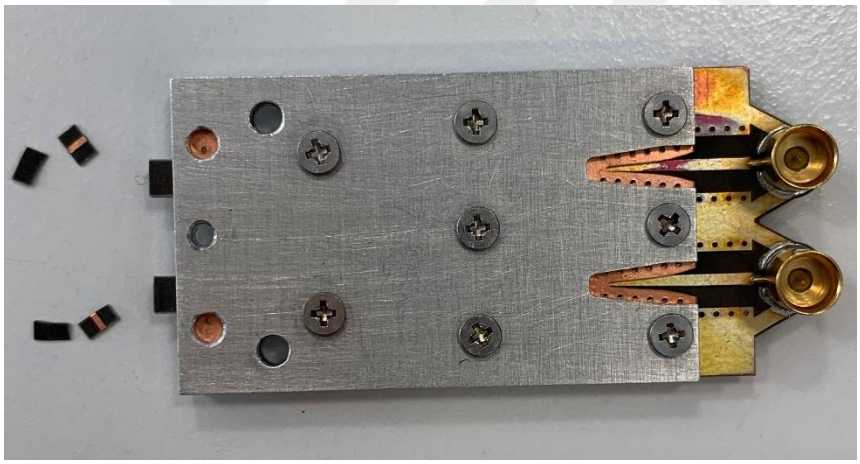

Figure 4.26. Shortening the inset length of the hybrid coupler probe.

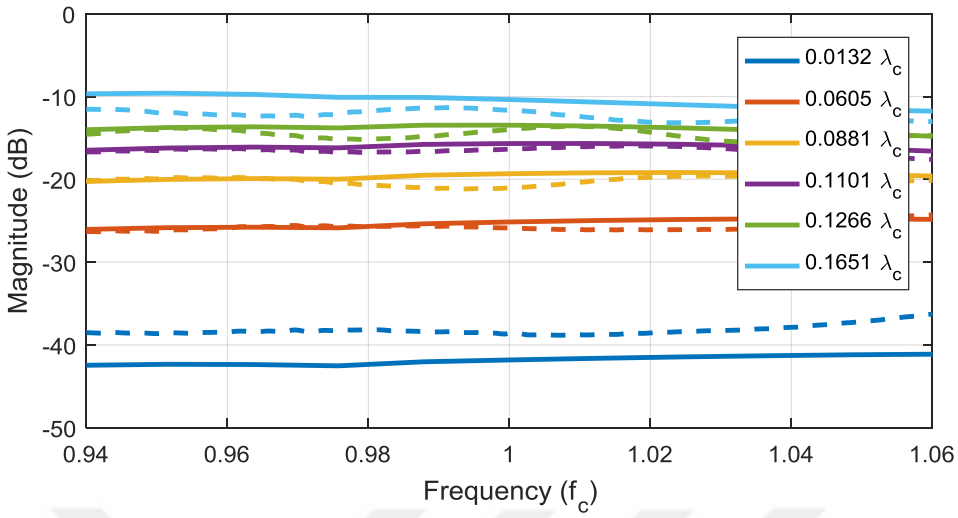

Figure 4.27. Comparison of the simulation (solid line) and the measurement (dashed line) results for the coupling of the unit cell with the hybrid coupler probe.

4.1.6. 8-Way Power Divider

The 8-way power divider in Figure 3.71 is modeled again with stripline-to-microstrip-line transitions connected at the stripline ports and fabricated by combining the PCB cards shown in Figure 4.28 using screws and support material. In Figure 4.29, the fabricated 8-way power divider and its measurement setup are shown. Before measurements, SOLT (Short-Open-Load-Through) calibration is performed with an SMP calibration kit. In Figure 4.30, simulation and measurement results for the return loss of the power divider are compared. The difference between the simulation and measurement results may be due to the uncertainties mentioned in Section 4.1.1.

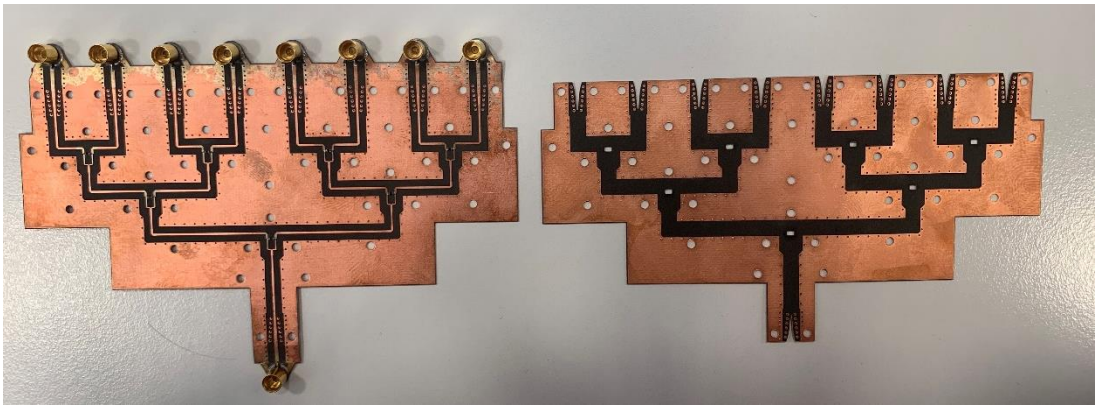

Figure 4.28. PCBs for the 8-way power divider.

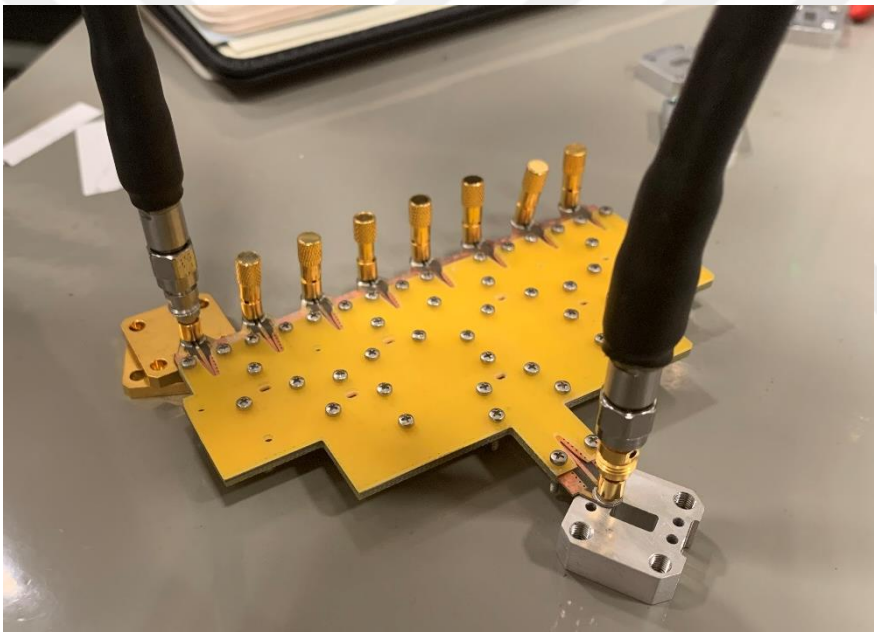

Figure 4.29. Fabricated 8-way power divider and the measurement setup.

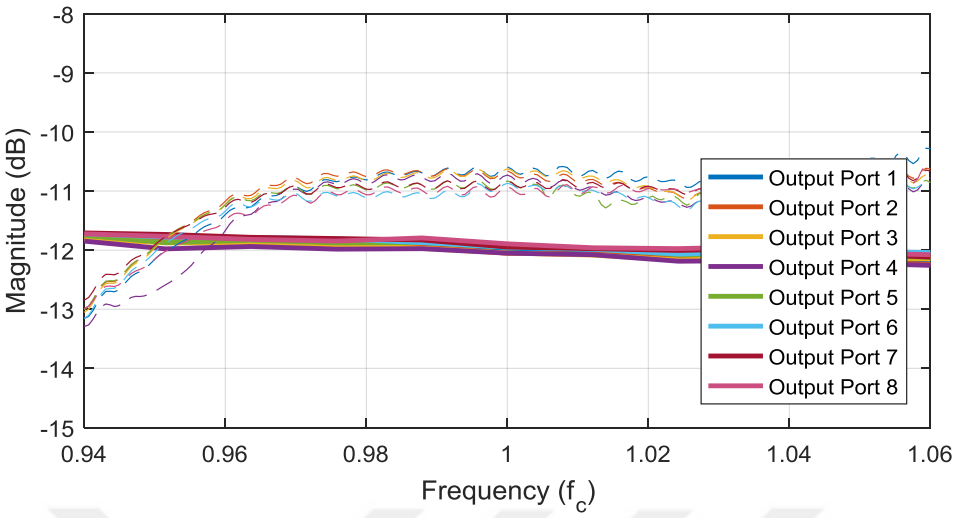

Figure 4.30. Comparison of the simulation (solid line) and measurement (dashed line) results for the insertion loss of the 8-way power divider.

4.1.7. 8x1 Vivaldi Array Combined with the 8-Way Power Divider

The8x1 Vivaldi array combined with the 8-way power divider in Figure 3.76 is modeled again and simulated with stripline-to-microstrip-line transitions connected at the input port and without any periodic boundaries. By combining the PCB cards shown in Figure 4.31 using screws and support material, the 8x1 Vivaldi array combined with the 8-way power divider is fabricated as shown in Figure 4.32.

Before measurements, SOLT (Short-Open-Load-Through) calibration is performed with an SMP calibration kit. Measurements are performed in the environment that is also used for pattern measurements described in the next section. Simulation and measurement results are compared for the return loss in Figure 4.33. The difference between the simulation and measurement results may be due to the uncertainties mentioned in Section 4.1.1 and undesired reflections from the environment.

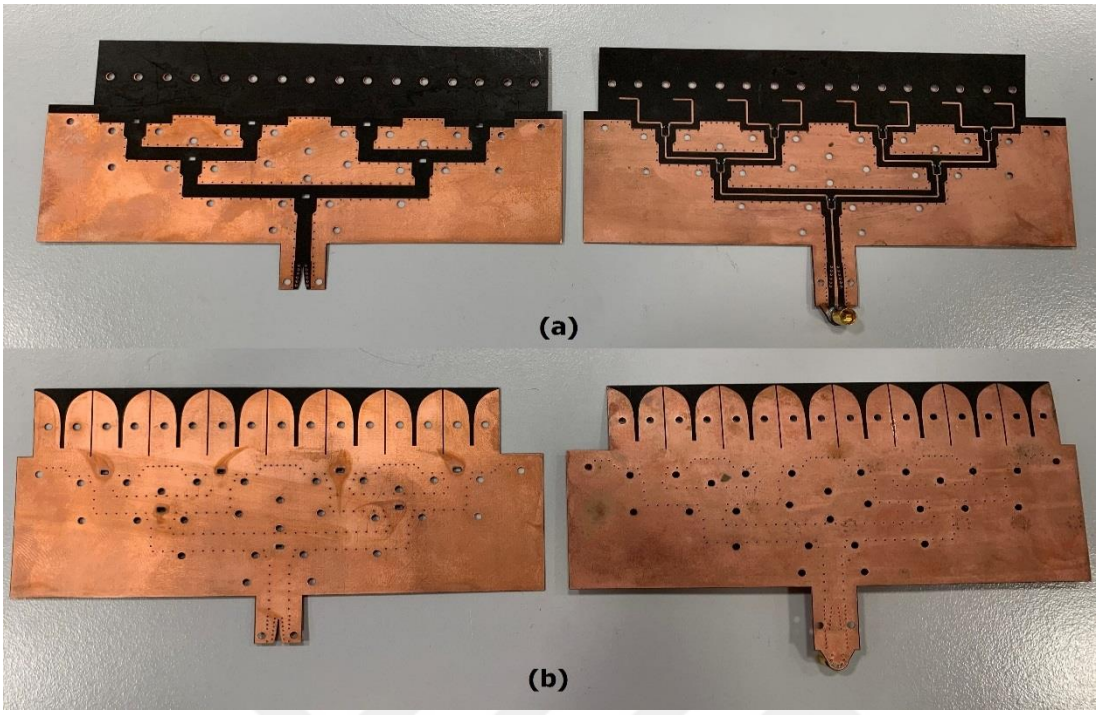

Figure 4.31. PCBs for 8-way power divider. (a) Front, (b) Back.

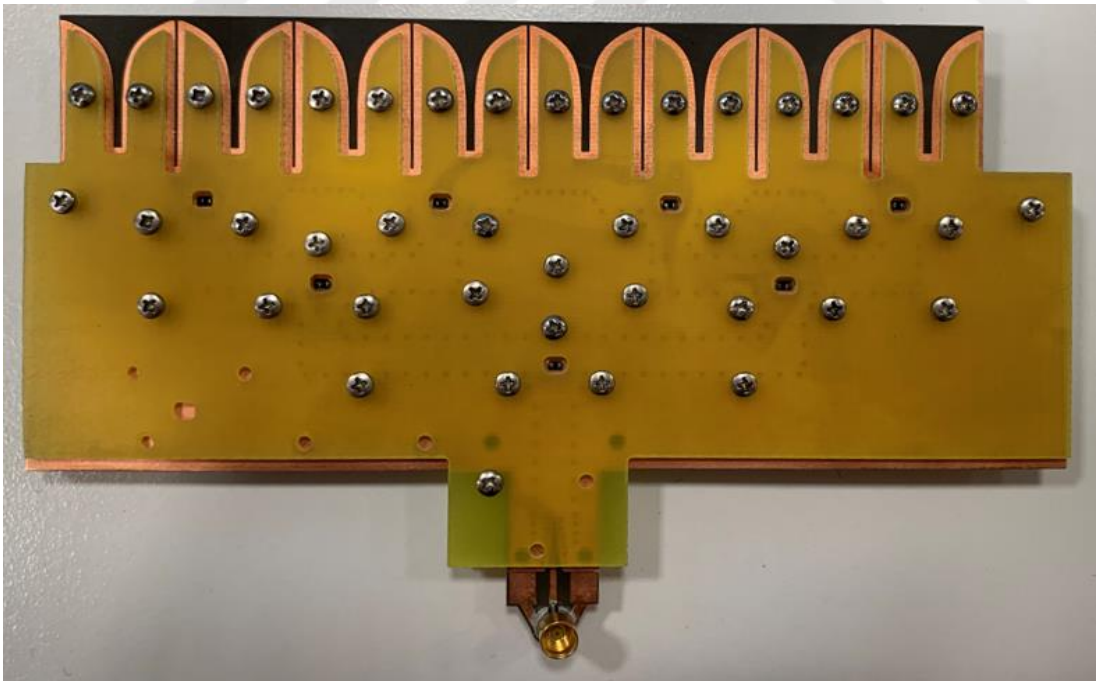

Figure 4.32. Fabricated 8x1 Vivaldi array combined with the 8-way power divider.

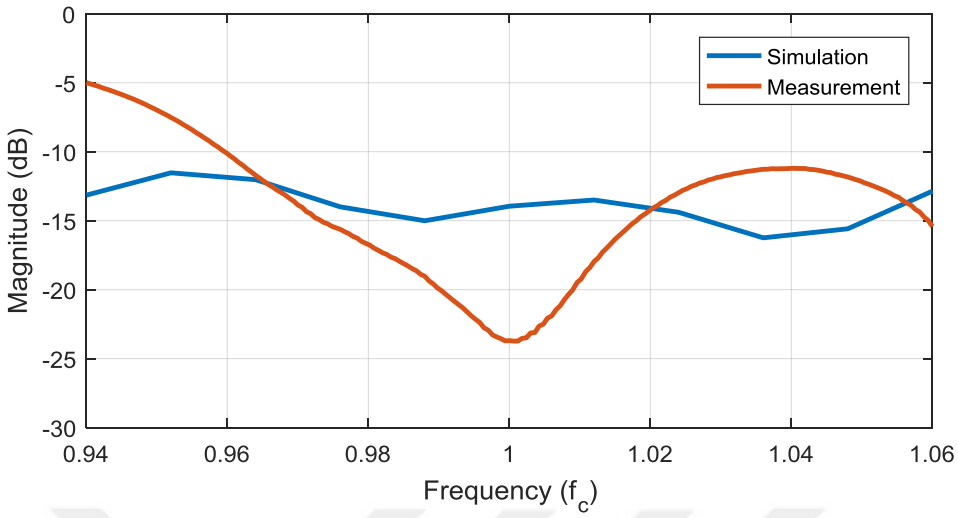

Figure 4.33. Comparison of the simulation and measurement results for the return loss.

4.2. Pattern Measurements

The setup for antenna measurements is shown in Figure 4.34. In this setup, the feeds of the antennas are connected to the network analyzer. While the antenna under test (AUT) rotates 360° around its vertical axis, the other (receiver) antenna, which is located in the far-field of AUT, receives the field radiated by AUT. Then, by S21 measurements, the far-field pattern of AUT is obtained in the horizontal axis, i.e., E-plane of the antenna. The environment in which the measurements are performed is covered with absorber materials to minimize reflections.

4.2.1. 8x1 Vivaldi Array Combined with the 8-way Power Divider

Measurement setup for the fabricated 8x1 Vivaldi array combined with the 8-way power divider (see Figure 4.32) is shown in Figure 4.34, while the antenna under test is focused in Figure 4.35. Simulation and measurement results for the E-plane far-field pattern at three different frequencies are compared in Figure 4.36 to Figure 4.38. It is observed that side lobes are affected and asymmetries are observed in the patterns of the fabricated antennas. In addition, half-power beamwidth values obtained via

simulation and measurement are compared in Figure 4.39. The difference between half-power beamwidths of the simulated and fabricated array is below 0.52° over the frequency band of operation. The differences between the simulation and measurement results may be due to uncertainties mentioned in Section 4.1.1. Especially, the errors on alignment and compression of the PCBs while combining with screws and support material may affect the results.

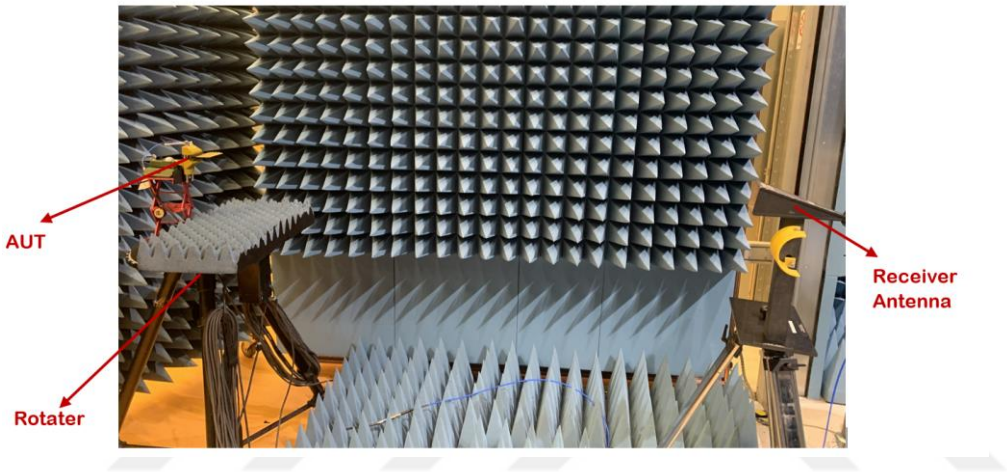

Figure 4.34. Measurement setup for the pattern measurements.

Figure 4.35. 8x1 Vivaldi array combined with the 8-way power divider under test.

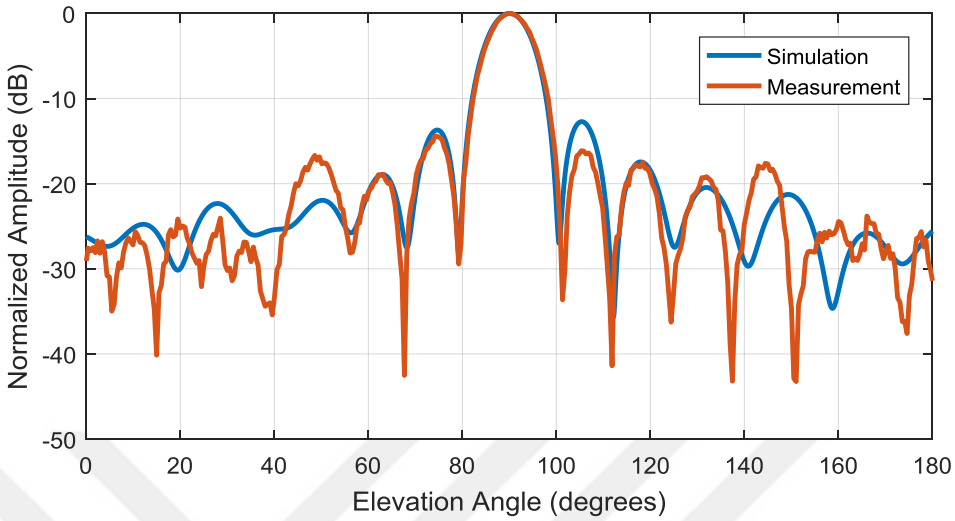

Figure 4.36. Comparison of the simulation (dashed line) and the measurement (solid line) results for the far-field pattern at 0.94 f_c.

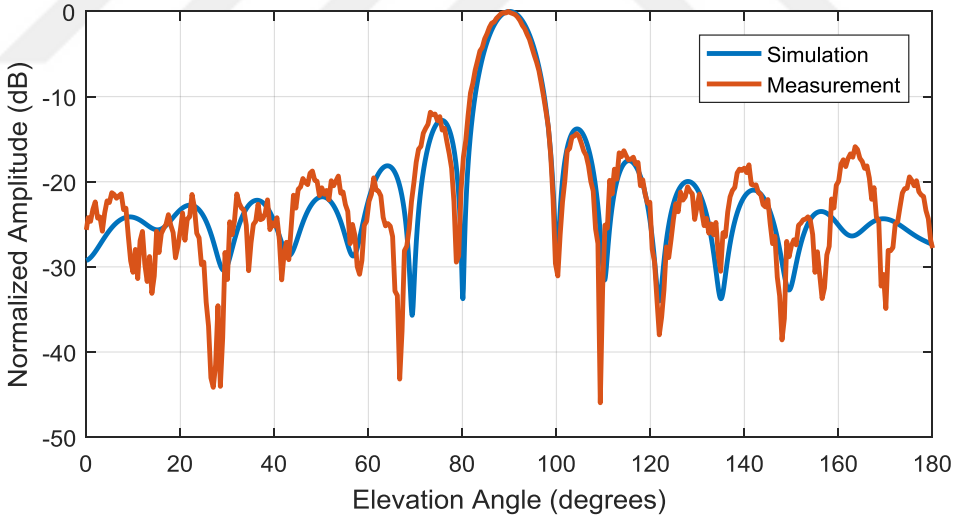

Figure 4.37. Comparison of the simulation (dashed line) and the measurement (solid line) results for the far-field pattern at f_c.

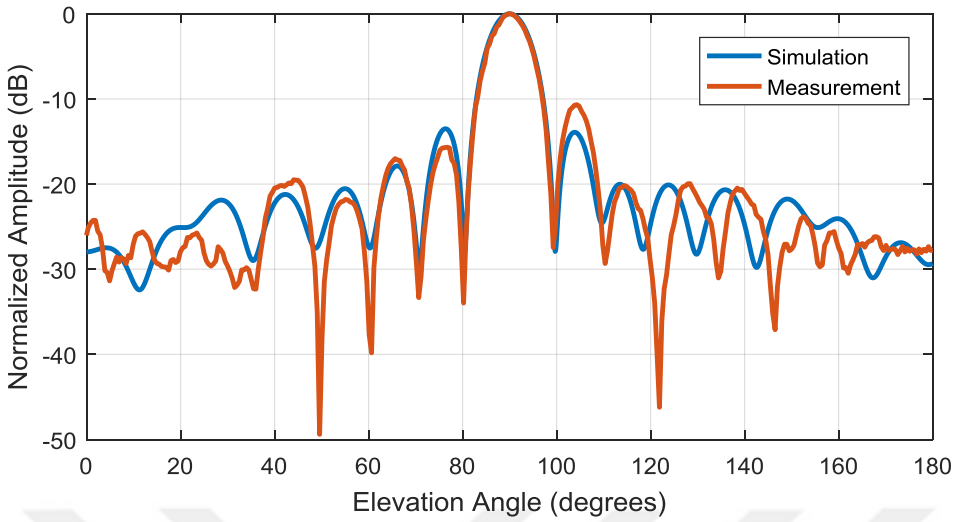

Figure 4.38. Comparison of the simulation (dashed line) and the measurement (solid line) results for the far-field pattern at 1.06 f_c.

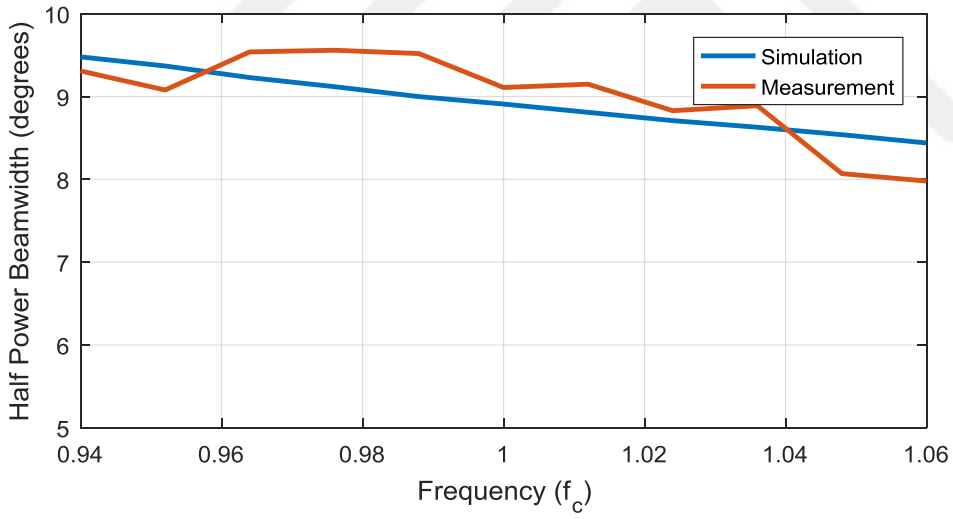

Figure 4.39. Comparison of the simulation and measurement results for the half-power beamwidth.

4.2.2. 8x1 Vivaldi Array Combined with the 8-way Power Divider and Hybrid Coupler Probe

For measurements of one line of the final design, i.e., 8x1 Vivaldi array combined with the 8-way power divider and the unit cell with the hybrid coupler probe, both ridged-waveguide ends of the unit cell are connected to the ridged-waveguide-to-standard-waveguide transitions (similar to the unit cells with the single probe and the hybrid coupler probe). This structure is modeled as shown in Figure 4.40. Fabricated PCB cards shown in Figure 4.41 are combined using screws and support material and they are mounted on the ridged-waveguide section (shown in Figure 4.23) to realize the structure. This final structure is shown in Figure 4.42. Measurement setup is shown in Figure 4.34, while the antenna structure under test is shown in Figure 4.43. E-plane far-field patterns at three different frequencies obtained via simulation and measurement are compared in Figure 4.44 to Figure 4.46. It can be stated that patterns of the fabricated antennas show higher side-lobe levels than simulation results, as well as significant asymmetries. In Figure 4.47, simulated and measured half-power beamwidths are further compared. Over the frequency band, the difference between half-power beamwidths of the simulated and fabricated array is below 1.52°. The differences between the simulation and measurement results may be due to uncertainties mentioned in Section 4.2.2. Moreover, at the coupler arms inside the waveguide, PCBs may not be fully attached, which may affect the results as mentioned in Section 4.1.3.

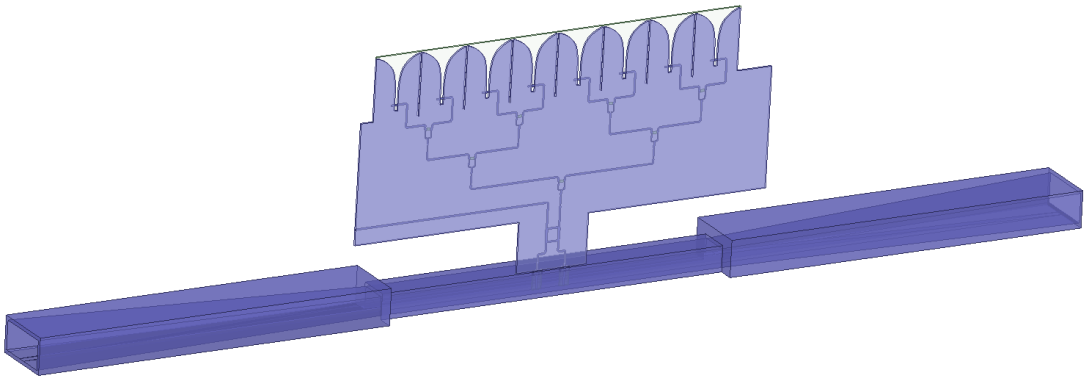

Figure 4.40. Modeled 8x1 Vivaldi array combined with the 8-way power divider and the hybrid coupler probe.

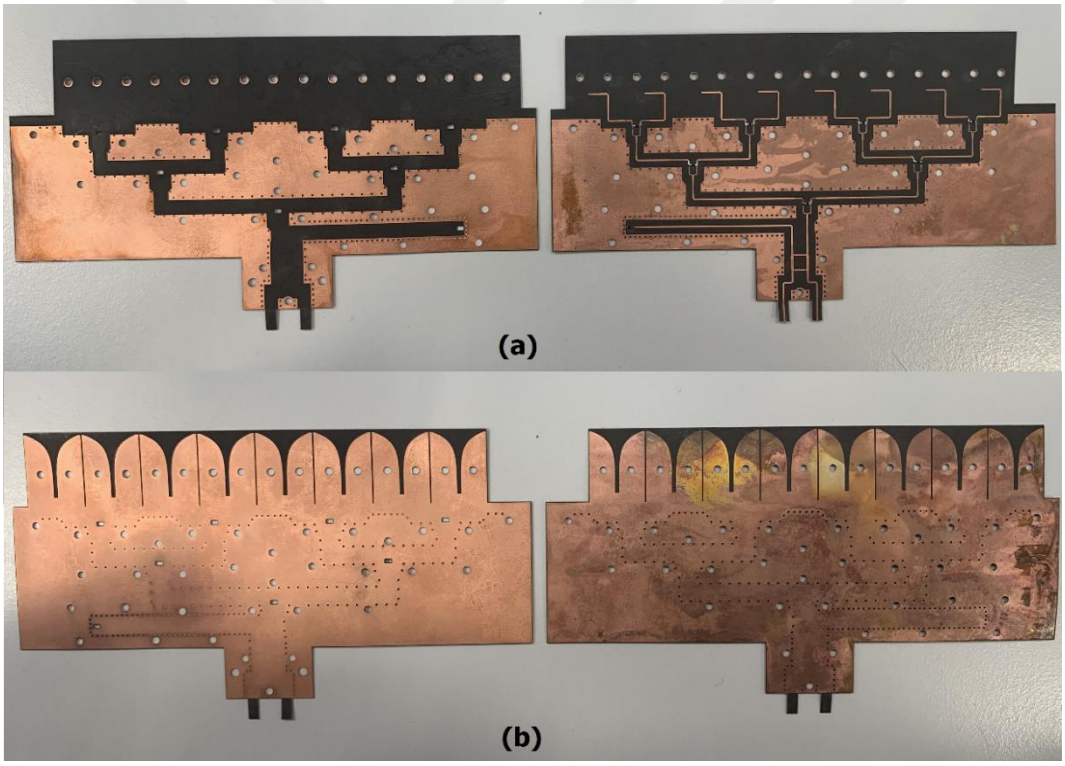

Figure 4.41. PCBs 8x1 Vivaldi array combined with the 8-way power divider and the hybrid coupler probe. (a) Front and (b) back.

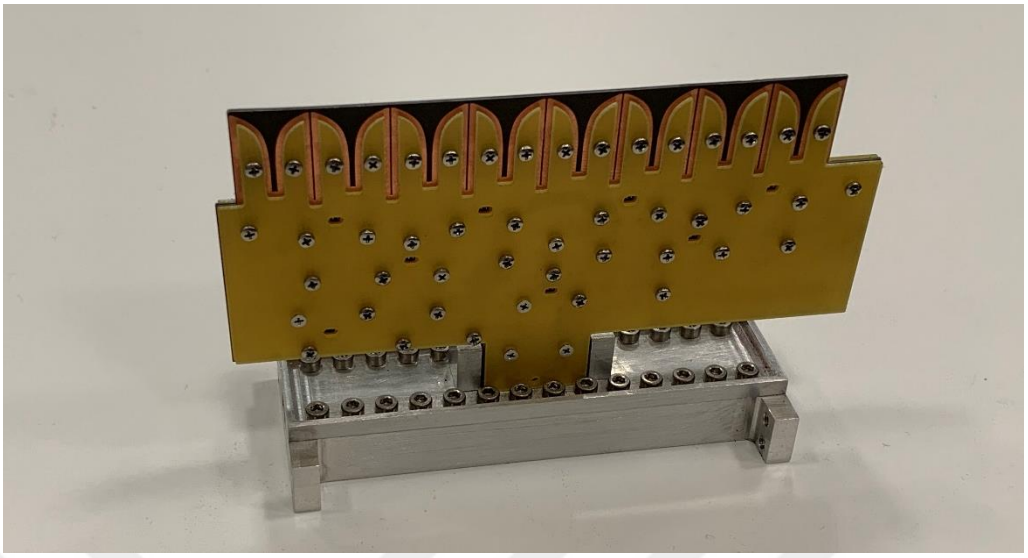

Figure 4.42. Fabricated 8x1 Vivaldi array combined with the 8-way power divider and the hybrid coupler probe.

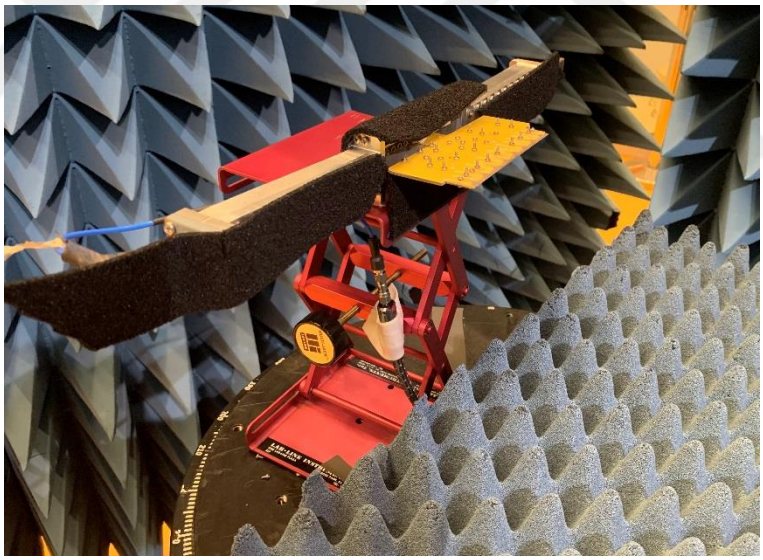

Figure 4.43. 8x1 Vivaldi array combined with the 8-way power divider and the hybrid coupler probe under test.

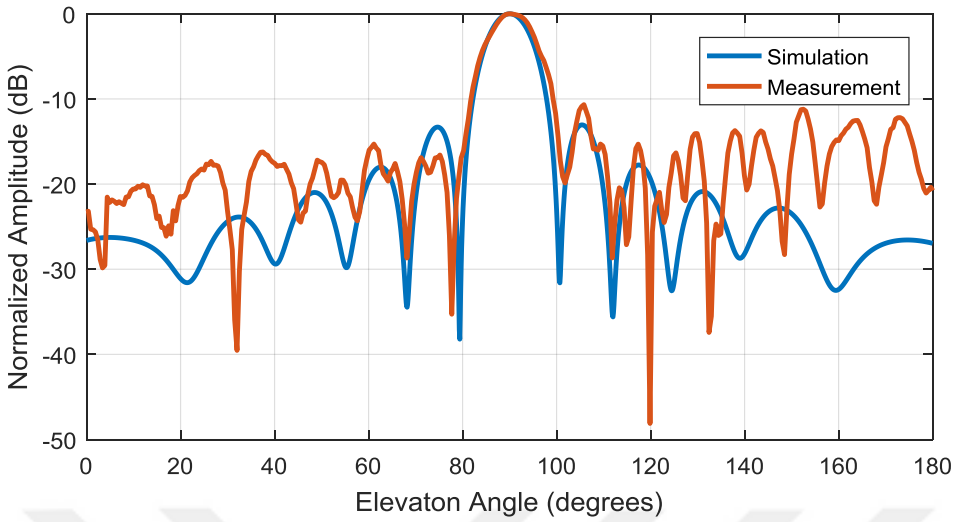

Figure 4.44. Comparison of the simulation (dashed line) and measurement (solid line) results for the far-field pattern at 0.94 f_c.

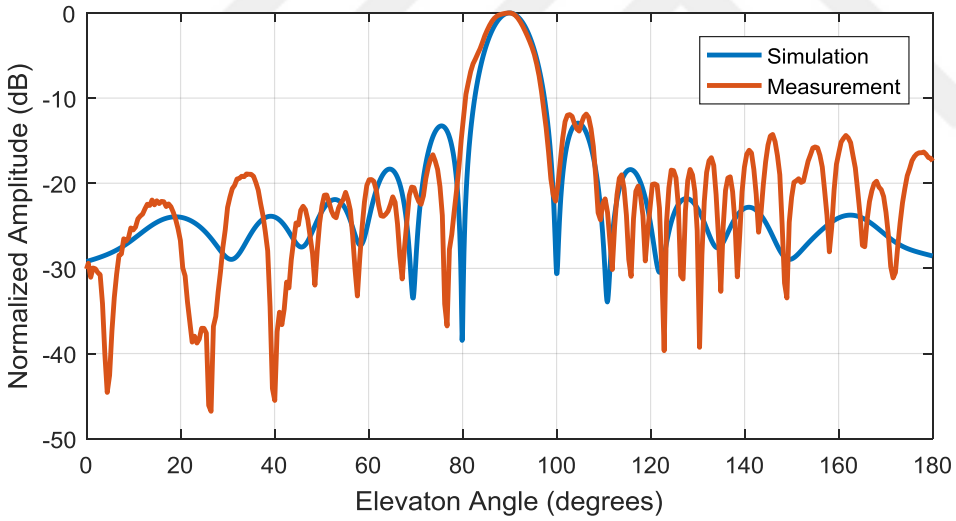

Figure 4.45. Comparison of the simulation (dashed line) and measurement (solid line) results for the far-field pattern at f_c.

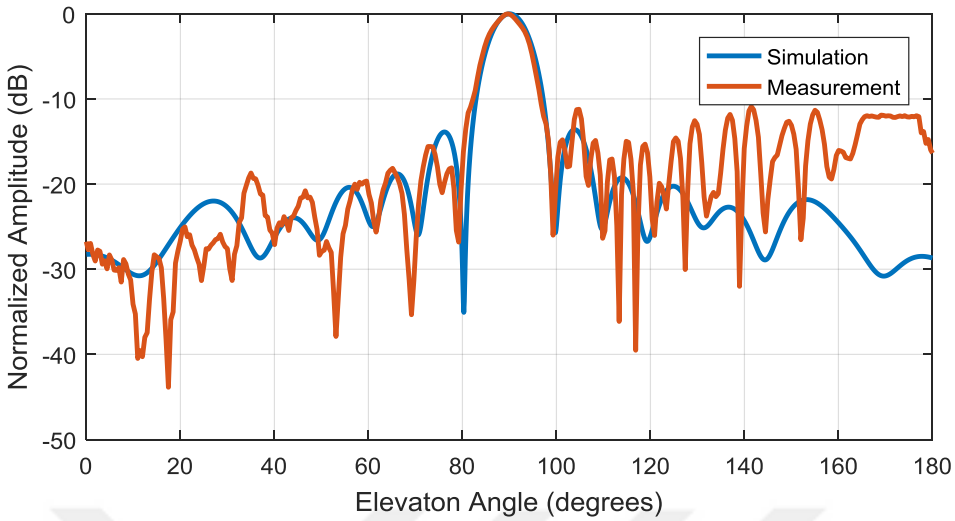

Figure 4.46. Comparison of the simulation (dashed line) and measurement (solid line) results for the far-field pattern at 1.06 f_c.

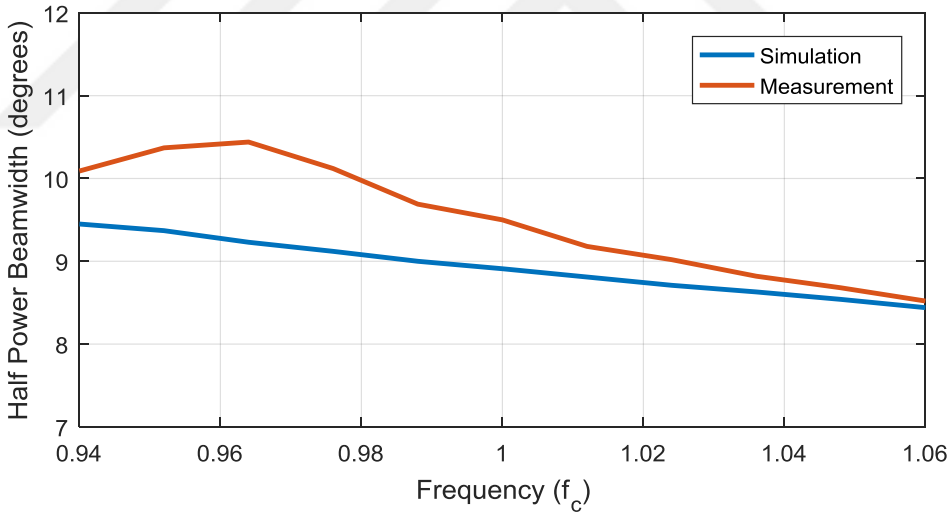

Figure 4.47. Comparison of the simulation and measurement results for the half-power beamwidth.

4.3. Error Analysis

In Figure 4.27, measured and simulated coupling values for the fabricated unit cell with hybrid coupler probe are compared for different inset lengths. In this section, the errors on the measured coupling values are discussed.

In Figure 4.27, it can be stated that, for inset length values larger than $0.0605\lambda_c$, the maximum error, i.e., the maximum value of the absolute difference between the simulation and measurement results, over the frequency band of operation is 2.5 dB. Since, the minimum inset length that is used in the final design of the antenna is $0.0653\lambda_c$, the maximum error that may be observed in the coupling values of the unit cells of the final design can be specified as 2.5 dB.

Normalized array factors are synthesized at five different frequencies, leading to the addition of a random error that changes from -2.5 dB to 2.5 dB to the coupling values of the each unit cell of the final design. To investigate this, a Monte Carlo analysis is performed with 1000 different random error set. Normalized array factors are synthesized with 1000 different random error sets and the maximum values for each azimuth angle are obtained, corresponding to the worst case. The normalized array factors that are synthesized with the maximum values for each azimuth angle are given in Figure 4.48 together with the expected normalized array factor (which is also given in Figure 3.39). It is observed that scanning performance of the array does not deteriorate but side lobe levels increase up to -17 dB.

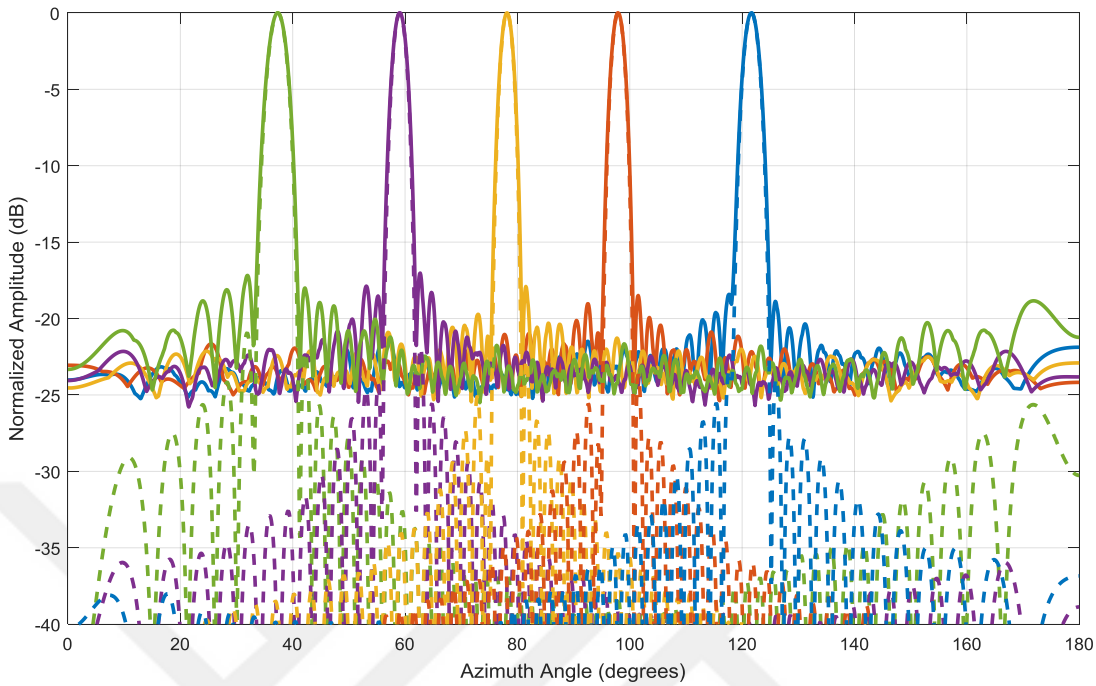

Figure 4.48. Comparison of the expected normalized array factor (solid line) and the worst normalized array factor obtained with Monte Carlo analysis (dashed line).

CHAPTER 5

CONCLUSION

In this study, a novel low-loss frequency scanning antenna structure is designed according to a set of design specifications. The designed structure is an array of Vivaldi antenna and it is composed of 56 8-element arrays aligned along an axis. This axis (azimuth) is the one for frequency scanning, while the pattern in the elevation axis is shaped by 8-element arrays. The antennas are fed by utilizing a waveguide beamformer with stripline 90-degree hybrid couplers whose input arms are inserted into the waveguide.

The beamformer design is started with the selection of element spacing and number of elements. The inter-element spacing to satisfy the frequency scan requirements results in an infeasible waveguide width, if an ordinary waveguide is considered. In order to lower the cutoff frequency of the fundamental mode, a single-ridge waveguide is utilized. To realize the progressive phase shift between consecutive elements, a serpentine waveguide design is proposed. Since the hybrid couplers are inserted through the slots on the broadwall of the waveguide, H-plane meandering is realized by optimizing H-plane turns. The length of the waveguide section between the elements is carefully determined such that the progressive phase shift between consecutive elements ensures the required scan range.

The unit cell of the beamformer array is constructed such that it involves an elementary unit of the waveguide with stripline coupler structure that couples energy from the waveguide to feed the antenna elements. Different architectures of stripline couplers are discussed and a novel 90-degree hybrid coupler structure is decided to proceed with. It is preferable since it has small reflections at the frequency of the broadside radiation, it is well-matched at coupling port, and it offers a low-loss design.

The reflections at the frequency of the broadside radiation are critical, because at this frequency, reflections from the unit cells are summed up in phase at the input port. If these reflections are not reduced in phase summation of reflections may result in scan blindness.

After deciding on the coupling structure, the unit cells need to be selected to form the array. The amplitude of coupling is controlled by the insertion depth of the 90-degree hybrid coupler. First, the unit cell is characterized for different values of the inset length. It is observed that the coupling amplitude has a flat characteristic over the frequency band, and the return loss at the waveguide port is less than -38 dB. The network parameters from characterization data are interpolated to obtain a smoother data set for more values of the inset length. The required insertion values are selected such that the array satisfies Taylor line source distribution with approximation that the loss for each cell is the same and average of the characterization data. The selections are made at the center frequency.

The selected unit cells are treated as three-port blocks and rigorously cascaded to observe the coupling through the stripline ports, i.e., the excitation for arrays in the elevation axis. It is observed that there is a disturbance on the excitation magnitudes and, starting with these initial guesses, an optimization is carried out to determine the inset lengths more precisely.

Since the inset lengths of the unit cells on the array are different, the phases of the signals at the coupling ports differ from the desired excitation phases. This error is decreased, if not eliminated, by appropriately extending the striplines at the coupling port.

The bandwidth of a TSA is mainly determined by the bandwidth of the feeding section. Thus, the design of the radiating element is started with the design of a stripline-to-slotline transition. After that, a Vivaldi element is designed by applying proper boundary conditions on both E- and H-planes. Since the phase difference on the H-plane walls of an element depends on the frequency, the phase difference is

formulated with respect to frequency and defined while assigning boundaries for the H-plane. Eight of the Vivaldi elements are used to form the array in the elevation axis. While the excitations are realized by the beamformer network in the azimuth axis, an 8-way power divider that consists of 2-way Wilkinson power dividers is designed to divide the power in the elevation axis.

Repeating eight element Vivaldi arrays with power divider networks along a line for 56 times and connecting the beamformer network, the final design is constructed. The final design is simulated and the following results are obtained. The antenna works in 12% bandwidth between $f_{low} = 0.940f_c$ and $f_{high} = 1.060f_c$. In this frequency band, the beam is scanned from 36.8° to 121° with a total angular range of 84.2° in the azimuth axis. In the azimuth axis, the side-lobe levels are below −20.5 dB for the entire frequency band and the half-power beamwidth is 2.2° at the broadside. At the frequency for broadside radiation, the total loss is −6 dB due to high return loss at the input port. For other frequencies, the total loss is below approximately −5.5 dB with maximum loss at f_{high}. A big portion of the loss is due to the 8-way power divider. For applications that do not require a narrow beam in the elevation axis the loss of the 8-way power divider would be eliminated. In that case, the loss would be as low as −3 dB.

All design specifications (see Table 1.1) have been satisfied in the simulation results. Comparisons of design criteria and simulation results are given in Table 5.1.

Although some prototypes related to the design procedure are fabricated and measured in the context of the thesis, fabrication of the complete design is left as a future work. Fabricated prototypes can be listed as follows.

- Unit cell with the single probe
- Hybrid coupler
- Unit cell with the hybrid coupler probe
- 8-way power divider
- 8x1 Vivaldi array combined with the 8-way power divider

- 8x1 Vivaldi array combined with the 8-way power divider and unit cell with the hybrid coupler probe

For the unit cells with probes, coupling measurements are performed. The errors in the couplings due to fabrication and measurement processes are examined with a sensitivity analysis procedure. It is observed that scanning performance is robust against this type of errors; however, side lobe levels increase up to -17 dB. For the prototypes that include Vivaldi arrays, pattern measurements are performed. It is observed that the measured patterns show some deviations from the simulated patterns and they show asymmetry.

The errors on alignment and compression of the PCBs while combining with screws and support material may have serious effects on the results. This is particularly important in the prototypes that are unit cells since the arms inside the waveguide may not be fully attached. During the fabrication of the complete design, PCBs are going to be combined by a proper bonding film and bonding process, which may eliminate such errors.

One of the contributions of this thesis is the utilization of the 90-degree coupler to create a low-reflection waveguide-to-stripline coupling network. In the context of this study, the two arms of a coupler inside the waveguide are of the same length. This was preferred to avoid increasing the characterization time and complicating the design procedure. However, it is not mandatory. As a future extension of this study, different arm lengths can still be employed to generate more degrees of freedom in the design and this freedom can be exploited to feed the antenna from both ends. This could be examined with the current design; but, when the designed antenna is driven from the terminated port, the magnitude of the excitation coefficients would be far from optimum and the antenna performance would be unacceptable. Nevertheless, if the proposed future work is carried out, it might be possible to optimize the radiation patterns when both (one at a time) ports used for exciting the structure. If this turns out to be feasible, the bandwidth requirement of the antenna and therefore the radar

system may be halved. This could be possible as the antenna would scan from left to broadside for one port, and from right to broadside for the other, within the half of the bandwidth of the current design. While doing this, the terminated port of the 90-degree coupler can be connected to a secondary array or the same array can be switched between two ports of the coupler by means of a solid-state switch.

Table 5.1. Design specifications

Specification	**Specified Value**	**Model Value**
Frequency bandwidth (for the specified scan range and side-lobe level at azimuth axis)	12 %	12 %
Scan range	>80°	84.2°
Half-power beamwidth at broadside (azimuth axis)	<2.3°	2.2°
Half-power beamwidth at broadside (elevation axis)	~9°	9.2°
Side-lobe level (azimuth axis)	<−18 dB	<−20.5 dB

REFERENCES

[1] Barton, D. K., and Leonov, S. A., *Radar Technology Encyclopedia*. Artech House, 1998.

[2] Balanis, C. A., *Antenna Theory: Analysis and Design*, 3rd ed. John Wiley & Sons, 2016.

[3] Skolnik, M. I., *Introduction to Radar Systems*, 3rd ed. McGraw Hill Book, 1980.

[4] Allen, J. L., and Diamond, B. L., IEEE Standard Definitions of Terms for Antennas, 1966.

[5] Allen, J. L., and Diamond, B. L., "Mutual coupling in array antennas," (No. TR-424). Massachusetts Inst. of Tech. Lexington Lincoln Lab, Lexington, MA, USA, Tech. Rep. TR-424, 1966.

[6] Edelberg, S., and Oliner, A., "Mutual coupling effects in large antenna arrays: Part 1-Slot Arrays," *IRE Transactions on Antennas and Propagation*, vol. 8, pp. 286–297, 1960.

[7] Hansen, R. C., *Phased Array Antennas*, 2nd ed. John Wiley & Sons, 2009.

[8] Volakis, J. L., *Antenna Engineering Handbook*, 4th ed. New York: McGraw-Hill, 2007.

[9] Elliot, R. S., *Antenna Theory and Design*, revised ed. John Wiley & Sons, 2006.

[10] Ma, X., and Xu, R., "A broadband W-band E-plane waveguide-to-microstrip probe transition," in *Asia-Pacific Microwave Conference*, 2008.

[11] Gültepe, G., "Monopulse wideband waveguide based travelling wave array antenna," M.S. thesis, Middle East Technical University, 2017.

[12] Uchendu, I., and Kelly, J. R., "Survey of beam steering techniques available for millimeter wave applications," *Progress in Electromagnetics Research*, vol. 68, pp. 35–54, 2016.

[13] Baek, C. W., Song, S., Cheon, C., Kim, Y. K., and Kwon, Y., "2-D mechanical beam steering antenna fabricated using MEMS technology," in *IEEE MTT-S International Microwave Symposium Digest*, 2001.

[14] Von Aulock, W. H., "Properties of phased arrays," *Proceedings of the IRE*, vol. 48, pp. 1715–1727, 1960.

[15] Kahrilas, P. J., "Design of electronic scanning radar systems (ESRS)," *Proceedings of the IEEE*, vol. 56, pp. 1763–1771, 1968.

[16] Wanh, H., Ge, P., Fang, D. G., Ma, X. F., and Sheng, W. X., "A low loss frequency scanning planar array using hybrid coupling" in *International Conference on Microwave and Millimeter Wave Technology*, pp. 1908–1911, 2010.

[17] Hilburn, J. L., Kikney, R. A., Emmett, R. W., and Prestwood, F.H., "Frequency-scanned X-band waveguide array," *IEEE Transactions on Antennas and Propagation*, vol. 20, pp. 506–509, 1972.

[18] Hilburn, J. L., Kikney, and Prestwood, F.H., "K band frequency-scanned waveguide array," *IEEE Transactions on Antennas and Propagation*, vol. 22, pp. 340–342, 1974.

[19] Hamidi, E., "Design, analysis and simulation of a C band frequency scanning slot-array antenna," in *International Conference on Computer and Communication Engineering*, 2010.

[20] Royle, M., "Frequency-scanned waveguide-fed slot array for millimetre-wave radar applications," M.S. thesis, University of Toronto, Toronto, Canada, 2016.

[21] Wang, Q., Wang, H., Cao, J., Zhang, Y., Quan, S., and Liu, X., "Design and process improvement of a Ku-band wide angle low side-lobe frequency scanning antenna," in *IEEE MTT-S International Wireless Symposium (IWS)*, 2019.

[22] Sakakibara, K., Hirokawa, J., Ando, M., and Goto, N., "A slotted waveguide array using reflection-canceling slot pairs," in *Proceedings of the International Symposium on Antennas and Propagation*, 1992.

[23] Sato, J., Hirokawa, J., and Ando, M., "Reflection-canceling of slotted waveguide antenna by using a circular pit," in *IEEE Antennas and Propagation Society International Symposium*, vol. 3, pp. 1706–1709, 1998.

[24] Park, S., Hirokawa, J., and Ando, M., "Analysis and design of a waveguide slot and a reflection-canceling inductive wall," in *IEEE Topical Conference on Wireless Communication Technology*, pp. 362–363, 2003.

[25] Eberle, J., Levis, C., and McCoy, D., "The flared slot: A moderately directive flush-mounted broad-band antenna," *IRE Transactions on Antennas and Propagation*, vol. 8, pp. 461–468, 1960.

[26] Gibson, P. J., "The vivaldi aerial," in *9th European Microwave Conference*, pp. 101–105, 1979.

[27] Prasad, S. N., and Mahapatra, S., "A novel MIC slot-line antenna," in *9th European Microwave Conference*, pp. 120–124, 1979.

[28] Janaswamy, R., and Schaubert, D., "Analysis of the tapered slot antenna," *IEEE Transactions on Antennas and Propagation*, vol. 35, pp. 1058–1065, 1987.

[29] Gazit, E., "Improved design of the Vivaldi antenna," *IEE Proceedings H-Microwaves, Antennas and Propagation*, vol. 135, pp. 89–92, 1988.

[30] Schaubert, D., Kollberg, E., Korzeniowski, T., Thungren, T., Johansson, J. O. A. K. I. M., and Yngvesson, K., "Endfire tapered slot antennas on dielectric substrates," *IEEE Transactions on Antennas and Propagation*, vol. 33, pp. 1392–1400, 1985.

[31] Collin, R. E., and Zucker, F. J., *Antenna Theory*. New York: McGraw-Hill, 1969.

[32] Lee, R. Q., "Notch antennas," in *Encyclopedia of RF and Microwave Engineering* (Chang, K., ed.), 2005.

[33] Yngvesson, K. S., Korzeniowski, T. L., Kim, Y. S., Kollberg, E. L., and Johansson, J. F., "The tapered slot antenna-a new integrated element for millimeter-wave applications," *IEEE Transactions on Microwave Theory and Techniques*, vol. 37, pp. 365–374, 1989.

[34] Kasturi, S., and Schaubert, D. H., "Effect of dielectric permittivity on infinite arrays of single-polarized Vivaldi antennas," *IEEE Transactions on Antennas and Propagation*, vol. 54, pp. 351–358, 2006.

[35] Knorr, J. B., "Slot-line transitions (short papers)," *IEEE Transactions on Microwave Theory and Techniques*, vol. 22, pp. 548–554, 1974.

[36] Seman, N., and Bialkowski, M., "Microstrip-slot transition and its applications in multilayer microwave circuits," in *Passive Microwave Components and Antennas*, ch. 12, pp. 247–266, IntechOpen, 2010.

[37] Shuppert, B., "Microstrip/slotline transitions: modeling and experimental investigation," *IEEE Transactions on Microwave Theory and Techniques*, vol. 36, pp. 1272–1282, 1988.

[38] Shin, J., and Schaubert, D. H., "A parameter study of stripline-fed Vivaldi notch-antenna arrays," *IEEE Transactions on Antennas and Propagation*, vol. 47, pp. 879–886, 1999.

[39] Langley, J. D. S., Hall, P. S., and Newham, P., "Balanced antipodal Vivaldi antenna for wide bandwidth phased arrays," *IEE Proceedings-Microwaves, Antennas and Propagation*, vol. 143, pp. 97–102, 1996.

[40] T. T. Taylor, "Design of line-source antennas for narrow beamwidth and low sidelobes," *IRE Transactions on Antennas and Propagation*, vol. 3, pp. 16–28, 1955.

[41] Pozar, D. M., *Microwave Engineering*, 4th ed. John Wiley & Sons, 2011.